

AD-A059 530

ILLINOIS INST OF TECH CHICAGO DEPT OF MECHANICS MECH--ETC F/G 20/4
AN EXPERIMENTAL INVESTIGATION OF THE NEAR WAKE OF A CIRCULAR CY--ETC(U)
MAY 76 R W WLEZIEN, J L WAY F44620-76-C-0062

UNCLASSIFIED

IIT-FLUIDS/HEAT TRANS-R76 AFOSR-TR-78-1292

NL

1 OF 2
AD
A059530



LEVEL II

2

AFOSR-TR- 78-1292

Illinois Institute of Technology, Chicago, Illinois 60616

AN EXPERIMENTAL INVESTIGATION OF THE NEAR WAKE OF A
CIRCULAR CYLINDER IN THE SUBCRITICAL REGIME

BY

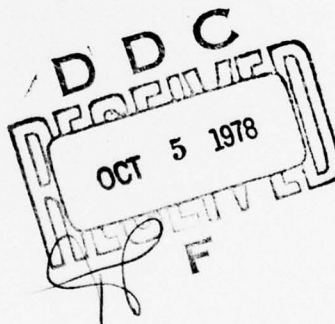
Richard W. Wlezien and John L. Way

IIT Fluids & Heat Transfer Report R76-3

May, 1976

AD A059530

DDC FILE COPY



Supported under USAF OSR Grant AFOSR-73-2509 and
Contract F 44620-76-C-0062

APPROVED FOR PUBLIC RELEASE; DISTRIBUTION UNLIMITED

Qualified requestors may obtain additional copies from
the Defense Documentation Center, all others should
apply to the National Technical Information Service.

78 09 05 026

Conditions of Reproduction

Reproduction, translation, publication, use and disposal in whole or in part by or for the United States Government is permitted.

AIR FORCE OFFICE OF SCIENTIFIC RESEARCH (AFSC)
NOTICE OF TRANSMITTAL TO DDC
This technical report has been reviewed and is approved for public release IAW AFR 190-12 (7b).
Distribution is unlimited.
A. D. BLOSE
Technical Information Officer

SECURITY CLASSIFICATION OF THIS PAGE (When Data Entered)

DD FORM 1 JAN 73 1473 EDITION OF 1 NOV 68 IS OBSOLETE

SECURITY CLASSIFICATION OF THIS PAGE (When Data Entered)

400 437

UNCLASSIFIED

SECURITY CLASSIFICATION OF THIS PAGE(When Data Entered)

cont. → transform technique. This method is a generalization of the monochromatic complex rotating vector to processes which are modulated. The computed phase is used to conditionally sample the wake temperature using a six-sensor resistance thermometer array, and the resulting data are processed using statistical methods. Results demonstrate that the near wake region contains diffuse vortical fluid and this fluid has a role in the shear layer instability. The statistics also show the formation and shedding of a mean Karman vortex, and lead to a possible explanation of the modulation process.

UNCLASSIFIED

SECURITY CLASSIFICATION OF THIS PAGE(When Data Entered)

ACKNOWLEDGMENT

The authors would like to express their sincere appreciation to Professors Mark V. Morkovin and Hassan M. Nagib for their advice and assistance in all phases of this work. We are grateful to Price Hodson for his valuable help in setting up the experiment. Special thanks go to Randy Goettsche for his assistance with the figures and to Kathy Wolowiec and Carol Timkovich for their diligent typing efforts. This research has been supported under USAF OSR Grant AFOSR-73-2509 and Contract F 44620-76-C-0062.

R.W.W. and J.L.W.

ACCESSION for	
NTIS	White Section <input checked="" type="checkbox"/>
DDC	Buff Section <input type="checkbox"/>
UNANNOUNCED	<input type="checkbox"/>
JUSTIFICATION	<input type="checkbox"/>
BY	
DISTRIBUTION/AVAILABILITY NOTES	
Date	
A	

TABLE OF CONTENTS

	Page
ACKNOWLEDGEMENT	iii
LIST OF TABLES	vi
LIST OF FIGURES	vii
NOTATION	x
ABSTRACT	xii
CHAPTER	
I. INTRODUCTION	1
Relevant Literature	1
Objectives	8
Description of Experiment	10
II. ANALYSIS OF SIGNAL PROCESSING	12
Spectrum and Coherence Estimation	12
Processing of Narrow-Band Signals	16
Conditional Probability	23
III. EXPERIMENTAL FACILITIES AND INSTRUMENTATION	26
Flow Visualization Wind Tunnel	26
Water Table	27
Environmental Wind Tunnel	28
Cylinder Model	31
Phasing Signal	36
Temperature Measurement	37
Data Acquisition and Processing System (DAPS)	41
IV. DATA PROCESSING TECHNIQUES	42
Acquisition of Time Series	42
Spectral Estimation	44
Filter and Hilbert Transformer Implementation	45
Conditional Analysis of Wake Temperature	49
Error Analysis	51
V. RESULTS AND DISCUSSION	54
Wind Tunnel Diagnostics	54
Wake Measurements	57

CHAPTER		Page
VI. CONCLUSIONS AND RECOMMENDATIONS		70
Conclusions		70
Recommendations		75
APPENDIX		
TABLES AND FIGURES		78
BIBLIOGRAPHY		124

LIST OF TABLES

Table		Page
1.	Wind Tunnel Diagnostic Measurements	78
2.	Data Acquisition Runs	79

LIST OF FIGURES

Figure		Page
1.	The Inverse of the Strouhal Number as a Function of Reynolds Number for Circular Cylinders	80
2.	Transition Length, L_t , as a Function of Reynolds Number	81
3.	Linear and Log Power Spectrum of Boxcar Window	82
4.	Linear and Log Power Spectrum of Hamming Window	83
5.	Log Power Spectral Density of Phasing Velocity, U_ϕ	84
6.	Schematic of Complex Analytic Representation of a Real Function	85
7.	Photograph and Schematic of Flow Visualization Wind Tunnel	86
8.	Photograph and Schematic of Water Table Facility	87
9.	Photograph and Schematic of High Speed Test Section of Environmental Wind Tunnel	88
10.	Instrumentation for Wind Tunnel Diagnostic Measurements	89
11.	Photographs of Cylinder Model, Heating Strip and End Plate	90
12.	Cylinder Finite Difference Heat Transfer Model.	91
13.	Results of Solution of Difference Equations for Cylinder Heat Transfer Model	92
14.	Temperature Drifts in Environmental Wind Tunnel and Cylinder Coolant.	93
15.	Flow Visualization Diagnostics of Sidewall Boundary Layer Interaction with Flowfield at Front of Cylinder	94
16.	Phasing Velocity Sensor and Electronics	95

Figure		Page
17.	Calibration of Phasing Velocity Measurement Circuit	96
18.	Circuit Diagram of Six Channel Differential Resistance Thermometer	97
19.	Calibration of Six Channel Differential Resistance Thermometer	98
20.	Dye Flow Visualization of Interaction of Six-Sensor Probe with Cylinder Wake	99
21.	Different Views and Close-Up of Six-Sensor Temperature Probe	100
22.	Photographs of Cylinder Model with Probes and Instrumentation.	101
23.	Analog Instrumentation and Data Processing System	102
24.	Wake Sensor Locations with Respect to Cylinder Model	103
25.	Log Power Spectral Density of Oversampled Phasing Velocity, U_ϕ	104
26.	Linear and Log Magnitude Frequency Response of 63 Point Bandpass Filter	105
27.	Linear and Log Magnitude Frequency Response of 31 Point Hilbert Transformer	106
28.	Illustration of Starting Losses for Digital Filter and Hilbert Transformer	107
29.	Bandlimited Function $z(t)$, Quadrature Function $z^1(t)$, and Phase Angle $\phi(t)$ Computed From U_ϕ	108
30.	Example of Six-Sensor Temperature Information Conditionally Sampled Based on Phase	109
31.	Linear Compensation for Drift in Channel Five Temperature Circuit	110
32.	Comparison of Room Pressure and Free Stream Velocity for $U_\infty = 4$ ft/sec	111
33.	Comparison of Room Pressure and Free Stream Velocity for $U_\infty = 21.5$ ft/sec	112

Figure		Page
34.	Comparison of Phasing Velocity and Free Stream Velocity for $U_{\infty} = 4$ ft/sec113
35.	Comparison of Phasing Velocity and Free Stream Velocity for $U_{\infty} = 21.5$ ft/sec114
36.	Mean Temperature and Velocity Profiles of Cylinder Boundary Layer Near Separation Line115
37.	Phase Shift in Cross Correlation of U and θ as a Function of Temperature $^{\phi}$ Sensor Downstream Position116
38.	Instantaneous Amplitude and Frequency as Computed from Sample U_{ϕ} Data117
39.	Dependence of Probability Distributions on Temperature Threshold Level for $\phi = 0$.	.118
40.	Dependence of Probability Distributions on Temperature Threshold Level for $\phi = 0$ at $x/D = 0.5$119
41.	Probability Distributions Through First Half of Shedding Cycle for High Temperature Threshold120
42.	Probability Distributions Through Second Half of Shedding Cycle for High Temperature Threshold121
43.	Regions of Non-Zero Probability Through Shedding Cycle for High Temperature Threshold122
44.	Phase Dependence of Probability Distributions at $x/D = .75$ for High Temperature Threshold123

NOTATION

Symbol	Term
A	Instantaneous amplitude modulation
A_{yzt}	Discrete coherence function
B_e	Effective bandwidth
C_{yzt}	Discrete cross-correlation function
D	Cylinder diameter
f	Circular frequency
f_r	Discrete frequency
f_s	Sampling rate
f_{St}	Strouhal frequency
f_o	Folding frequency
G_{zzt}	Discrete power spectral density function
h_n	Discrete filter impulse response
H_r	Discrete filter frequency response
L_d	Diffusion length scale
L_f	Formation length scale
L_t	Transition length scale
N	Number of samples
p	Probability density function
P	Probability distribution function
P_r	Room pressure
Re	Reynolds number

Symbol	Term
St	Strouhal number
t	Time
T	Period
u	Time domain window
U	Frequency domain window
U_{ϕ}	Phasing velocity
U_{∞}	Freestream velocity
x	Longitudinal coordinate
y	Vertical coordinate
y_n	Input time series
Y_r	Discrete Fourier transform of y_n
z	Input time function
z^a	Analytic signal
z^i	Imaginary part of z^a
z_n	Input time series
Z	Fourier transform of z
Z_r	Discrete Fourier transform of z_n
α	Frequency dependent amplitude
ϵ	Normalized standard error
θ	Temperature difference
ϕ	Phase angle
ϕ_c	Phase shift in correlation
ψ	Frequency dependent phase angle
ω	Angular frequency

ABSTRACT

The near wake of a circular cylinder in crossflow is experimentally investigated for Reynolds number 7600. The purpose is to develop techniques for characterizing the formation region of the Kármán vortex street in the presence of transition to turbulence and to use these techniques to examine the quasi-periodic vortex shedding phenomenon. A thermal tracer is used to tag vortical fluid in one of the cylinder boundary layers and this scalar is subsequently detected in the wake. The instantaneous phase of the amplitude and frequency modulated polychromatic vortex shedding phenomenon is computed using a digital Hilbert transform technique. This method is a generalization of the monochromatic complex rotating vector to processes which are modulated. The computed phase is used to conditionally sample the wake temperature using a six-sensor resistance thermometer array, and the resulting data are processed using statistical methods. Results demonstrate that the near wake region contains diffuse vortical fluid and this fluid has a role in the shear layer instability. The statistics also show the formation and shedding of a mean Kármán vortex, and lead to a possible explanation of the modulation process.

CHAPTER I

INTRODUCTION

Previous work related to the formation region in the wake of a circular cylinder in crossflow is discussed. Open questions related to length scales and the transition to turbulence are considered. This leads to an examination of relevant experimental techniques found in recent literature. The determination of a more objective experimental technique for the characterization of the near wake is established as the objective of the present research, and the resulting experiment is presented.

Relevant Literature

The underlying mechanism of the Kármán vortex street has proven to be a particularly elusive phenomenon in fluid mechanics. In 1911 Kármán[29] presented his theory of the vortex street. Quoting Roshko [23] in 1955: "It can hardly be said that any fundamental advance in the problem has been made since Kármán's stability papers...". The near wake of a bluff body has shown itself to be a region of complex interaction among flow parameters, including Reynolds number, geometry and free stream turbulence level. A unified relationship between these and other flowfield parameters remains to be found.

Based on experiments and qualitative observations, the vortex shedding phenomenon has been classified into several

distinct regimes summarized by Morkovin [20]. The regime to be considered in the following work is termed "subcritical" and encompasses flow around cylinders for a Reynolds number range of 150-300 to $10^5 - 1.3 \times 10^5$. This range of Re is characterized by single vortex sheet instability in the separated boundary layer, with the transition to turbulence approaching the cylinder with increasing Re . An interesting characteristic is the relative constancy of the Strouhal number within this range, as shown in Figure 1.

In an effort to further understand this Reynolds number regime, Bloor [3] investigated the transition to turbulence in the near wake. For a Re range of 1.3×10^3 to 8×10^3 she found regular transition waves in the separated shear layer. The downstream position at which these waves first appear was measured for a variety of Re . This transition length, L_t , decreases with increasing Re (Fig. 2). It was her conclusion that transition to turbulence occurs as a result of nonlinear distortion of these Bloor vortices, as they are now known.

For Re greater than approximately 8×10^3 , these transition waves are not evident within the shear layer, and the shear layer becomes turbulent almost immediately after separation. In a later work, Shimizu [26] suggests that the L_t versus Re curve might change more abruptly near $Re = 8000$ (see Fig. 2). A more immediate laminar-turbulent

transition seems to replace the regular transition waves in the shear layer. He further subdivides the regimes of Morkovin [20] into second subcritical ($300 < Re < 5 \times 10^3$), second critical ($5 \times 10^3 < Re < 10^4$), and first subcritical ($10^4 < Re < 3.5 \times 10^5$), based on the decrease in spanwise organization of the vortex shedding. However questions pertaining to the transition to turbulence and the onset of three dimensionality still remain.

Another length scale measured by Bloor [3] is the formation length, L_f . It is an indication of the downstream distance at which the actual roll-up of the Kármán vortices occurs. She noted that the low frequency velocity irregularities always observed immediately behind the cylinder are suddenly reduced at the point where the vortices form. This was the method used by Bloor to measure L_f .

In more recent work, researchers have attempted to measure this quantity by various methods, but its exact definition has been rather ambiguous throughout the literature. Gerrard [13] defines L_f as the downstream distance at which non vortical fluid first crosses the center of the wake. In another work, Bloor and Gerrard [4] define the formation length as the downstream position where there is the greatest velocity fluctuation at the second harmonic of the eddy shedding frequency. Schaefer and Eskinazi [24] plotted the lines of peak vorticity as a function of downstream distance and found that the position of minimum

separation between these lines corresponds to the region where velocity fluctuations are greatest. Bearman [1] did much the same thing for bluff bodies with splitter plates. However the concept of formation length remains ill defined; certainly an exact definition of the formation length and good objective method for its measurement remain to be found.

Still another characteristic length, the diffusion length L_d , was proposed by Gerrard [13]. It is defined as the instantaneous shear layer thickness at the point of strong crosswake shear layer interaction. Gerrard hypothesized that the volume of the formation region is established by a balance between the amount of fluid entrained by the free shear layers and the amount of fluid returned to the formation region in the process of shedding a Kármán vortex. The relative thickness of the shear layer should indicate the amount of fluid entrained by unsteady processes in the shear layer. As Re increases, the decreasing L_t should result in greater entrainment by the separated shear layer, resulting in a decrease of the formation length. It is this decrease in formation length, balanced by the increase in entrainment, (hence more diffuse Kármán vortices) that Gerrard said results in a relatively constant Strouhal number. This in fact was implied by the pitot-tube traverses of Schiller and Linke [25] in 1933.

One must keep in mind that this is merely a hypothesis. The only data on L_d is that presented by Gerrard [14]

giving average and instantaneous layer thicknesses for two Re (5×10^3 and 2×10^4). His method of inferring the instantaneous shear layer thickness was to place a pair of hot wires in a vertical downstream plane corresponding to L_f and spacing them across the shear layer so as to give the greatest difference between the signals at transition wave frequency. The results of this method agreed with his earlier theory.

Wille [30] presented a somewhat different theory for the shedding phenomenon. He noted that the shear layers surround a region of relatively dead fluid and the width of this region is decreasing with increased downstream position. The resulting curved streamlines create a pressure force which is balanced by the inward spiralling of the outer flow. It is a reaction to this curvature which results in the influx of fingers of irrotational flow.

Another tempting approach to the problem is that of inviscid modelling using numerical techniques. The shear layer has been successfully modelled by finely spaced line vortices. Clements [8] considered the flow along a long, rectangular body with sharp separation lines. He showed that the vorticity collected into an organized, periodic structure which suggests the Kármán street. On the other hand, Wille [30] finds it inconceivable that in a real fluid inviscid induction is a primary agent across a wake of width one to two orders of magnitude greater than the vorticity layer thickness.

An often mentioned result of increasing Re is the presence of low frequency fluctuations (an order of magnitude lower in frequency than the Strouhal frequency) in the near vicinity of the cylinder. Bloor [4] mentions that there are always low frequencies present in the near wake except very near the end of the formation region. Gerrard [12] found that for $Re=2 \times 10^4$ there is a random spanwise ± 15 degree tilting of vortex lines, and this tilting changes at a frequency an order of magnitude lower than the Strouhal frequency. Maekawa and Mizuno [18] noted that hot wire signals taken near the separation point had a beat-like amplitude variation at this lower frequency. Mattingly [19] mentioned a low frequency undulation in the separation line. For Re between 2×10^4 and 6×10^4 , spanwise cells of well correlated flow corresponding to the undulated separation line would drift along the cylinder. With increasing Re , the width of these cells would decrease, until the spanwise organization disappeared near $Re=7.5 \times 10^4$. It is interesting to note the work of Keefe [16], who found that by adding end plates to the cylinder and decreasing the spacing between them, the wake between them would become more organized with the resulting fluctuating lift much larger.

In attempts to further understand the presence of low-frequencies, similar experiments utilizing multiple hot wire traces were conducted by Toebes [28] and Gerrard [14]. While the former concluded that the wake pulsates,

the latter concluded that the wake flaps like a flag. As before, more objective experiments seem appropriate.

Recently, several researchers have documented experimental techniques which show promise for the analysis of near wake phenomena. By treating the eddy shedding phenomenon as a nearly periodic process, new insights into this flowfield can be made.

DeCoster and Kibens [9] treated the velocity fluctuations in the wake of a disk as the sum of mean, strictly periodic, and random components. A velocity sensor was placed in the wake at a point of large periodic fluctuations. This signal was filtered to remove high frequency components, and the peak values of the filtered signal were used as a phase reference. The periodic velocity components were then determined by ensemble averaging across many periods of the shedding cycle by using the phase reference signal to initiate each realization of the ensemble.

A similar technique was used by Cantwell [7] in the wake of a circular cylinder. The phase-lock loop was utilized to again determine a phase reference, and this in turn triggered an integrator which produced a ramp of constant slope. However there are distinct limitations to both of these methods due to the deviation of the shedding process from exact periodicity. Deviation of individual cycles from the mean period are not accounted for and smear the phase-conditioned averages.

Objectives

In recent years it has become increasingly evident that Reynolds averaging of the equations of motion is not adequate for a complete understanding of many of the mechanisms in fluid mechanics. In the past, experimental measurements were limited to mean and mean square quantities by the lack of sophisticated instrumentation. Hypotheses often had to be based solely on the subjective interpretation of flow visualization pictures or oscilloscope images of hot-wire signals. Certainly Reynolds averaging pays no justice to the complex flowfield in the wake of a cylinder; on the other hand, even the most experienced researcher is not totally unbiased in his interpretation of raw data.

With the advent of various modern digital data processing systems, the researcher is now able to compute a limitless variety of conditioned and unconditioned statistical parameters to aid in the further understanding of complex flow-fields. But the statistics should be tied into a physical understanding of the problem to avoid getting lost in numbers.

A good portion of the cited literature is an attempt to understand the amplitude and frequency modulated sub-critical Kármán vortex street. The various methods for determining characteristics of the near wake have been rather vague. The following work is an attempt to develop more objective techniques for characterizing the formation region behind a cylinder.

DeCoster and Kibens [9] as well as Cantwell [7] have demonstrated the feasibility of ensemble averaging almost-periodic phenomena across many cycles. However their methods did not account for the random amplitude and frequency modulation occurring in the wake. The approach to be taken in this thesis is slightly different; a signal does not have to be purely monochromatic in order to assign a phase to it. Instead, the shedding process can be treated as a modulated system, with an instantaneous amplitude and phase assigned to it. Then statistics can be determined as a function of phase rather than time. In effect the periodicity can be removed from the flow and the shedding process examined for a single phase. The mechanisms of the near wake region can be examined statistically across many Strouhal cycles, and insight into the low frequency modulation and transport processes can be gained in an objective manner.

Although hot-wire anemometry is a very popular method for the investigation of complex flow-fields, the measurement of a vector quantity is relatively difficult. In order to detect the separated shear layer, a method for distinguishing vortical fluid from the potential free stream is necessary. Schemes for determining vorticity using hot wire probes do exist in the literature, but a thermal tracer technique is chosen as most feasible for the present work. Heat is transferred into the cylinder boundary layer before separation; for a fluid of Prandtl number near one,

the thermal boundary layer should be of the same order thickness as the momentum boundary layer. Hence the vortical fluid in the separated shear layer is "tagged" at its source. Since the boundary layers on opposite sides of the front stagnation line acquire oppositely signed vorticity, a single-sided thermal tagging is ideal for investigating the anti-symmetric Kármán street. The concentration of an easily identifiable scalar (temperature) can be examined for a large number of periods, and the characteristics of the mean periodic rollup of vorticity in the formation region investigated statistically.

Description of Experiment

The primary experiment consists of temperature measurements in the wake of a circular cylinder. The cylinder consists of a 2 in. diameter pyrex tube with an approximately 25 degree arc of its surface used as a resistance heater. The heater is positioned to heat an arc between the front stagnation line and one of the separation lines. Coolant water at the ambient air temperature is circulated through the cylinder to insure that the remainder of the cylinder is at ambient temperature. The cylinder is mounted in the High Speed Test Section of the IIT Environmental Wind Tunnel.

The thermally tagged fluid is detected downstream by a rake of six temperature sensing resistance thermometers. Bridge circuits are used to yield signals proportional to

the difference between the temperature sensed by each wire and the ambient tunnel temperature. The outputs of these bridges are suitable for digitization. The rake probe is mounted in a two dimensional traversing mechanism capable of positioning it anywhere in a plane perpendicular to the cylinder axis. The signal used to determine the phase of the eddy shedding cycle (or phasing signal) is obtained by placing a constant temperature hot wire velocity sensor just outside of the cylinder boundary layer near the separation point. After suitable amplification, the almost sinusoidal signal obtained from this sensor is suitable for digitization.

The temperature as well as the velocity signals are sampled and digitized by the IIT Data Acquisition and Processing System (DAPS), and the time series are recorded on magnetic tape for later processing. The implementation of a continuous acquisition program allows the digital recording of multiple signals over a continuous time interval limited only by the length of a single magnetic tape.

The details of this experimental configuration will be discussed further in Chapter III.

CHAPTER II

ANALYSIS OF SIGNAL PROCESSING

The use of the Discrete Fourier Transform (DFT) for power spectral estimation is discussed, along with the issue of windowing for finite length transforms. Coherence function estimation is also described, and its interpretation in the comparison of signals is considered. The Hilbert transform is presented as a means for determining the instantaneous phase of a modulated signal. The utilization of conditioned probability densities for the characterization of the near wake in phase space is demonstrated, and the use of an additional condition to account for amplitude modulation is considered.

Spectrum and Coherence Estimation

With the advent of the Fast Fourier Transform (FFT) algorithm, the estimation of power spectra through the Discrete Fourier Transform has become increasingly popular. However, since many notational ambiguities exist in digital data analysis, a brief description of the methods used here is provided. The notation is for the most part similar to that used by LaRue and Libby [17], and Bendat and Piersol [2].

Let $z(t)$ be an arbitrary continuous signal which is a function of time, let f_s be the frequency at which z is sampled and digitized, and let N be the total number of samples to be taken. The time interval between samples can be given by

$$\Delta t = 1/f_s \quad (1)$$

and the total sample period by

$$T = N\Delta t . \quad (2)$$

The series of N digital samples can be represented by

$$z_n = z(n\Delta t) \quad (n = 0, 1, 2, \dots, N-1) . \quad (3)$$

However, the sampling process restricts the range of frequencies that can be identified without ambiguity. In order to prevent this aliasing, the original signal must have negligible spectral content above the folding frequency which is given by $f_o = f_s/2$. This can be accomplished by appropriate analog low-pass filtering of $z(t)$ at a cutoff below f_o .

The discrete Fourier transform of the series z_n is defined as

$$Z_r = \frac{1}{N} \sum_{n=0}^{N-1} z_n \exp(-i2\pi rn/N) \quad (4)$$

$$(r = 0, 1, 2, \dots, N-1)$$

where Z_r is in general a complex number which can be represented by

$$Z_r = a_{zr} + ib_{zr} \quad (5)$$

and Z_r corresponds to the discrete frequency

$$f_r = r/N\Delta t . \quad (6)$$

If there is no content in z_n at zero frequency, the single sided power spectral density is

$$G_{zr} = [a_{zr}^2 + b_{zr}^2]N\Delta t . \quad (7)$$

This can be ensemble averaged over many records to give a statistically reliable estimate of the power spectrum.

For a continuous function of time, the Fourier transform is given by

$$Z(f) = \int_{-\infty}^{\infty} z(\tau) \exp(-i2\pi f\tau) d\tau . \quad (8)$$

This implies that $z(t)$ is of infinite duration. However any real signal must be of finite duration (the instrument is switched on at some time and switched off at another). In the process of discretizing a signal, only a finite number of samples can be taken. Even if the duration of the real signal approached infinity, the number of samples per digital record is seldom larger than thousands. Truncation of the real signal corresponds to multiplication by a boxcar function, which is defined

$$u(t) = \begin{cases} 0, & t < 0 \\ 1, & 0 \leq t \leq T \\ 0, & T < t \end{cases} . \quad (9)$$

A property of the Fourier transform is that multiplication of two functions in one domain results in their convolution in the other domain. The Fourier transform of $u(t)$ gives

$$|U(f)| = 2T \frac{\sin 2\pi fT}{2\pi fT} \quad (10)$$

and it is this function which is effectively convolved with the Fourier Transform of the infinitely long signal when the signal is truncated to length T . The function $u(t)$ is called a window, and its effects are leakage and loss of

resolution. If the boxcar function were extended to infinite duration, $U(f)$ would approach the Dirac δ function. However, the effect of the boxcar function can be seen in its power spectrum (Fig. 3). The resolution of the window is determined by the width of the main lobe (Δf in this case). The leakage, or spectral content resulting from contributions outside the main lobe, is readily apparent. Although the boxcar function has good frequency resolution, it is undesirable because of leakage.

Various window functions other than $u(t)$ have been proposed. The problem is one of determining a finite function in the time domain which yields the desired response in the frequency domain. One such function is the Hamming window, with the power spectrum shown in Figure 4. Side lobe leakage is reduced considerably (99.96% of the spectral contribution comes from within the main lobe), but the width of the main lobe is doubled. This result is in general true for all window functions; i.e. leakage is reduced at the cost of resolution. The time domain representation of the Hamming window is

$$u_H(t) = 1 - .852 \cos(2\pi t/T) \quad (11)$$

and this was applied to all data records used in power spectral estimation before transformation.

Cross spectral estimates can be used to compare two signals. Given the time series y_n and z_n , with their corresponding discrete Fourier transforms Y_r and Z_r , the cross spectrum is defined

$$C_{y_zr} = (\bar{Y}_r Z_r) N \Delta t = c_{y_zr} + i q_{y_zr} \quad (12)$$

where $\bar{}$ denotes complex conjugation. The one sided cross-spectral density is given by

$$G_{y_zr} = (c_{y_zr}^2 + q_{y_zr}^2) N \Delta t, \quad (13)$$

where G_{y_zr} indicates how well y_n and z_n are correlated at frequency f_r . Although the cross spectrum presents exactly the same information as its Inverse Fourier Transform, the cross correlation, it is more easily interpreted than the cross correlation for signals where there is any periodicity. The coherence function, defined as

$$A_{y_zr}^2 = G_{y_zr}^2 / G_{y_yr} G_{z_zr} \quad (14)$$

is a normalized cross spectrum function that ranges between zero and one. For A_{y_zr} equal to unity, there is a constant phase relationship between y_n and z_n at f_r for all data records considered, which implies a linear relationship between y_n and z_n . Care must be taken, however, that a sufficient number of records be included in the ensemble average, for in the limiting case of a single record ensemble for y_n and z_n , A_{y_zr} is unity for all r .

Processing of Narrow-Band Signals

The Kármán vortex street in the subcritical regime is a process which departs from strictly monochromatic behavior. Attempts have been made in recent years to study this flow field as a function of phase rather than time using "phase mean" computations. For a monochromatic process, it is possible

to define an instantaneous phase, and this phase can be used to compare events occurring in many cycles of a periodic process. Unfortunately, in fluid mechanics most processes are not truly monochromatic unless they are driven externally (for example, flow over a helicopter blade). The vortex street is an amplitude and phase modulated polychromatic process, and previously implemented methods for determining the instantaneous phase of this process have assumed a quasi-monochromatic behavior. A method will be presented here which is free from the limiting assumptions of the earlier techniques.

Figure 5 is the power spectral density of the signal obtained from a hot-wire sensor placed in the potential flow near the separation point of the boundary layer on a circular cylinder. Superimposed on what might be termed a random background spectrum is a peak of finite width centered at frequency f_{St} , the Strouhal frequency. The velocity fluctuations which contribute to this peak are a result of the flow induced by the Kármán vortices, and are indicative of the vortex formation process. The finite width of the peak is characteristic of a process which is modulated either in frequency or amplitude or both.

If the signal is appropriately bandlimited to remove the random background signal, the remaining polychromatic signal can be considered to have an instantaneous frequency $\omega(t)$, and an instantaneous amplitude $A(t)$. The phase can then be defined as

$$\phi(t) = \int_0^t \omega(\tau) d\tau. \quad (15)$$

The following analysis will demonstrate a method for the determination of $\phi(t)$.

The methods used by DeCoster and Kibens [9] as well as Cantwell [7] contain assumptions about the shedding process which are not necessarily valid. The first assumption is that the instantaneous peaks in the modulated signals (corresponding either to pressure or velocity) occur at a constant phase, and this phase is used as a reference. This is only true when the amplitude modulation is small enough to be neglected. Results of the present investigation (see Chapter V) indicate amplitude modulations of 50 percent.

A second and more crucial assumption is that of quasi-monochromatic behavior. Essentially, a mean frequency is computed and it is assumed that the frequency does not change significantly from this value. This can be valid only if all periods of the shedding process are of equal duration. The current work indicates that the frequency modulation is about ten percent, resulting in periods of varying length. Consequently, the phase computed by the earlier methods will not in general equal 2π at the end of a period and the phase conditioned statistics will be smeared.

The technique used in this thesis involves the creation of a complex rotating vector from which ω , ϕ , and A can be computed. This method is not limited by the assumptions implied in previous work.

Assuming one has a properly sampled (i.e., no aliasing) time sequence of the signal to be used as a phase reference, the first task is to bandlimit the signal to remove spectral content outside of the band of interest. Although it is possible to apply an analog bandpass filter to the signal before sampling, non-recursive digital filters offer distinct advantages for this application. Since a phase angle is the desired quantity to be measured, any signal processing which introduces phase shifts is undesirable. Analog filters produce a phase shift in the signal and it can be argued from a causality standpoint (i.e., a signal cannot be known before it occurs) that a real-time analog filter without phase shifts is impossible to construct. However, digital processing does not have this limitation. The causality requirement does not apply to a stored time series because it is possible to look "both directions" in time. It can be shown (see Rabiner and Gold [22]) that a non-recursive filter will impart a phase shift that is identically zero if the time domain representation of the filter function is symmetric about $t = 0$. This is not in general true of the more computationally efficient recursive digital filters.

In order to understand the way in which a digital filter works, it is convenient to think in terms of the Fourier transform of a time series. Consider a discrete filter response H_r ; the filtering of a time series z_n to get z'_n can be thought of in terms of the frequency

domain representation

$$Z'_r = Z_r H_r \quad (16)$$

where Z'_r is the Fourier transform of z'_n . However, multiplication in the frequency domain corresponds to convolution in the time domain so the filtering can be accomplished by direct convolution with the filter impulse response, h_n ; i.e.,

$$z'_n = z_n * h_n \quad (17)$$

where $*$ denotes convolution. The problem then becomes one of finding functions that are finite in time and correspond to the desired filter frequency response. This will be discussed further in Chapter IV.

Mathematical techniques have been developed to handle bandlimited functions. The following description of the complex representation of real polychromatic fields is taken from Born and Wolf [5] and follows the theory of partially coherent light as introduced by Wolf. Prior to this theory, optical theory was limited primarily to either monochromatic or purely random analysis, and this bears an interesting parallel to experimental fluid mechanics. The mathematical treatment employed in the theory of partial coherence has been applied to other branches of physics in connection with correlation techniques for measurements of radio stars, exploration of the ionosphere by radio waves, and the analysis of partial polarization.

In discussing monochromatic wave fields, it is useful to regard a real wave function as the real part of an associated complex wave function. For a polychromatic field it will again be useful to employ a complex representation, which may be regarded as a natural generalization of that used with monochromatic fields.

Let $z(t)$ be a real signal at a fixed point in space for which the Fourier Transform exists. Then

$$z(t) = 2 \int_0^{\infty} \alpha(f) \cos[\psi(f) - 2\pi ft] df \quad (18)$$

With $z(t)$ a complex function is associated

$$z^a(t) = 2 \int_0^{\infty} \alpha(f) e^{i[\psi(f) - 2\pi ft]} df \quad (19)$$

Then

$$z^a(t) = z(t) + iz^i(t) \quad (20)$$

where

$$z^i(t) = 2 \int_0^{\infty} \alpha(f) \sin[\psi(f) - 2\pi ft] df \quad (21)$$

The functions $z^i(t)$ and $z^a(t)$ are uniquely specified by $z(t)$, $z^i(t)$ being obtained from $z(t)$ by replacing the phase $\psi(f)$ of each Fourier component by $\psi(f) - \pi/2$. The integrals (18) and (21) are said to be allied Fourier integrals, or associated functions, or conjugate functions and may be shown to be Hilbert transforms of each other as proved by Titchmarsh [27]:

$$z^i(t) = \text{Hi}[z(t)] = \frac{1}{\pi} \int_{-\infty}^{\infty} \frac{z(\tau)}{\tau - t} d\tau \quad (22)$$

$$z(t) = \text{Hi}^{-1}[z^i(t)] = -\frac{1}{\pi} \int_{-\infty}^{\infty} \frac{z^i(\tau)}{\tau-t} d\tau . \quad (23)$$

The Hilbert transform, then, is given by the convolution relation

$$\text{Hi}[z(t)] = -\frac{1}{\pi t} * z(t) . \quad (24)$$

This complex representation is used frequently in communication theory, where $z^a(t)$ is called the analytic signal belonging to $z(t)$. The concept of an analytic signal was introduced by Gabor [11], and the name is derived from the fact that, provided z satisfies certain general regularity conditions, the function $z^a(\zeta)$, considered as a function of the complex variable ζ , is analytic in the lower half of the complex plane.

In the present application, the spectral amplitudes will only have appreciable values in a small frequency interval centered at the mean (Strouhal) frequency. The analytic signal then has a simple interpretation. Expressing $z^a(t)$ in the form

$$z^a(t) = A(t)e^{i\phi(t)} = z(t) + iz^i(t) \quad (25)$$

the instantaneous amplitude of the modulating envelope $A(t)$, the instantaneous phase $\phi(t)$, and the instantaneous angular frequency are computed as

$$A(t) = \{[z(t)]^2 + [z^i(t)]^2\}^{\frac{1}{2}} \quad (26)$$

$$\phi(t) = \tan^{-1}[z^i(t)/z(t)] \quad (27)$$

$$\omega(t) = \partial\phi(t)/\partial t . \quad (28)$$

This is demonstrated graphically in Figure 6, which is adapted from Bracewell [6].

A truncation problem similar to the bandpass filter case arises in computing the Hilbert transform. The function $-1/\pi t$ must be approximated by a finite length time domain representation which yields the desired response in the frequency domain. This will be discussed further in Chapter IV.

Conditional Probability

As discussed in the previous section, it is possible to determine the instantaneous phase, frequency, and amplitude of the modulated eddy shedding process. If the process were purely periodic, that is, if it repeated itself exactly from cycle to cycle, examining the wake at a particular phase for any cycle would be representative of the wake at that phase for all cycles. On the other hand, if the shedding process were entirely random, the statistics would not involve phase.

However, in this Reynolds number range the wake is not adequately described by either of these classifications; instead, it can be characterized as a randomly modulated (in frequency and amplitude) polychromatic process with turbulence superposed. If the periodicity is removed through the creation of a phase related signal and if the wake is examined conditionally based on this phase, the sampled data can be treated as a random process. If another

condition is added, i.e., if the wake is examined conditionally based upon amplitude as well as phase, some insight into the modulation process might be gained.

Consider $\theta(x,y,t)$, the time dependent temperature difference between a point in the wake and the ambient free stream. Since the following discussion applies to each spatial position, the spatial dependence will be temporarily omitted. Also, with the computation of phase, time can be transformed into phase, hence

$$\theta = \theta(\phi) . \quad (29)$$

The conditional probability density $p(\theta'|\phi',A')$ (the probability of θ' given ϕ' and A') can be estimated from a discrete time series by

$$p(\theta'|\phi',A') = \text{Prob}[\theta' < \theta(\phi) \leq \theta' + \Delta\theta'] \quad (30)$$

given that

$$\phi' < \phi \leq \phi' + \Delta\phi'$$

$$A' < A \leq A' + \Delta A'$$

where $\text{Prob}[]$ is an appropriately normalized number density.

This statistic can be calculated to yield a probabilistic picture of the temperature distribution in the wake as a function of phase and amplitude. However, for the results presented in Chapter V, the amplitude dependence is dropped. In other words, A' is set equal to zero, and $\Delta A'$ is set equal to infinity.

These probability densities can be integrated between temperature levels to yield the probability that the

temperature falls between those levels, that is

$$P(\theta_1 < \theta < \theta_2 | \phi', A') = \int_{\theta_1}^{\theta_2} p(\theta' | \phi', A') d\theta' . \quad (31)$$

For the results presented in Chapter V, θ_2 is set at infinity and only θ_1 is varied. The resulting probabilities are plotted as a function of the x and y spatial coordinates to yield an overall picture of the wake. If θ_1 is set relatively high, only the least diffused vorticity will enter into the calculation, whereas if θ_1 is set just above ambient temperature, any vortical fluid will be detected.

CHAPTER III

EXPERIMENTAL FACILITIES AND INSTRUMENTATION

The various flow facilities used for experiments in air and water are described. The cylinder model used for the main experiment is presented, and adjustments for various non-ideal situations are discussed. A description of the instrumentation and data acquisition system is also included.

Flow Visualization Wind Tunnel

The IIT Flow Visualization Wind Tunnel was used to conduct visual qualitative measurements of the sidewall boundary layer influence on the flowfield in the near vicinity of the cylinder. It is a low velocity, open circuit facility which is driven by the building exhaust system. The test section (6 in. x 29 in. x 8 ft.) is made entirely of clear plexiglass and is preceded by a two dimensional 18:1 contraction (see Fig. 7).

Reynolds number matching was accomplished using two different cylinder models. For investigation of the stagnation region, a two inch diameter cylinder model with a length to diameter ratio of three was constructed. These dimensions were chosen because the tunnel sidewall boundary layers of the Flow Visualization Wind Tunnel are of the same order of thickness as those in the Environmental Wind Tunnel. Visualization was achieved using an oil evaporation technique. A nichrome ribbon was mounted

vertically in the test section approximately six inches upstream of the cylinder and oil drops were run along its surface. By passing a current through the ribbon, the oil was evaporated and convected downstream. This resulted in a dense, thin vertical sheet of smoke which followed the streamlines in the stagnation region of the cylinder. A horizontal plane of light was created using a strobe light and slotted masks. By careful arrangement of the light and smoke, an individual streamline could be visualized and photographed.

A one inch cylinder with an aspect ratio of six was used for wake visualization. Smoke was injected through stainless steel hypodermic tubing into the region immediately behind the cylinder to determine the effect of the sidewall boundary layer. The purpose of the smaller cylinder is to more nearly approximate the aspect ratio of the cylinder used in the main experiment.

Water Table

Visual diagnostic observations of temperature probe characteristics were made in the IIT Water Table, shown in Figure 8. This facility can produce flow rates up to one foot per second through an adjustable test section. This test section is preceded by two aluminum honeycombs followed by a two dimensional contraction. The flowfield is illuminated from below and mirrors allow simultaneous top and side views of the test section.

The ability to duplicate the quantity U_{∞}/v allowed

Reynolds number matching between the experiments in air and water for identical cylinder diameters. For the diagnostic measurements, an aluminum cylinder with axial slits for the injection of dye was constructed. The cylinder was mounted with its axis normal to the floor of the test section, thus permitting a gravity feed for the dye.

Environmental Wind Tunnel

All quantitative measurements were conducted in the high-speed test section of the IIT Environmental Wind Tunnel, shown in Figure 9. It is a closed loop tunnel, with two independent test sections. The high speed test section (3 feet high, 2 feet wide and 10 feet long) is a low turbulence facility, with a maximum air velocity of 100 feet per second. Upstream turbulence manipulators consist of a honeycomb of packed plastic soda straws followed by 10 fine mesh screens. The flow then proceeds through a 4:1 contraction and into the test section. A screen immediately downstream of the test section raises the tunnel internal pressure slightly above atmospheric, thereby eliminating the possibility of undesirable inward jetting of room air. As an additional precaution, unnecessary slots and holes in the tunnel walls were sealed with tape prior to the experiment.

Although wind tunnels are convenient facilities for experimental work in fluid mechanics, objectivity demands that certain questions pertaining to experimental conditions be considered. The finite length cylinder and its interaction with tunnel sidewall boundary layers will be dis-

cussed later. Fluctuations in tunnel free-stream velocity present another problem. Although the Environmental Wind Tunnel is a low turbulence facility, Fabris [10] noted two types of free-stream velocity fluctuation; these include quasi-periodic, very low frequency (.1 - 1 hz) fluctuations and longitudinal velocity fluctuations at a higher frequency (5 - 10 hz). Because free shear flows exhibit great amplification of disturbances, further investigation into these flow nonuniformities is warranted.

The low frequency aspects of these phenomenon makes them especially suited to digital processing, as most analog instruments do not have sufficiently long time constants or good low frequency response. Two data acquisition runs were made at free stream velocities of 4 and 21.5 feet per second, with analog information being digitized and stored on magnetic tape using the IIT Data Acquisition and Processing System (see last section, this chapter). These velocities are considered to be the extremes of the useable range for this experiment. A velocity of 4 feet per second is the lowest velocity at which the tunnel is free of extreme velocity fluctuations or surging, whereas the upper velocity limit is dictated primarily by the onset of probe vibration..

The objectives of the diagnostics are twofold. The first is to determine whether a relationship exists between ambient room pressure and tunnel free stream velocity. As the building which houses the wind tunnel has a forced convection air conditioning system, the room pressure can fluc-

tuate greatly depending upon conditions at other locations in the system. A possible Helmholtz instability between the tunnel and room has also been postulated.

The second objective is to determine if there is a relationship between the low frequency free stream velocity fluctuations and the velocity fluctuations in the vicinity of the cylinder model. Although low frequency pressure and velocity fluctuations in the vicinity of the cylinder have been previously documented (Bloor [3] , Hanson and Richardson [15], Gerrard [14], and Maekawa and Mizuno [18]), the possibility of a relationship to free stream velocity fluctuations has not been investigated.

Two sets of data were taken at each free stream velocity. The first consists of simultaneous room pressure and wind tunnel free stream velocity measurements, while the second consists of free stream velocity measurements with simultaneous velocity measurements near the cylinder boundary layer separation point. The instrumentation is shown schematically in Figure 10.

The free stream velocity fluctuations were measured using a .00015 inch diameter by .1 inch long tungsten hot wire mounted normal to the flow approximately 7 cylinder diameters upstream of and 2.5 diameters above the centerline of the cylinder. The sensor was driven by a DISA 55D01 constant temperature anemometer, with the signal subsequently processed by a DISA 55D10 linearizer and a DISA 55D25 auxiliary unit to obtain a linearized signal with low d.c.

content. An amplifier and low pass filter conditioned the signal for proper digital sampling. A similar circuit was used to measure the velocity fluctuations near the cylinder separation point, with the sensor again mounted normal to the flow approximately $1/8$ diameter above the cylinder near the flow separation point.

Room pressure fluctuations were measured using a Validyne DP45 very low range differential pressure transducer. The differential transducer was sealed at one input tap in order to measure absolute pressure and the d.c. component was removed by an adjustment in the carrier demodulator used to drive the transducer. An analog amplifier followed by a low pass filter conditioned the signal for sampling, with the gain adjusted so as to make full use of the range of the analog to digital converter in the data acquisition system.

Although it is possible to calculate many statistical quantities from the discrete time series, certain statistics yield better insights into the problem at hand. In order to determine if there is some simple relationship between free stream velocity, U_∞ , the velocity near separation, U_ϕ , and room pressure P_r at particular frequencies, coherence functions were calculated. The results of these measurements will be discussed in Chapter V, and the measurements are summarized in Table 1.

Cylinder Model

The cylinder used for the main experiment consists

of a pyrex glass tube (2 in. diameter x 22 in. long x .125 in. wall thickness) with a 25 degree arc of its surface coated with a metallic gold ohmic heater (see Fig. 11). The gold coating is produced by firing a metallo-organic compound to the surface at high temperatures resulting in a thin film of precious metal about 1000 angstroms thick. Imperfections in the application technique resulted in minute perforations in the film, but a single layer of the coating is suitable as an electrical conductor. The particular film used for this experiment has a resistance of 27 ohms and was driven using a Hewlett Packard 6255A power supply at 40 volts, for a net power input of about 60 watts. Electrical connection to the film was accomplished through the use of adjustable hose clamps.

As a result of early experiments, it was discovered that the heating of the cylinder is not localized to the gold strip. Although pyrex is not a good conductor of heat, under steady state conditions the entire cylinder attains a temperature slightly above ambient. This is undesirable because the thermal tag should only be applied to vortical fluid from one of the cylinder boundary layers. In order to determine possible solutions to this problem, a steady state, two dimensional finite difference model of the cylinder heat transfer configuration was constructed and run on the IIT UNIVAC 1108 computer. For the sake of simplicity, the air convection coefficient is assumed to be constant over the surface of the cylinder at the maximum Re

of interest ($Re = 20,000$ and $h = .05 \text{ BTU/hr-in}^2\text{-}^\circ\text{F}$). The cylinder is modelled by a two dimensional axisymmetric half-cylinder with 5 nodes in the radial direction and 36 nodes in the tangential direction (see Fig. 12). The gold strip is represented by three surface nodes having internal heat generation. The finite difference equations were solved using a Gauss-Seidel iteration technique, and the results normalized with the maximum surface temperature (Fig. 13). The conclusion which can be drawn from this numerical solution is that the increase in surface temperature due to the heater does not become negligible until angles of ± 100 degrees from the center of the strip.

The circulation of coolant water through the center of the cylinder was proposed as a possible solution to the heating problem. Limited by a maximum water flow rate of 5 gallons per minute, a Reynolds number based on cylinder inside diameter of about 10,000 was expected, with a resulting heat transfer coefficient $h = 1.25 \text{ BTU/hr-in}^2\text{-}^\circ\text{F}$. The heat transfer simulation was run for two conditions; in each case the water is at the ambient air temperature, with zero and maximum air flow rates in respective runs. The results demonstrate that the water is the dominant heat transfer agent, with negligible change in the results over the entire range of air convection coefficients, and that the use of coolant water can limit the heating of the cylinder surface to a reasonable ± 30 degree arc of the surface (see Fig. 13). Further runs of the simulation program also demonstrate that

the cylinder surface temperature is essentially equal to the water temperature at positions far away from the heating strip.

The coolant water system was implemented as a recirculating loop using a large volume of water. A problem initially encountered with the coolant was a temperature rise due to the dissipation of fluid kinetic energy.

Although the wind tunnel temperature also increases with time, the coolant temperature increases at a greater rate (Fig. 14). A metal container of ice was suspended in the tank of water, and by varying the depth to which the container was immersed, the amount of heat removed from the water was regulated. The large volume of water (100 gallons) effectively damped the system, and through periodic monitoring of the wind tunnel and water temperatures with sensitive mercury thermometers, the difference between the two temperatures never exceeded .04 degrees Celsius. Therefore, the unheated portion of the cylinder remained within .04 degrees of the ambient tunnel temperature.

Another difficulty results from the cylinder interaction with the wind tunnel side wall boundary layers. This interaction must be minimized if the experiment is to model the wake of a two-dimensional cylinder. The stagnation region at the front of the cylinder results in a stretching of the boundary layer vorticity more commonly known as a

horseshoe vortex. This results in secondary flow in the axial direction which is towards the wind tunnel walls in front of the cylinder and away from the walls in the cylinder wake. Shimizu [26] made axial traverses of crossflow turbulence intensity in the stagnation region and his measurements show nonuniformities which suggest the presence of horseshoe vortices.

As mentioned earlier, qualitative measurements using visualization techniques have been made in the near vicinity of the cylinder. In order to reduce the stangation effects, various circumferential barriers were placed on the cylinder near the tunnel sidewalls and tested. The results are summarized in Figure 15, which is a reproduction of multiple exposure photographs of streamlines in the plane of the cylinder axis. The configuration shown in 15(a) is the cylinder without a barrier, showing the streamline curvature well outside of the boundary layer. One of the small barriers tested is shown in Figure 15(b), where streamline curvature is reduced but not eliminated. The design which yielded the best results is shown in Figure 15(c). This barrier minimizes streamline curvature outside of the boundary layer without creating additional vorticies due to its own boundary layer, which is the consequence of larger barriers.

Additional observations were made in the wake of the cylinder. The ring barrier proved to be insufficient in the wake, and the near wake tended to slosh axially

as the result of bursts from the sidewalls. A combination ring and plate design shown in Figure 11(c) proved to be the most satisfactory solution to the cylinder-sidewall boundary layer interaction problem. Smaller plates permitted the curling over of longitudinal vorticity from the wall boundary layer into the wake, while tests of the final design indicate that the boundary layer vorticity is prevented from entering the wake.

Phasing Signal

In order to generate the instantaneous phase and amplitude within each shedding cycle as discussed in Chapter II, a signal indicative of the wake periodicity must be generated. Although previous researchers have used hot-wire velocity signals from within the wake (DeCoster and Kibens [9]) or surface pressure signals from the cylinder (Cantwell [7]), the signal from a hot wire in the non-vortical free stream near the separation point proved to be an attractive alternative. Most of the energy content of this signal is within a narrow spectral band centered at the Strouhal frequency (see Fig. 5). The maximum spectral energy is about 20dB above the content at nearby frequencies outside of the peak.

The hot-wire was driven in the constant temperature mode by a DISA 55D01 Anemometer, with bias and gain provided by an operational amplifier circuit (Fig. 16). The need for a filter is eliminated due to the fact that the signal has negligible energy content at frequencies above the Strouhal

peak. The relatively noisy linearizer is also eliminated because the amplitude of the velocity fluctuations is small enough to have a effectively linear output from the anemometer. The velocity calibration curve is given in Figure 17.

The hot wire probe was mounted in a milling machine indexing head for ease of positioning. To eliminate the wake effect of the phasing probe, the temperature and phasing probes were separated in the crosswake direction by $3/4$ inch, which was experimentally verified to be acceptable.

Temperature Measurement

In preliminary experiments the temperature measurements in the wake were made using a 10 ohm tungsten sensor driven by a commercial constant current unit. However, this system proved to be undesirable because of poor frequency response, low signal to noise ratio and low temperature sensitivity. The sensitivity is a particularly important factor, as the temperature difference between the heated air and the ambient tunnel temperature is limited by buoyancy effects and the maximum nondestructive surface temperature of the ohmic heater. Also, the commercial unit can only indicate absolute wake temperature, and this is misleading in the presence of a slowly changing free stream temperature as is experienced in the Environmental Wind Tunnel.

A study of several bridge circuits was conducted, and these results are summarized in Wlezien and Way [31]. The final design is a six channel differential resistance

thermomenter, which utilizes a circuit known as the "broken bridge". The multiple channel configuration was chosen to allow the use of a multiple sensor probe for characterization of the wake temperature distribution. The sensors are .000025 inch diameter by .1 inch long Platinum - 10% Rhodium wires with a resistance of approximately 1000 ohms. Although these sensors are extremely fragile, they exhibit high sensitivity and good frequency response (order of 1-2 khz). The circuit configuration which is shown in Figure 18 utilizes a single reference sensor to monitor ambient temperature, and provides outputs proportional to the difference between the temperature of each sensor and freestream temperature. The circuit has a sensitivity of 3.94 volts per degree Celsius for a sensor current of approximately 88 μ A, which results in negligible velocity sensitivity; however, this low sensor current can result in extraneous noise pickup. Good electrical shielding is of primary importance for proper circuit operation, and a double shield configuration adapted from Morrison [21] results in a noise level equivalent to .01 $^{\circ}$ C RMS. Additional stability and noise reduction is accomplished by physically isolating the power supply from the bridge circuits and by providing the bridge input voltage from a 1.4 volt mercury battery.

In order to simplify calibration of the sensors and to produce almost linear temperature response, the sensors are constructed so as to have a resistance within one

percent of 1000 ohms. As a result, the sensors have almost identical linear temperature response when all outputs have the same bias voltage (Fig. 19). The wire used for the sensors has a Platinum - 10% Rhodium core with an outer jacket of silver. The silver is selectively etched using a 30% Nitric Acid solution to produce the sensor, with the resistance proportional to the length of the etched section of the wire. An ohmmeter can be used to monitor the etching process, but care must be taken to insure silver is not replated onto the sensor by the meter current.

Two attempts were made at constructing a six-wire parallel sensor probe. The probe is designed to rigidly hold six wires parallel to each other in a single plane with a separation of .1 inch. Flow visualization diagnostic measurements have been conducted in the IIT Water Table using dye in water and the results are summarized in Figure 20. The original probe (Fig. 20(b)) has a large stagnation region, and this results in an undesirable disturbance of the delicate free shear layer. Dye injected into the boundary layer is driven into the region immediately behind the cylinder as a result of the large stagnation region in front of the probe. On the basis of these results, a minimum stagnation probe was designed, and the visualization test of this new design did not show any noticeable disturbance to the flow (see Fig. 20(c)).

The final probe (Fig. 21) consists of a two sided circuit board with conductors etched into the copper

coating and jewelers broaches used as sensor supports soldered to pads at the edge of the board. The six inch ruler provides a scale for the probe in Figure 21. This board is mounted parallel to the mean flow to present a minimum stagnation region, with the broaches extending from the board at a 45 degree angle. The tips of the broaches were aligned in a specially built jig to assure proper spacing between the sensors. However, the sensors have negligible tensile strength and any slight probe vibration is amplified by the long broaches, resulting in sensor destruction. This problem was solved by gluing fine glass fibers across the broaches in a truss-like structure using cyanoacrylate adhesive, and as a result the six sensor probe lasted the entire series of experiments. A photograph of the overall experimental configuration with cylinder, end plates, phasing sensor and temperature probe is shown in Figure 22(a). The temperature probe is mounted on a stainless steel tube of oval cross section, with a three inch offset to reduce flow interference from the support. The probe support is held by a two dimensional traversing mechanism mounted above the wind tunnel test section. Vertical probe positioning is accomplished using a Starrett dial indicator accurate to ± 0.001 inch, while a scale with .01 inch divisions is used for horizontal positioning. The probe reference position is determined by marks on each side of the test section in conjunction with an alignment telescope.

Data Acquisition and Processing System (DAPS)

The IIT Data Acquisition and Processing System was used to sample and digitize analog data and to extract information from the data through digital processing techniques. The system is built around a PDP 11/10 processor and is shown schematically in Figure 23. A magnetic tape unit is used for storage and retrieval of data, and a Tektronix model 4010-1 graphic display and a model 4631 hard copy unit provide user interaction as well as a plotting capability. Other peripherals include a 60 cycle line clock, a programmable clock, a hardware multiply/divide unit, and a 16 channel 12 bit analog to digital converter capable of a 100 khz sampling rate. A design feature of the PDP 11/10 system is its UNIBUS, which allows interaction between system units without using the central processor. This results in an extremely flexible peripheral device handling system. The acquisition system as well as the analog instrumentation for the experiment is shown in Figure 22(b) .

CHAPTER IV

DATA PROCESSING TECHNIQUES

The acquisition and sampling of analog signals is considered and the various acquisition routines are described. The implementation of the computational techniques of Chapter II is presented with a discussion of the limitations imposed by finite length time series. Digital estimation of power spectra is demonstrated, and a finite impulse response filter and Hilbert transformer are presented. An inter-computer processing technique for the estimation of statistics is also presented, and the extent of errors in the data and computations is examined.

Acquisition of Time Series

Due to variations in requirements, three different acquisition programs were used to sample analog signals. The flexibility of the DAPS allows the user to tailor programs to the particular needs of the problem at hand. For the tunnel diagnostic measurements, the data is used to estimate spectra, hence the acquisition can be done in non-contiguous blocks. This actually aids convergence of the ensemble smoothing of the spectral estimates. The acquisition program written by J.L. Way is a general purpose, user oriented program which can be used to acquire data in discontinuous blocks. Essentially, sampling proceeds until the memory of the computer is exhausted,

the data is written on magnetic tape, and the process is repeated.

In order to easily perform diagnostic measurements in the wake, this program was modified to plot the acquired data on the graphic display unit. Hence multiple channels of data can be visually examined, which is desirable when working with the six sensor temperature probe.

The third acquisition program is also a modification of a program written by J.L. Way, and it allows continuous acquisition of long blocks of data, which facilitates the proper filtering of time series. For this program, the computer memory is divided into two buffers; acquisition proceeds until one buffer is full, then the acquisition is switched to the second buffer while the first buffer is recorded on tape. This program is made possible by the unique architecture of the PDP computer, and the length of a continuous time series is limited only by the amount of data which can be stored on a single magnetic tape.

A problem often encountered in sampling multiple channel data is the total time necessary to sample and digitize a sequence of channels, resulting in a non-simultaneous, or time-skewed, sampling of the channels. For the DAPS, the time needed to sample and digitize a single channel is about $20\mu\text{s}$, which results in a time delay of $120\mu\text{s}$ between the first and last sample for a

sequence of seven channels. However, the DAPS digital to analog converter has four simultaneous sample and hold amplifiers, which can be used to reduce the net delay to 60 μ s.

Data acquisition runs were made at three Reynolds numbers of interest using the continuous acquisition program. Although the data from run 1A is the only data analyzed here, the acquisition of data for all three runs is summarized in Table 2. Due to the variation in Strouhal frequency, the sampling rates were adjusted so that the number of samples per Strouhal period is maintained at approximately 74. The number of samples per probe position was also kept a constant 15,300 which corresponds to about 200 Strouhal cycles of data at each probe position. Data was acquired at approximately 80 positions in the wake, which were determined on the basis of diagnostic runs. The sensor positions for run 1A are indicated in Figure 24. An entire run for a single Re requires approximately two hours, a period over which the experiment can be well controlled.

Spectral Estimation

Power spectral estimates were made using the DFT as described in Chapter II. The transforms were calculated using the IBM SSP Fast Fourier Transform subroutine HARM on the Univac 1108 computer, and the resulting ensemble averaged spectra were written on magnetic tape in PDP 11/10 integer format for subsequent plotting by the DAPS.

Cross spectral estimates were also computed and ensemble averaged, with the coherence determined from the averaged spectra and cross spectra.

Computation of the spectral estimates requires a certain amount of care. For a fixed amount of data, a balance between resolution and confidence level must be chosen. If high resolution is desired, the spectral estimates will have a large variance, whereas low variance can only be achieved with lower spectral resolution. This situation is analogous to the Heisenberg Uncertainty Principle in quantum physics.

The data for each signal in the wind tunnel diagnostic runs was taken in 20 blocks of 1024 samples. Originally, 1024 point transforms were tried, but this resulted in a large variance in the coherence function estimates. However, these functions became relatively smooth when the data blocks were subdivided and 256 point transforms taken. Spectra calculated from two independent sets of data exhibit good reproducibility (see Chapter V).

Filter and Hilbert Transformer Implementation

Given a filter response in the frequency domain, the time domain representation will in general be infinite in length. Recursive filter structures can be implemented to yield a half infinite filter impulse response, but these will result in undesirable phase shifts. Another approach, known as finite impulse response filtering, is an approximation of the infinite filter impulse response h_n by a

finite sequence h_m . A naive way to determine h_m is to simply truncate the infinite sequence, i.e.

$$h_m = \begin{cases} h_n, & |m| \leq M \\ 0, & |m| > M. \end{cases} \quad (32)$$

This truncation can lead to large errors in the frequency response due to Gibbs phenomenon. However, there are optimization programs which will yield the best filter response based on design parameters such as frequency response, filter length, and ripple.

One such optimization program was written by J.H. McClellan and is listed in Rabiner and Gold [22]. Given a finite filter length and the magnitudes within each frequency band, the program generates an optimal equiripple filter. This program has been used to generate the filters used in the present work.

A sampling rate of 74 sequences per Strouhal cycle, increased the difficulty of designing an adequate digital bandpass filter for the phasing signals. The Strouhal frequency is almost two orders of magnitude lower than the sampling frequency, hence the desired digital filter must have sharp changes in amplitude response in a relatively small frequency band (see Fig. 25). This can only be achieved by using a very long filter impulse response. From the earlier discussion of aliasing, it can be seen that only two samples per cycle are needed to completely describe a signal of a particular frequency. Noting the spectrum of Figure 25, it can be seen that the

spectral content could be better represented if the sampling rate were reduced by a factor of eight. Hence the signal is oversampled, and the sampling rate must be effectively reduced through decimation of the data before a reasonable filter can be constructed.

Decimation by eight, that is, using only every eighth value of the phasing signal time series, yielded a more reasonably sampled signal (see spectrum of Fig. 5), but this decimation cannot in general be carried out blindly or aliasing may result. If the signal has non-negligible spectral content at frequencies higher than half the new sampling frequency, there will be aliasing. For the present data, however, the spectral content above the new folding frequency is negligible, and the decimation can be carried out directly.

The bandpass filter used to process the phasing signal for Run 1A is shown in Figure 26. Note that the frequency in Figure 26 is normalized with the sampling frequency to remove the sampling rate dependence of the filter response. This filter has a 63 point impulse response and a maximum magnitude error in the frequency domain of only 1.1 percent. This design was chosen after several runs of the optimization program; a general conclusion is that low error can only be achieved at the cost of filter length and sharpness of the band cutoffs. Note, however, that even with the low error achieved in this filter, the magnitude response drops 40 db in a frequency band

corresponding to about five percent of the sampling frequency.

The Hilbert transformer is very similar to the bandpass filter in that it also has an infinite impulse response. The discrete Hilbert transform is then a finite length impulse response which approximates the infinite duration function. The primary problem is that the ideal Hilbert transformer frequency response is discontinuous

$$H(f) = \begin{cases} 0, & f=0 \\ 1, & 0 < f < f_s/2 \\ 0, & f=f_s/2, \end{cases} \quad (33)$$

and this is difficult to approximate using a finite impulse response. A 31 point Hilbert transformer was designed using the same optimization program as for the bandpass filter, and the results are shown in Figure 27. Although this filter is half as long as the bandpass filter, the maximum magnitude error is only 1.4 percent between $.35 f_s$ and $.465 f_s$. Another useful characteristic is that half of the filter coefficients are zero for a transformer which is symmetric in the frequency domain about $.25 f_s$, hence the net filter length is only 15.

Care must also be taken when convolving the filter weights with the sampled data, as a portion of the time series is needed to start the filters and is lost in the filtering process. Consider the fictitious time series of Figure 28(a) and the seven point filter of Figure 28(b). Since the time series is finite in length, it represents a signal which has been multiplied by a boxcar function. It is not valid to assume that the signal has any particular

value before the zeroth sample, hence it is impossible to apply the filter to get an output value for the zeroth sample. For a symmetric filter of length M_f where M_f is odd, the first $(M_f-1)/2$ values of the time series are lost. In a similar matter, Figures 28(d) and 28(e) demonstrate that for a Hilbert transformer of length M_h , where M_h is odd, $(M_h-1)/2$ values are also lost. A similar loss of data occurs at the end of a time series.

For the decimated data of Run 1A, the sampling rate corresponds to about 9.25 samples per Strouhal cycle, therefore about ten cycles of data are lost in filter startup and shutdown. By implementing a continuous acquisition routine, 200 Strouhal cycles of data were acquired in a continuous segment, so the filter startup and shutdown was required only once for every complete set of data.

A typical decimated and bandpass filtered time series obtained from actual data is shown in Figure 29(a), and the imaginary signal obtained through the Hilbert transform in Figure 29(b). Using the relations given in Chapter II, the instantaneous phase obtained is shown in Figure 29(c). Due to the decimation, the phase is known only for every eighth temperature sample. Since the changes in phase are nearly linear between computed samples linear interpolation was used to recover the phase between the calculated values.

Conditional Analysis of Wake Temperature

Using the previously mentioned techniques, the raw

data was converted into a useable form by the IIT UNIVAC 1108 computer. For each temperature probe position, the instantaneous phase and amplitude of the phasing signal were calculated and the temperature data was sorted according to channel. The resulting data was written on tape in a format compatible with the PDP 11/10 computer, and the DAPS was used for all further processing of the data.

This mixed processing technique was chosen for a variety of reasons. Although the UNIVAC is much faster than the PDP for many computations, the most time consuming aspect of the temperature data analysis is the transfer of data between magnetic tape and memory. Because the UNIVAC is a time sharing machine, the actual wall time duration for a typical run is about the same as for the PDP. The calculations of the probability density analysis are simple in form, but must be performed many times in succession. PDP assembly language is well suited to this type of computation.

The conditional probability analysis is performed by simply placing a range on amplitude and phase, and then computing the number density of the sampled temperature when both phase and amplitude are within range. Since amplitude conditioning was not used in the current study, it will not be mentioned further.

Consider Figure 30 which is a plot of the computed phase angle together with the six simultaneous temperature signals. A phase window of $\pi/16$ (represented by the dashed

lines) was chosen after comparison of several windows; a larger window will smear the phase conditioned statistics, whereas a smaller window will pass insufficient data to permit convergence of the statistics. The pairs of arrows in Figure 30 denote the time intervals over which the conditional sampling occurs.

The UNIVAC was used to compute instantaneous phase and amplitude of the phasing signal and this information along with the instantaneous temperature data was written on magnetic tape for further processing on the PDP. The records on this tape are small enough to fit PDP memory with room for appropriate software, and the conditional probability density functions are computed directly from this data. These functions can either be plotted directly, or integrated between temperature limits to yield $P(\theta_1 < \theta \leq \theta_2 | \phi')$ (see equation (31), Chapter II). In this case the resulting probabilities are punched on paper tape, and these tapes are read by BASIC routines (BASIC is a language similar to FORTRAN which is implemented on the PDP 11/10) and plotted as a function of x and y . The resulting plots can be saved using the hard copy unit.

Error Analysis

This brief discussion is provided to give some indication of the errors expected in the various phases of the data processing. It should be emphasized that the concepts presented here are by no means rigorous, and they are only meant to give order of magnitude numbers.

For spectral estimates, Bendat and Piersol [2] give the relative error at any frequency as

$$\epsilon = \frac{1}{\sqrt{B_e/T}} \quad (34)$$

where B_e is the bandwidth for each record in an ensemble of records. As discussed earlier, the record length was reduced by a factor of four, and a Hamming window was applied to the data. The bandwidth can be given by

$$B_e = 2 \frac{k}{T} \quad (35)$$

where k is the number of records in an ensemble. Therefore,

$$\epsilon = \frac{1}{\sqrt{2k}} \quad (36)$$

For the spectral data processed in the present work, k is 80, resulting in a relative error in the spectral estimate of about 8 percent.

The errors present in the bandpass filter and Hilbert transformer have been discussed earlier in this chapter. The errors in the probability density estimate are somewhat more difficult to determine and that will not be done here. However, a smooth curve can be drawn through the probability values computed at different spatial points and this appears to be an adequate demonstration of accurate results.

An experimental error encountered in the temperature

measurements nearly resulted in the loss of an entire channel of wake temperature data. For unknown reasons the channel five bias voltage drifted drastically through the course of the experiment. Fortunately, the time and ambient temperature were recorded periodically, and the temperature sensors were placed in the free stream at intervals throughout the experiment. A plot of the apparent ambient temperature (due to drift) was constructed using this data, and a curve fit through these points was used to determine the drift as a function of time (see Fig. 31). The raw temperature data was compensated based on this drift function, and the resulting probabilities appeared to converge correctly based on data from nearby points.

CHAPTER V

RESULTS AND DISCUSSION

Power spectra and coherence functions are used to yield some insight into the dynamics of wind tunnel operation. Early results of wake measurements are presented, and this leads to a more detailed investigation of the wake. A phase-conditioned statistical analysis of the wake is performed, and this leads to several conclusions pertaining to wake dynamics.

Wind Tunnel Diagnostics

As discussed previously, the fluctuations in the wind tunnel free-stream velocity lead to questions pertaining to the causes and effects of these fluctuations. Although it is easily verified that the wind tunnel velocity is uniform in the time average, this provides little insight into the dynamics of the wind tunnel operation. The results of diagnostic measurements at the extremes of the operating range will be discussed here.

The room pressure versus free stream velocity diagnostic measurements are summarized in Figures 32 and 33. In order to demonstrate the stationarity of the data, the U_{∞} spectra were calculated from two independent sources of data, the second being the phasing velocity, U_{ϕ} versus U_{∞} velocity diagnostics (Figs. 34 and 35). These measurements were conducted approximately one hour apart, yet both measurements produce the same U_{∞} spectra (within an

acceptable error) for each of the velocities tested. It is felt that the assumption of stationary data is justified.

The room pressure for $U_{\infty} = 4$ ft per second exhibits three distinct regions in the power spectrum: a low frequency region between 1 and 5 hz, a small peak between 7.5 and 10 hz, and a larger peak centered about 13 hz. The free stream velocity spectrum has similar trends, with a more pronounced peak between 7.5 and 10 hz. All three peaks are present in the coherence estimate, indicating a linear relationship between P_r and U_{∞} particularly in the low and middle frequency bands, but the peak near 13 hz does not seem large enough to be significant.

At 21.5 ft. per second the P_r spectrum is rich in frequency content, and this is readily apparent to the experimenter as a rather noisy wind tunnel room. The U_{∞} spectrum contains three peaks at the low frequency end of the spectrum and a distinct peak in the vicinity of 60 hz. The coherence function shows some relationship at low frequencies, with rather distinct peaks near 20 hz and 60 hz. The advantage of computing coherence is apparent when these peaks are compared with the seemingly wide band pressure spectrum. Although there are no outstanding peaks in the P_r spectrum near either 20 or 60 hz it is clear that there is a relationship between P_r and U_{∞} at these frequencies. The coherence at 60hz can be explained by the

ever present line noise. The causes of the other coherence peaks in this and the 4 ft/sec measurements require further consideration. If one considers the length of the wind tunnel, 48.5 ft, the circumference of the entire tunnel, 123 ft, and the speed of sound, 1135 ft/sec, this results in possible longitudinal standing wave frequencies of 23 hz and 9 hz. Hence standing waves would appear to be a reasonable explanation for all but the velocity fluctuations below 5 hz, and this again leads to the possibility of a Helmholtz instability, although there is no present evidence to verify this.

The U_∞ spectrum of Figure 34 exhibits spectral peaks at both the first and second harmonic of the 5 hz Strouhal frequency. It is interesting to note that there is coherence at the Strouhal frequency with the freestream velocity sensor which is upstream of and above the actual cylinder, a position which would usually be considered out of the influence of the cylinder. The other coherence peak would not seem to be due to the higher harmonic of the Strouhal frequency but instead due to the free stream velocity fluctuations near 10 hz.

The U_∞ spectrum of Figure 35 at 21.5 ft/sec again exhibits a relatively large peak at the Strouhal frequency. The peak at the extreme low frequency end of the spectra and coherence function is due to d.c. components in the signals. The coherence function shows that there is virtually no linear relationship between U_∞ and U_ϕ except

at the Strouhal frequency.

Based on these results, there is little reason to believe that there is a significant connection between low frequency (below the Strouhal frequency) free stream velocity fluctuations and the low frequency content in the phasing signal. Also, the velocity fluctuations in the free stream might be divided into two categories: fluctuations possibly due to longitudinal standing waves in the wind tunnel and lower frequency fluctuations of unknown origin.

Wake Measurements

As discussed in earlier chapters, the thermal tracer was detected in the cylinder near wake, and conditioned statistics were calculated to permit a better understanding of the wake processes. As long as the flowfield is two dimensional, the vorticity transport equation has exactly the same form as the two dimensional heat transfer equation. Thus, for a fluid of Prandtl number near unity, the transfer of heat from the surface of the cylinder should be a process which is analogous to the transfer of vorticity. In other words, the momentum boundary layer and the thermal boundary layer should be of the same order of thickness. A simultaneous measurement of the mean thermal and momentum boundary layers was made for $Re \approx 4000$, and the results are shown in Figure 36. A dual sensor probe was constructed with the temperature and velocity sensing wires located at the same x and y coordinate, and offset in the z direction, along the axis

of the cylinder. The sensors were driven by temperature and velocity circuits similar to those previously discussed, and the output voltages were averaged with an analog voltmeter. The results of Figure 36 verify that the thermal and momentum boundary layers are indeed nearly the same thickness. Note also that the greatest temperature above ambient is only 2.5°C , which results in negligible buoyancy.

The phasing velocity was detected using the hot-wire sensor located outside of the boundary layer near the separation point. This position provides a signal which is indicative of the shedding process with low spectral content at frequencies outside of the Strouhal peak. For early measurements, the phasing hot wire was actually immersed in the boundary layer, as the steep gradients in the velocity profile would amplify any fluctuations in the boundary layer resulting in the large velocity fluctuations sensed by the hot wire. But the nonlinearity of the velocity profile distorted the almost sinusoidal velocity fluctuations, resulting in a signal rich in spectral content beyond the Strouhal peak. For sensor positions outside of the boundary layer, the harmonics were reduced considerably, but so was the amplitude of the phasing velocity fluctuations. Suitable analog amplification alleviated this problem.

Early attempts to use the phasing signal for conditional sampling of the wake involved the computation of cross

correlation functions. The phasing velocity was correlated with the temperature fluctuations sensed by a single temperature sensor in the cylinder wake using a PAR 100A Signal Correlator. The output of the correlator was averaged using a PAR TDH-9 Waveform Eductor and the resulting correlation function was plotted on an x-y plotter. The correlation functions can in general be described as a sinusoid which decays slowly with increasing time delay (the independent variable in the correlation function) and which possesses some relative phase shift ϕ_c . This phase shift corresponds to the difference in phase between the periodic phasing velocity and the periodic temperature fluctuations at a particular location in the wake. The values of ϕ_c were calculated for various downstream temperature sensor positions along the centerline of the wake at four different Reynolds numbers, and the results are plotted in Figure 37. Note that there is a sharp change in slope exhibited by each of the ϕ_c curves at some value of x/D , and that this x/D value decreases with increasing Re . The horizontal portion of each curve can be explained as a forming Kármán vortex, which remains relatively stationary in the wake as vorticity is fed into it. After this growing process, the mature vortex is rapid accelerated and convected downstream. This acceleration is evidenced by the increasing rate of change of x/D with ϕ_c , where ϕ_c is actually a time delay normalized with the Strouhal period. Hence the

sharp bend in the ϕ_c curve should be an indication of the downstream position at which the Kármán vortices form.

As a consequence of these results, a more detailed investigation of the wake was undertaken. The early results provide information only along the centerline of the wake, and the interpretation of the curves tends to be very subjective.

The phase conditioned statistical technique described in previous chapters was chosen as the most promising technique for interpreting the temperature data from the wake. Although data was sampled and recorded on digital tape for three Reynolds numbers, only the results for $Re=7600$ will be presented here. Statistics conditioned on phase alone will be considered, but the possibility of further conditioning of the statistics will be discussed in Chapter VI.

The phasing velocity signal was processed using the bandpass - Hilbert transform technique presented earlier, producing a complex rotating vector which shows the instantaneous amplitude, phase and frequency characteristics of the shedding process. The center plot of Figure 38 contains both the real and imaginary parts of this complex vector, superimposed to better show their relationship. Note that $z^i(t)$ is not merely $z(t)$ delayed by $1/4$ of a mean period; instead it is the signal which is the sum of the spectral components of $z(t)$, each delayed by $1/4$ of its own period.

The instantaneous amplitude, $A(t)$ and the instantaneous angular frequency, $\omega(t)$ were calculated from this complex function, and are also presented in Figure 38. The frequency was calculated by applying a nine point digital differentiator to the computed phase. The amplitude function corresponds to the envelope of $z(t)$ but the Hilbert transform permits its definition for all values of time. The first few periods of the results shown in Figure 38 are expanded in Figure 29. In Figure 29, the large amplitude modulation (about 50 percent) is not obvious, but it can be seen in Figure 38 that there is a large modulation with a period corresponding to about 4 to 8 shedding periods. Furthermore, the computed phase in Figure 29, shows what seems to be a constant phase when there is an approximately 10 percent frequency modulation. The frequency modulation is not present as a result of the bandlimiting process, however, because the bandwidth of the filter allows up to 60 percent modulation about the center frequency. Furthermore, the amplitude modulation does not appear to contain frequencies greater than about one-fourth the center frequency of the filter, and this filter allows amplitude modulation frequencies up to one-half the center frequency. Therefore, it can be said with total confidence that the results of the processing technique are not caused by the digital processing, but instead are a decoding of the information actually contained in the signal being processed.

If a simple visual comparison is made between $A(t)$ and $\omega(t)$ in Figure 38, there seems to be an anticorrelation between the fluctuations of these functions. Gerrard [10] concluded that amplitude and period are inversely related on the basis of observation of oscilloscope traces, and this implies exactly the opposite of the present results. Certainly further investigation of the $A(t)$ and $\omega(t)$ functions is warranted, and this should be considered in further work.

The computed phase was used to conditionally sample the wake temperature data as discussed in Chapter IV. The conditional probability density functions (see Equation (31), Chapter II) were computed at each sensor position, and then integrated above a minimum temperature θ_1 to yield the phase conditioned probability that the temperature would exceed the minimum value. Based on the probability distribution of the thermal tracer in the wake, insight into the wake processes can be gained. However, the determination of a suitable value for θ_1 must first be established.

Thermal tracers have been used previously to distinguish vortical fluid from the outer potential flow (see Fabris [9], LaRue and Libby [16]). However, the experiments of these researchers were carried out far downstream in the wake where the tracer is well mixed within the turbulent fluid. The determination of a temperature threshold was simply a problem of making θ_1 as close

to zero as possible without detecting the noise in the temperature signal. For this experiment the determination of θ_1 is not that simple. In the near wake there is vortical fluid with differing degrees of mixedness. If θ_1 were set just above the noise level of the signal, any fluid bearing vorticity from the tagged shear layer would be detected. On the other hand, a high value of θ_1 would permit the detection of only the least diffused vorticity. Hence the question of determination of θ_1 becomes relative, based on the concentration of the thermal tracer.

The first set of probability plots involves holding phase constant while computing the conditional probabilities for a series of θ_1 values. The results for θ_1 equal to .154, .292, .451, and .610°C respectively are shown in Figure 39. These are psuedo three-dimensional plots, with the horizontal axis corresponding to both the x direction and probability.

In comparing these plots, several interesting trends can be observed. Consider first the plot for the highest threshold value. Near to the cylinder, the probability curves are very steep and very sharp. Hence, the shear layer position seems to repeat itself very regularly between periods. At $x/D=1.5$ the phase mean width of the probability plot begins to widen and the peak begins to decrease in height, and this trend continues as downstream distance increases. This spreading can be attributed to the presence of transition waves in the separated shear

layer, and the nonlinear growth of these instabilities results in increased randomness and tracer diffusion with downstream distance.

When θ_1 is lowered to $.451^\circ\text{C}$, the area in which the tracer is found increases, and this trend continues for $\theta_1 = .292^\circ\text{C}$. In the latter case, the vertical traverse at $x/D = 1.25$ seems to indicate the shear layer in two places, which would be indicative of the forming Kármán vortex. When θ_1 is lowered to $.154^\circ\text{C}$, the thermal tag seems to be detected almost everywhere in the wake. Comparing this with the other plots, it seems that the forming vortex which rolls up some distance downstream of the cylinder may be ejecting vortical fluid into the region immediately behind the cylinder in the formation process. This would be consistent with Gerrard's explanation of the wake processes, where the volume of the formation region is created by a balance between the fluid entrained in the separated shear layer and the fluid ejected into this region during the vortex formation process.

It is interesting to note that the lowest threshold shows the presence of the thermal tag all across the wake, and even down to the opposing shear layer. Hence the region immediately behind the cylinder appears to be a well mixed region containing vorticity from both boundary layers across the entire width of the wake. This demonstrates a direct transport of fluid across the wake in the near wake region.

The data at an x/D of .5 is simultaneously plotted on a larger scale in Figure 40 for all four threshold values. The boundary between the shear layer and the outer potential flow can be seen to have a sharp temperature gradient which is not smeared by the phase-mean averaging process. On the inner boundary of the layer, the temperature distribution seems to be smeared in a random fashion, and the phase mean temperature gradient is not as sharp as the outer edge. This seems to be a result of the turbulent fluid existing immediately behind the cylinder from the ejection process just described. Random disturbances of the shear layer by this vortical fluid would result in the smearing of the shear layer in the phase mean, and it may be these disturbances which trigger the ensuing instability in the shear layer. Essentially this could imply a feedback process, where the separated shear layer instability is triggered by turbulent fluid from previous Kármán vortices, themselves being formed from the shear layers. The low frequency modulation of the wake might even be an oscillatory instability in this feedback loop. If the near wake is relatively quiescent, the separated layer will remain stable longer, hence less diffused. This sharper shear layer would result in more concentrated vorticity in the Kármán vortex, and greater ejection into the near wake region. The greater ejection would drive the shear layer unstable sooner, resulting in weaker Kármán vortices, and a more quiescent near wake, This would

complete a cycle which lasts an order of a few Strouhal cycles. It should be noted that experimental evidence indicates that the period of the low frequency amplitude modulation is in fact about four to eight cycles in duration.

The results of Figure 39 prompted the calculation of the wake temperature conditional probability profiles for a series of phase angles using the highest value for θ_1 . The high threshold value seems to emphasize the vortex formation process, while the lower thresholds tend to smear the wake characteristics. The most concentrated vorticity should be the primary agent in the formation of the Kármán vortex, therefore the highest temperature threshold would yield the most information about the vortex formation process.

The conditional probability maps for $\theta_1 = .610$ °C are plotted in Figures 41 and 42 for eight values of phase. Close to the cylinder, the shear layer can be distinctly identified throughout all the phases, and it does not seem to change significantly throughout the Strouhal cycle. However, as downstream distance is increased, the wake characteristics seem to show distinct changes throughout the shedding cycle. Beginning at phase zero, the Kármán vortex appears to be accelerated and convected in the downstream direction, resulting in an increasingly long shear layer. At a relative phase of about $3\pi/4$, the shear layer begins to be drawn across the wake. The

subsequent diffusion of the shear layer downstream of the point at which a new vortex is beginning to form results in an effective cutoff of vorticity to the previously formed vortex. By $\phi = 5\pi/4$, the old vortex has been shed, and the new vortex proceeds to roll up for the remainder of the cycle. The formation process seems to occur primarily at a single downstream position, and when the vortex is completely formed, it is subsequently accelerated and shed. This seems to verify the conclusions drawn from the correlation results.

A less detailed plot of the formation process is presented in Figure 43. The shaded regions correspond to the envelope of the plots of the previous two figures. In other words, the plot of Figure 43 shows the regions where there is a nonzero probability of finding temperatures greater than the threshold. If nonzero probability is termed possibility, then these are the regions where it is possible to find the tracer at a particular phase for at least one percent of the Strouhal periods considered. The lower shear layer for each of the phases ϕ is simply a duplicate of the upper layer at phase $\phi + \pi$ flipped about the wake centerline. This should correspond to the lower shear layer position because of the antisymmetry of the process.

Considering only the upper shear layers, the layer seems to be the first drawn into the wake at a ϕ of $3\pi/4$. Subsequently the Kármán vortex is formed, and at a phase of

about $7\pi/4$, the acceleration of the stationary vortex begins. The initiation of a new vortex begins almost simultaneously with the acceleration of the previous vortex which is forming from the opposite shear layer. Phases 0 through π demonstrate the acceleration process. It should be noted that the results of the correlation technique used for the preliminary results predicts the position of the accelerating vortex almost exactly, when the results of both techniques are compared. Therefore the correlation technique appears to be an adequate method for determining the downstream distance at which the Kármán vortices form.

Figure 44 is an enlarged plot of the vertical traverse taken at an x/D of .75 for half of the phases plotted in Figures 41 and 42. This figure is provided to indicate the periodic oscillation of the position of the separated shear layer. For any particular phase, the probability of finding fluid with a temperature greater than the threshold value appears to be a Gaussian function of vertical position. This dispersion of shear layer position is most likely due to the presence of Bloor instabilities in the shear layer. If the phase mean position of the layer is considered, a very definite transverse periodic motion of the separated layer can be observed. The shape of the curve seems to be preserved throughout the cycle, and this indirectly demonstrates that the present technique computes phase accurately. Consider the $\phi = 0$ and the $\phi = \pi/2$ curves in Figure 44. If there were smearing across phase,

the $\phi = 0$ curve would be expected to spread in both vertical directions, as the shear layer mean position is lower for $\phi < 0$ and higher for $\phi > 0$. However, if the shear layer is at the extreme of its periodic swing, as for $\phi = \pi/2$, higher and lower phases both have lower mean shear layer positions, therefore smearing in phase would result in a skew probability curve at this extreme position. Since the curves have almost identical shapes, there apparently is negligible smearing in phase. The same argument holds at the other extreme shear layer position for $\phi = 3\pi/2$.

Based on the results shown in Figure 44 it might be tempting to define a mean instantaneous shear layer thickness in terms of the half-widths of the curves. However at the present time, because the temperature threshold is arbitrary, it would be premature to reach any conclusions about the shear layer thickness. Further investigation is warranted, especially with respect to the temperature gradients on either side of the shear layer.

CHAPTER VI

CONCLUSIONS AND RECOMMENDATIONS

The conclusions of this series of experiments fall within three primary categories. The first includes experimental apparatus and diagnostic measurements related to experimental facilities. The second category involves the data processing techniques used in treating narrow band polychromatic processes. The third and last set of conclusions relates to the conditional temperature measurements made in the wake of the cylinder, and associated conclusions about near wake processes. Based on these conclusions, a series of recommendations for further work are made.

Conclusions

A set of diagnostic experiments and calculations related to instrumentation and facilities leads to the following conclusions.

1. A cylinder model with a thin film surface heating strip can successfully be used to selectively inject a thermal tracer into the flowfield in the near vicinity of the cylinder. In order to localize the surface heating, a water coolant at ambient wind tunnel temperature must be pumped through the center of the cylinder model. The surface heater can then be used to thermally tag the vorticity in a single boundary layer of the cylinder.
2. The thermal tag can be detected in the wake of

the cylinder using a multiple sensor resistance thermometer. A carefully designed probe results in negligible interference with the wake flowfield, and permits the use of a very small sensor with a frequency response of order 1-2 kHz. By double shielding the probe leads, a low sensor current of 88 μ A can be used and this results in negligible velocity sensitivity with a noise level equivalent to .01 $^{\circ}$ C RMS. A set of six broken bridge circuits can be used to compensate for changes in ambient wind tunnel temperature.

3. Wind tunnel sidewall boundary layer influence on the cylinder flowfield can be reduced significantly through the use of specially designed end plates. These plates incorporate a circumferential ring to reduce cross-flow on the front of the cylinder, and a large plate in the wake region to eliminate communication between the cylinder wake and wind tunnel sidewall boundary layer. Consequently, a finite length cylinder can be used to approximate the flowfield in the vicinity of a two dimensional model.

4. A hot wire sensor placed in the potential flow region outside of the boundary layer near the separation point can be used to generate a signal characteristic of the eddy shedding process. The velocity fluctuations at a frequency near the Strouhal frequency appear to be induced by the Karman vortices, and fall within a well defined spectral peak superimposed on a random background spectrum.

5. Frequency domain statistics relating wind tunnel

free stream velocity and room pressure for the extreme velocities of interest demonstrate a linear relationship between velocity and pressure fluctuations at several frequencies. Significant correlation exists in three frequency bands centered about 3 hz, 9hz, and 23 hz. The higher frequencies might be explained by standing waves corresponding to the length of a single tunnel leg and the circumferential centerline distance. The low frequency fluctuations might be attributed to a Helmholtz instability between the room and wind tunnel.

6. Frequency domain statistics relating the wind tunnel free stream velocity with the velocity fluctuations sensed by the phase reference velocity sensor demonstrate that there is no significant relationship between the two velocities outside of the Strouhal frequency. The low frequency fluctuations in the vicinity of the cylinder do not appear to be related to the free stream velocity. Free-stream velocity fluctuations sensed six diameters upstream and six diameters above the cylinder wake are felt even at a position usually considered out of the region of influence of the cylinder wake.

The following conclusions can be made concerning the technique used for processing the phase reference signal.

1. The peak of finite bandwidth appearing in the spectrum of the phasing velocity can be separated from the random background spectral content using a finite

impulse response digital filter. This filter does not cause undesirable phase shifts in the signal and produces a bandlimited polychromatic signal which is characteristic of the eddy shedding phenomenon.

2. This signal can be processed using a complex representation of a real polychromatic function to yield instantaneous phase as well as instantaneous amplitude and frequency modulation. This processing technique involves the implementation of a discrete Hilbert transformer to determine the imaginary part of the complex function. As a result, the exact instantaneous phase of the eddy shedding process can be computed without the limiting assumptions of previous workers, and phase conditioned wake statistics can be determined.

3. The wake appears to have frequency and amplitude modulations which are roughly anti-correlated. The amplitude modulation appears to be about fifty percent with a characteristic period of four to eight Strouhal cycles. The frequency modulation is approximately ten percent with a characteristic frequency in the vicinity of four Strouhal cycles.

The wake temperature measurements lead to several conclusions for $Re=7600$.

1. The mean thermal and momentum boundary layers are of the same order of thickness near the separation point of the cylinder. If the thermal tag is injected into a single boundary layer, it provides an indication

of the vorticity throughout the wake coming from that boundary layer.

2. The shear layer appears to be very well defined near the cylinder. Although there is a periodic transverse motion of the shear layer at the Strouhal frequency, the layer duplicates its position almost exactly from cycle to cycle.

3. At a further downstream distance, the phase-mean position of the shear layer is smeared by the appearance of transition waves. However, the periodic transverse oscillation is still evident.

4. The near wake region which is bounded by the cylinder, the separated shear layers, and the forming Kármán vortices appears to contain turbulent vortical fluid which is ejected into this region during the vortex formation process.

5. The free shear layer appears to have a sharp vorticity gradient at the boundary with the outer potential flow but the boundary with the near wake region is more diffuse as a result of interaction with the vorticity in the near wake.

6. The vorticity in the near wake may have a significant role in driving the shear layer unstable. This would imply a feedback loop between the forming vortex and the shear layer which feeds it vorticity. The low frequency modulation of the wake may be an instability present in this feedback loop.

7. The processing technique used to determine the

instantaneous phase of the eddy shedding process appears to result in little smearing of the statistics across phase.

8. The results obtained using a high temperature threshold level in the wake probability computations indicate the phase mean formation and shedding of a Kármán vortex.

Recommendations

The following is a set of recommendations aimed at guiding future work related to the present experiment.

1. A better understanding of the effect of temperature threshold level should be considered. The introduction of temperature ranges rather than thresholds might aid in this attempt.

2. The conditioning of wake statistics on modulation amplitude as well as phase should lead to a better understanding of wake processes.

3. The feedback mechanism for the low frequency modulation might be investigated through the use of controlled disturbances. If large amplitude sound pressure fluctuations are used to disturb the shear layer in a controlled manner, an override of the feedback process should occur, with subsequent reduction of the modulation.

4. The data already existing on magnetic tape should be processed to yield information on Reynolds number effects.

5. The wind tunnel velocity fluctuations should be considered in greater detail. In particular, the low frequency oscillations (five hz and lower) are not understood very well. In addition the possibility that the cylinder shear layer instabilities are driven by wind tunnel freestream disturbances should be considered.

APPENDIX

Table 1. Wind Tunnel Diagnostic Measurements

Quantity	Run 1	Run 2	Units
Free-stream velocity	4	21.5	ft/sec (fps)
Hot-wire sensitivity			volt/fps
Free stream	50	5	
Near cylinder	5	.25	
Pressure sensitivity	4.05×10^4	4.05×10^4	volt/psi
Sampling frequency, f_s	50	250	hz
Folding frequency, f_o	25	125	hz
Low pass filter cutoff	16	80	hz

Table 2. Data Acquisition Runs

Quantity	Run 1A	Run 2A	Run 3	Units
Re	7600	10600	5800	
Velocity sensitivity	-14.25	-4.55	-16.67	volt/fps
Temperature sensitivity	-3.94	-3.94	-3.94	volts/ $^{\circ}$ C
Sampling frequency, f_s	814	1036	592	hz
Folding frequency, f_o	407	518	296	hz
Samples per position	15300	15300	15300	
Strouhal frequency, f_{St}	≈ 11	≈ 14	≈ 8	hz
Phasing probe position, y/D $x/D=0$.177	.177	.221	

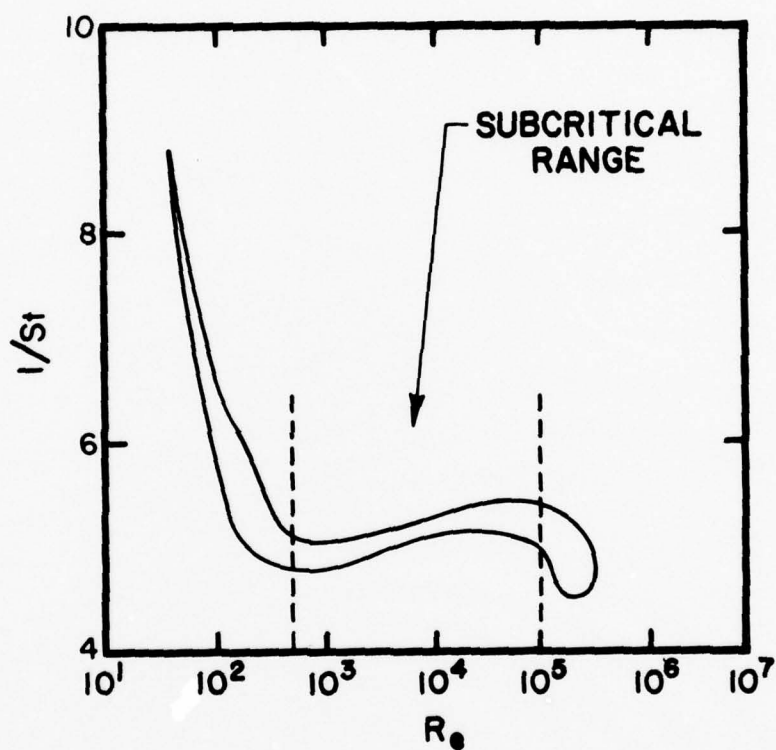


Figure 1. The Inverse of the Strouhal Number as a Function of Reynolds Number for Circular Cylinders

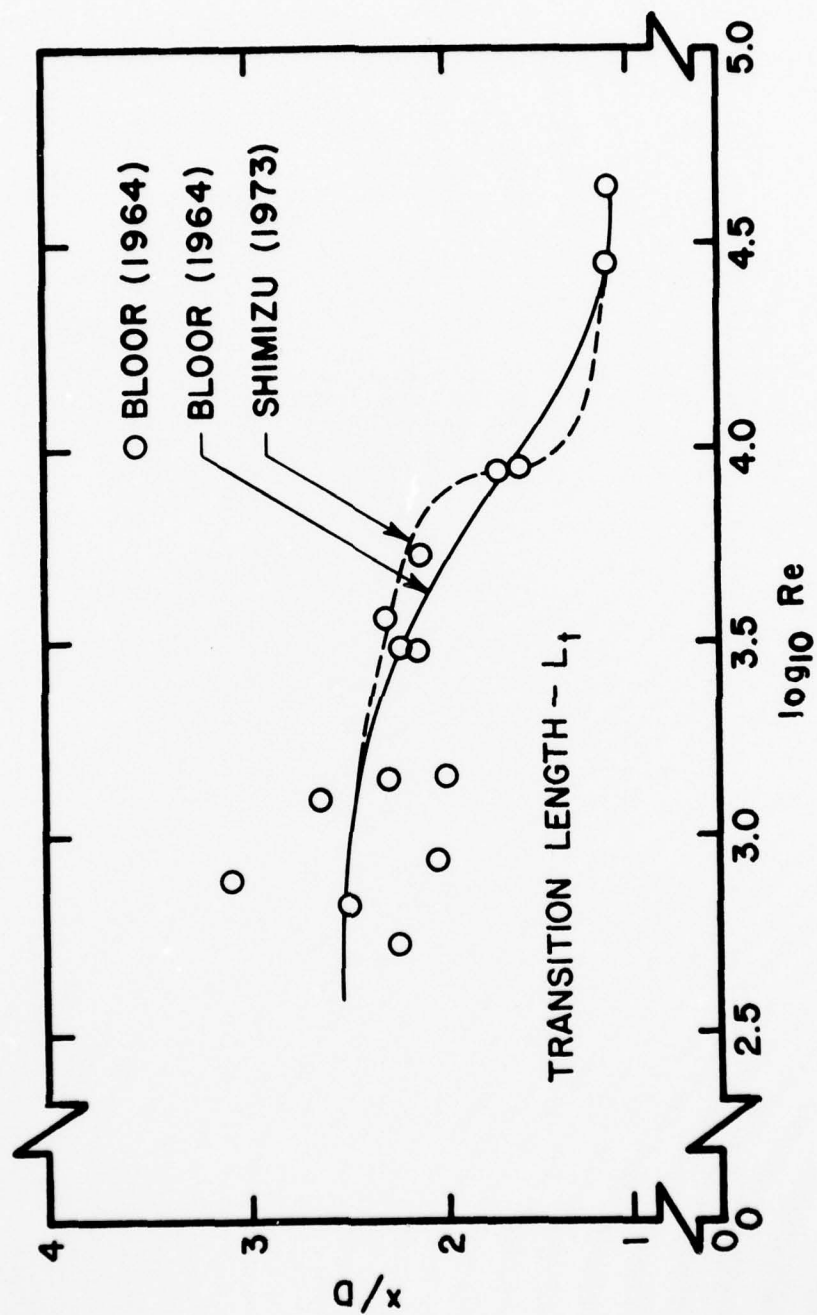


Figure 2. Transition Length, L_t , as a Function of Reynolds Number

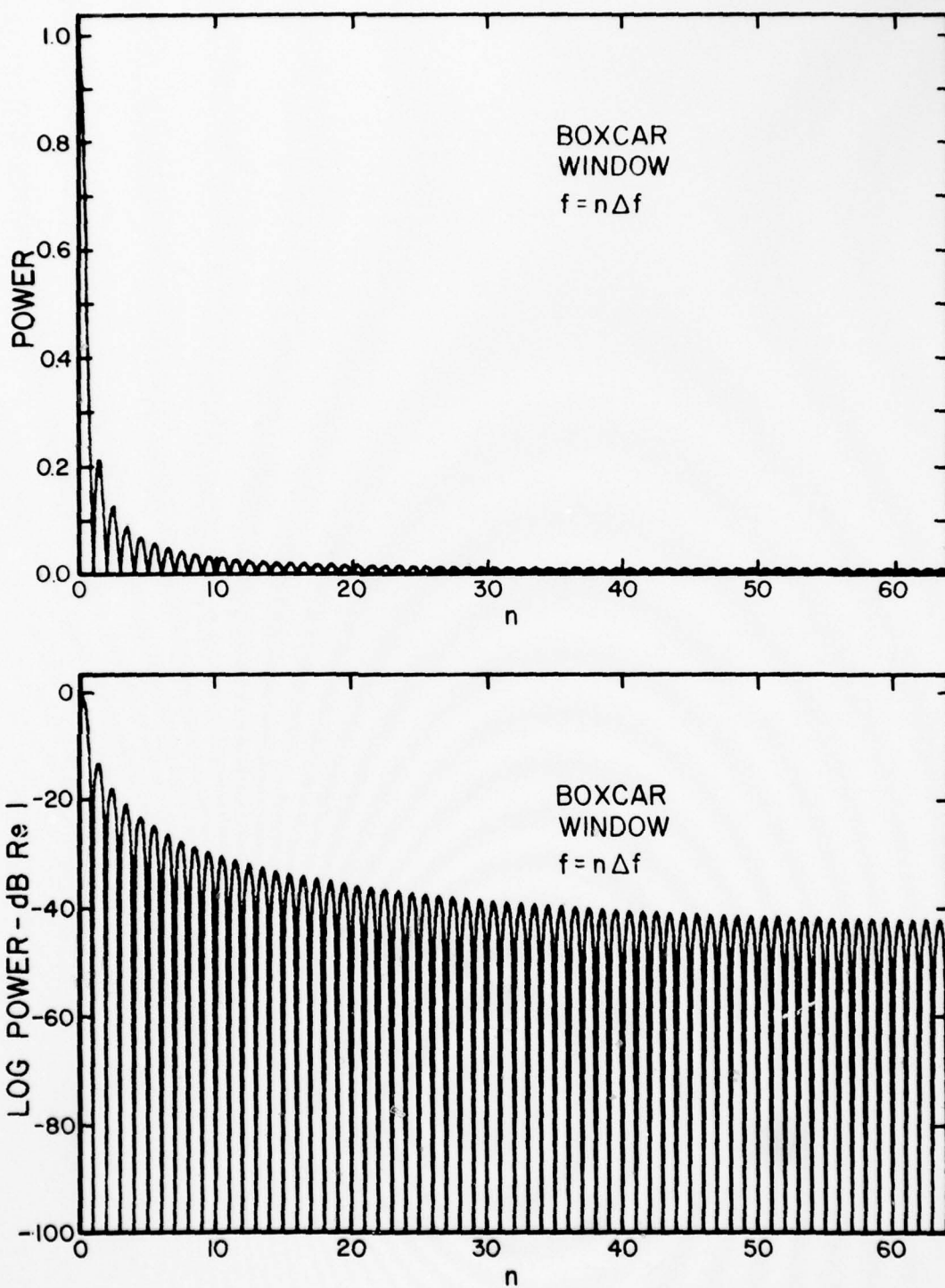


Figure 3. Linear and Log Power Spectrum of Boxcar Window

AD-A059 530

ILLINOIS INST OF TECH CHICAGO DEPT OF MECHANICS MECH--ETC F/G 20/4
AN EXPERIMENTAL INVESTIGATION OF THE NEAR WAKE OF A CIRCULAR CY--ETC(U)
MAY 76 R W WLEZIEN, J L WAY F44620-76-C-0062

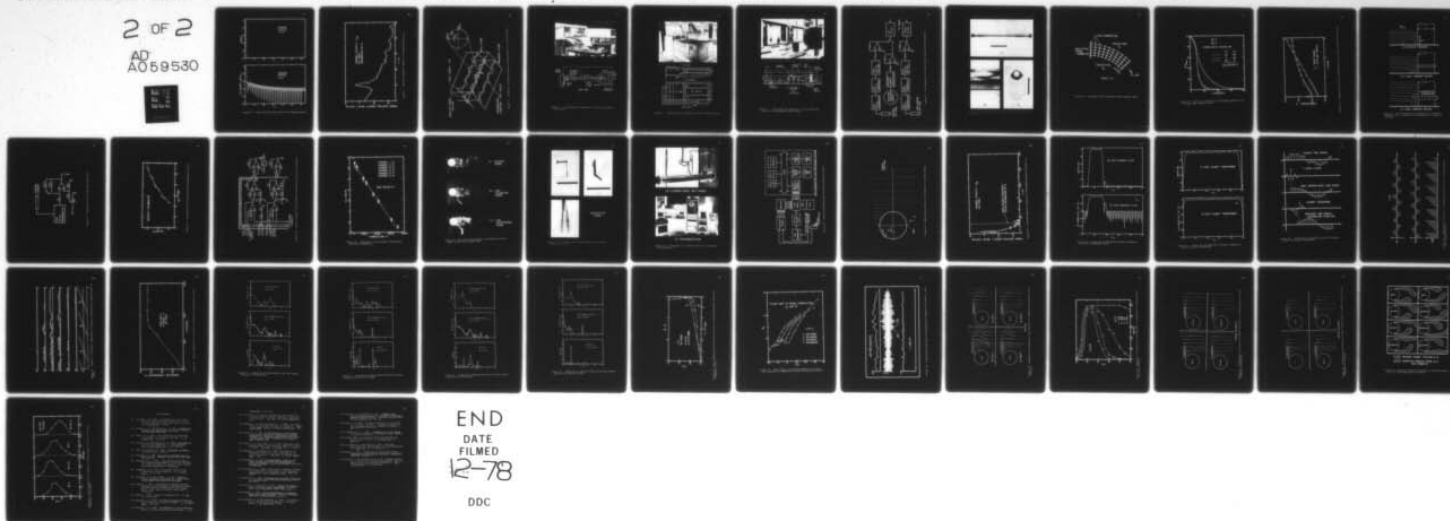
UNCLASSIFIED

IIT-FLUIDS/HEAT TRANS-R76 AFOSR-TR-78-1292

NL

2 OF 2

AD
A059530



END
DATE
FILMED
12-78
DDC

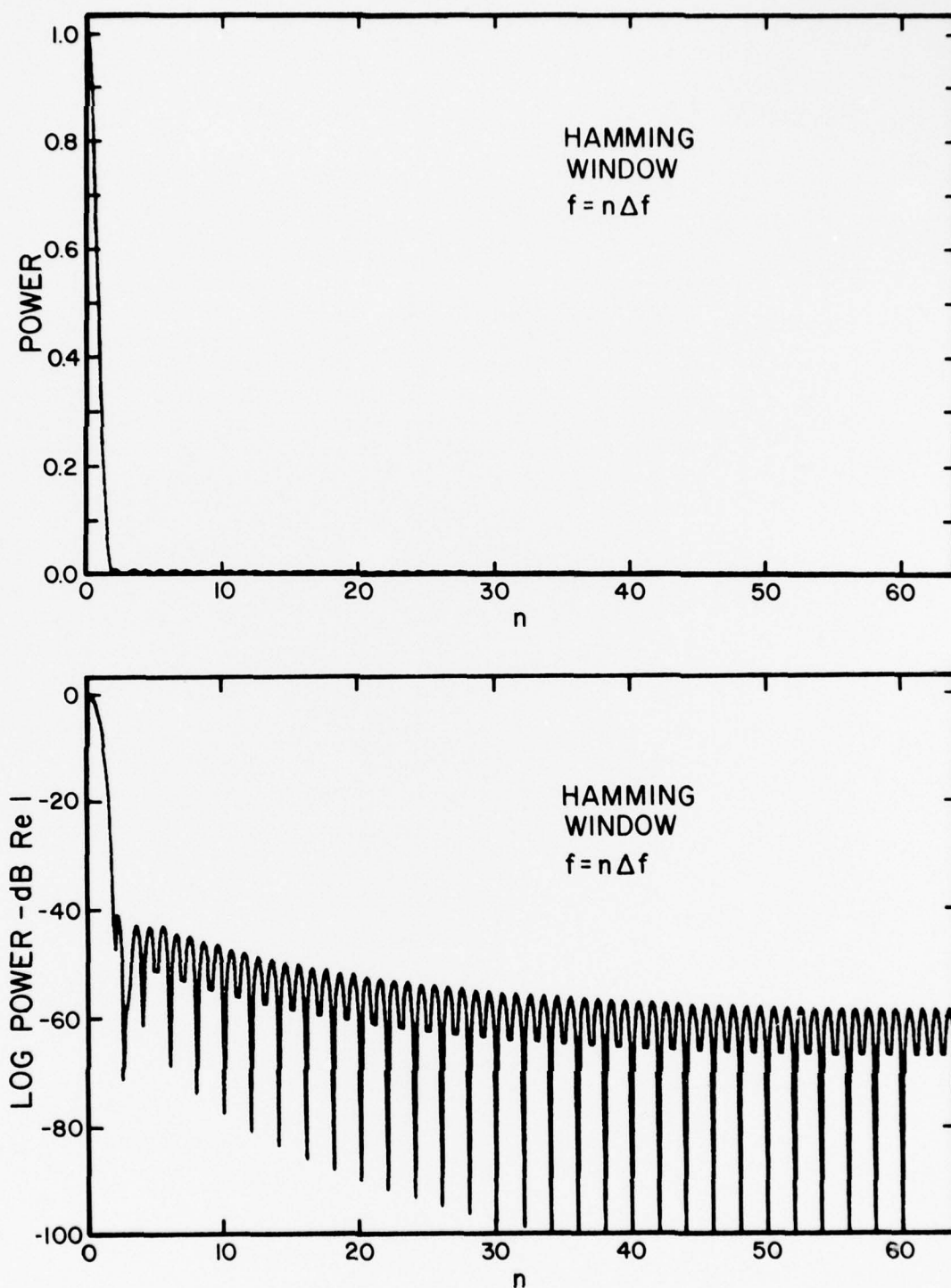


Figure 4. Linear and Log Power Spectrum of Hamming Window

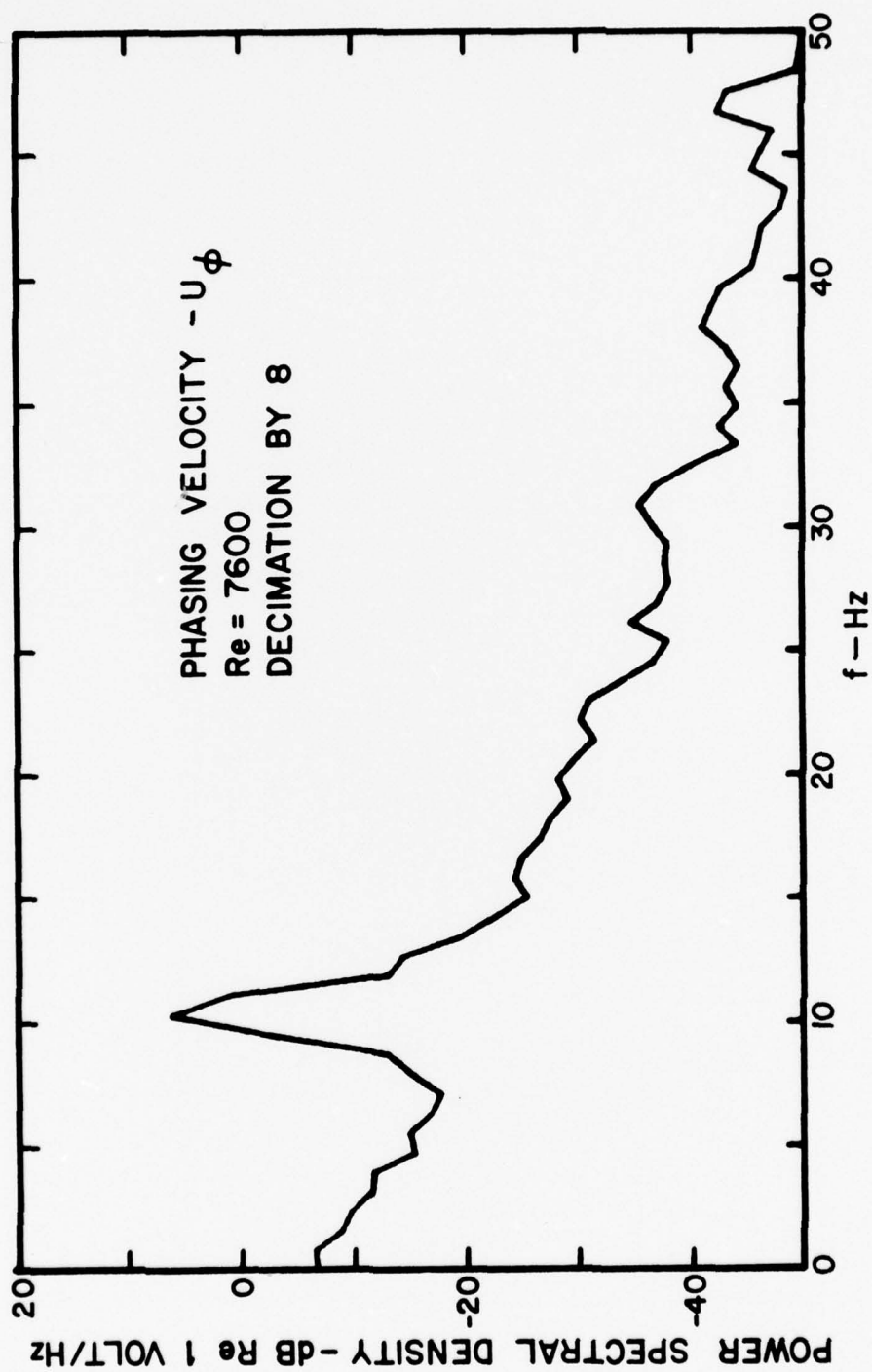


Figure 5. Log Power Spectral Density of Phasing Velocity, U_ϕ

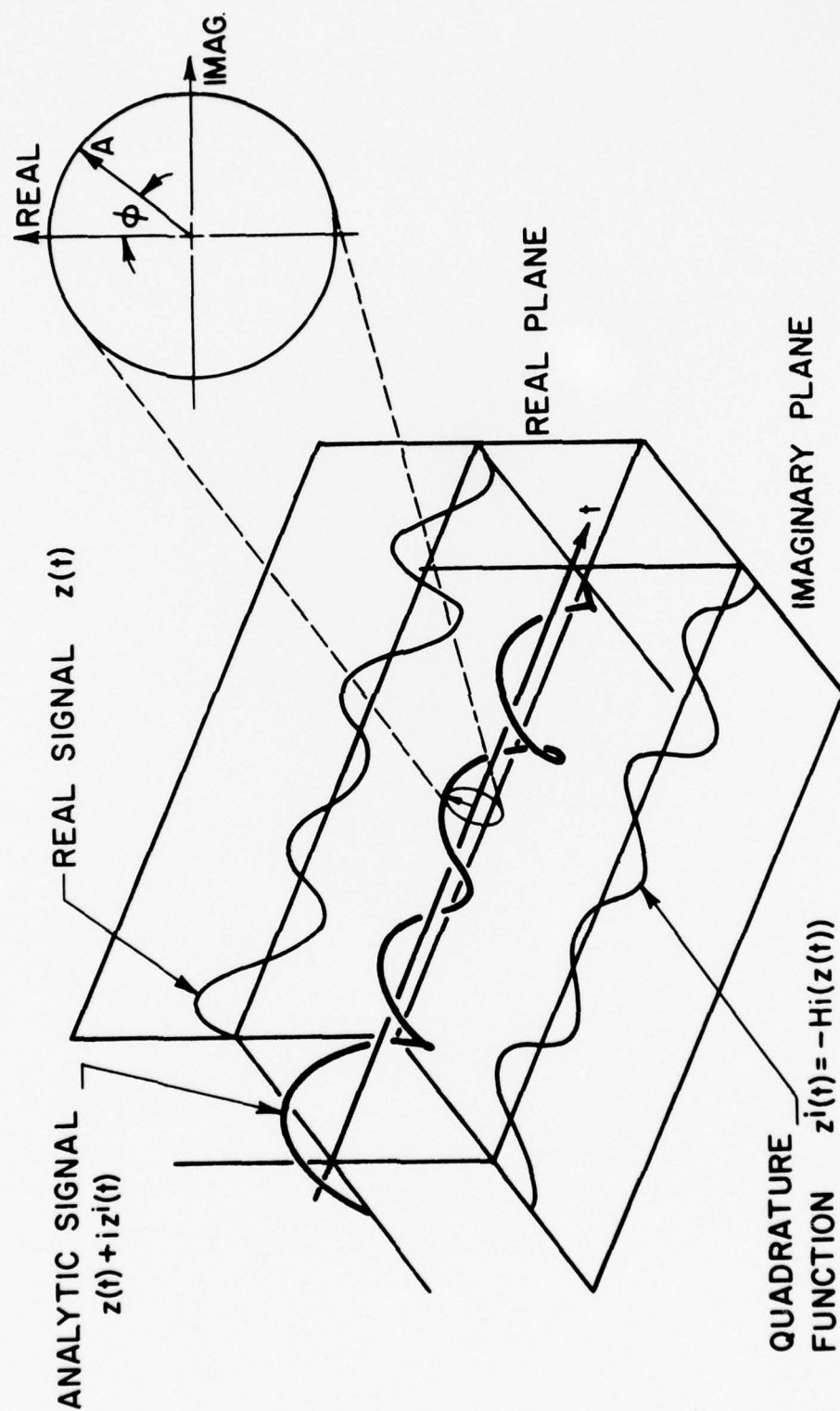


Figure 6. Schematic of Complex Analytic Representation of a Real Function

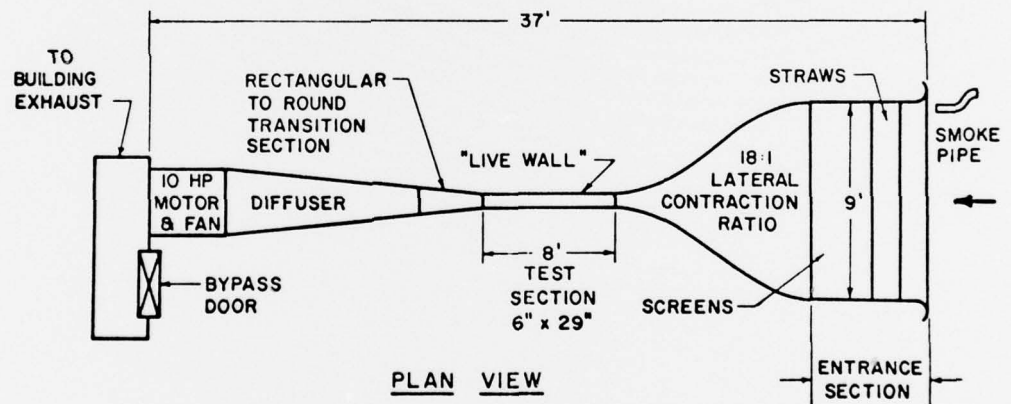
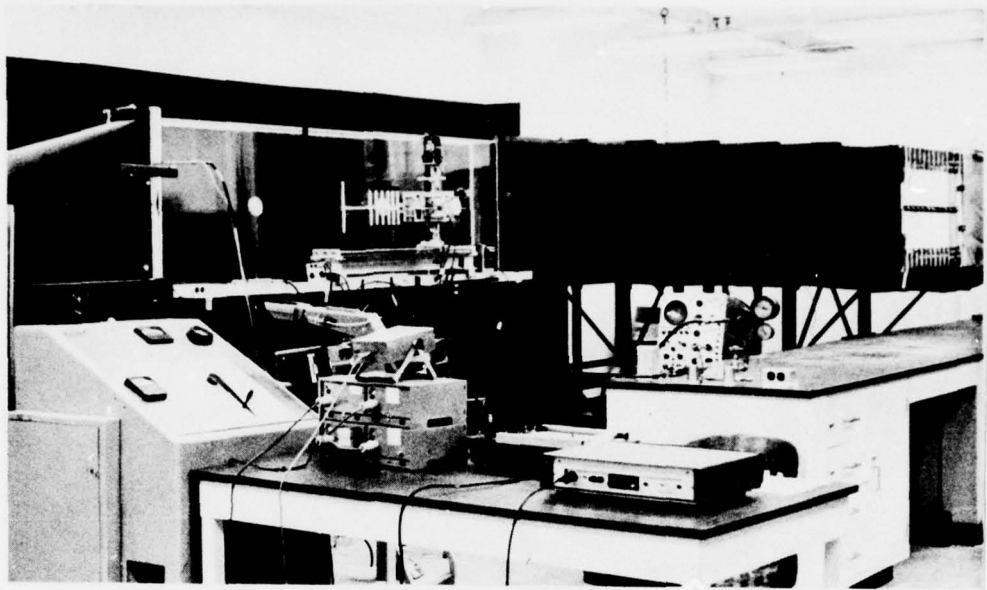


Figure 7. Photograph and Schematic of Flow Visualization Wind Tunnel

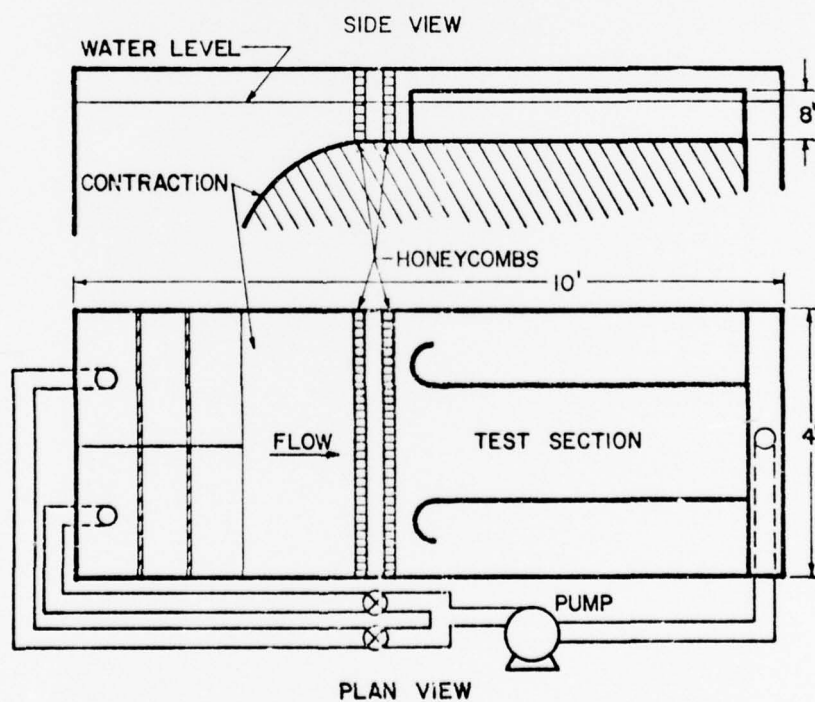
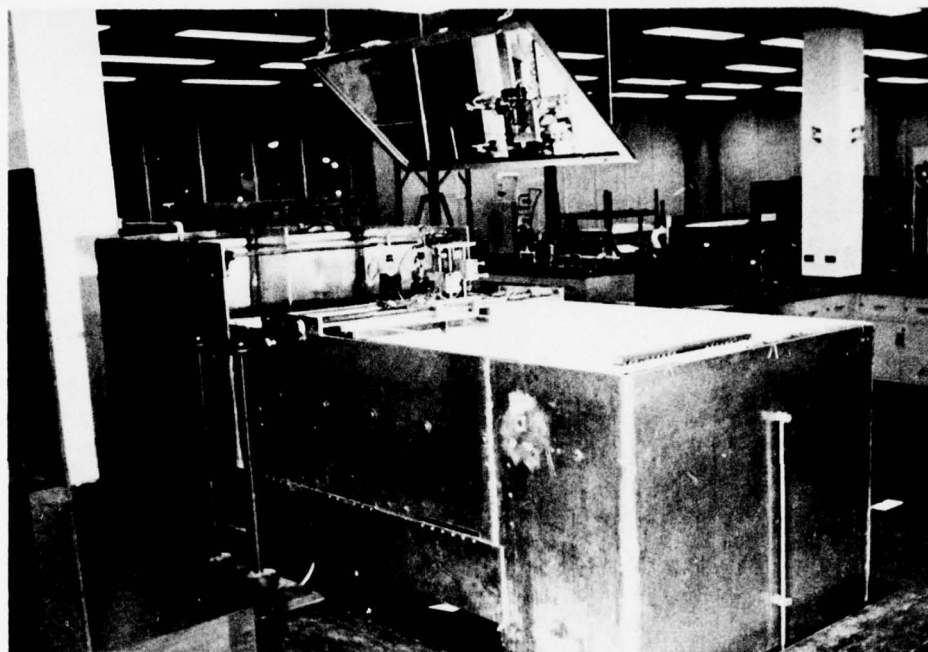


Figure 8. Photograph and Schematic of Water Table Facility

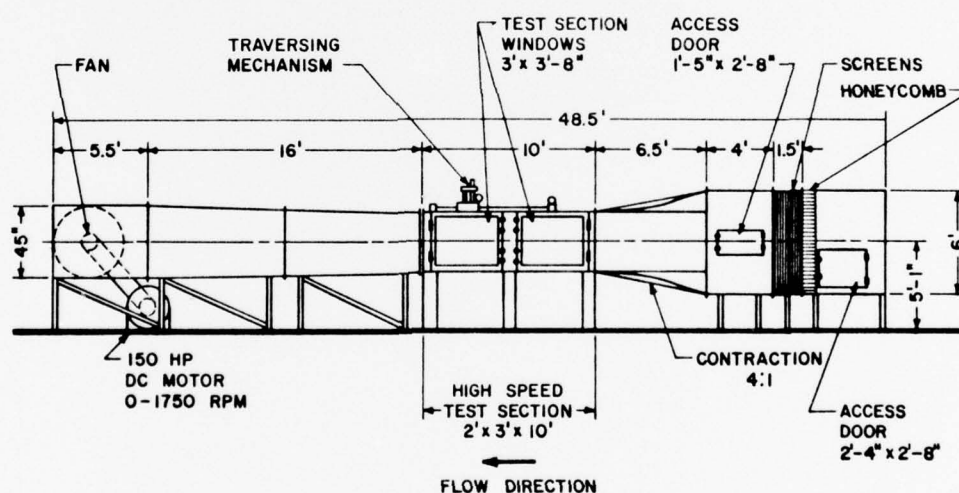
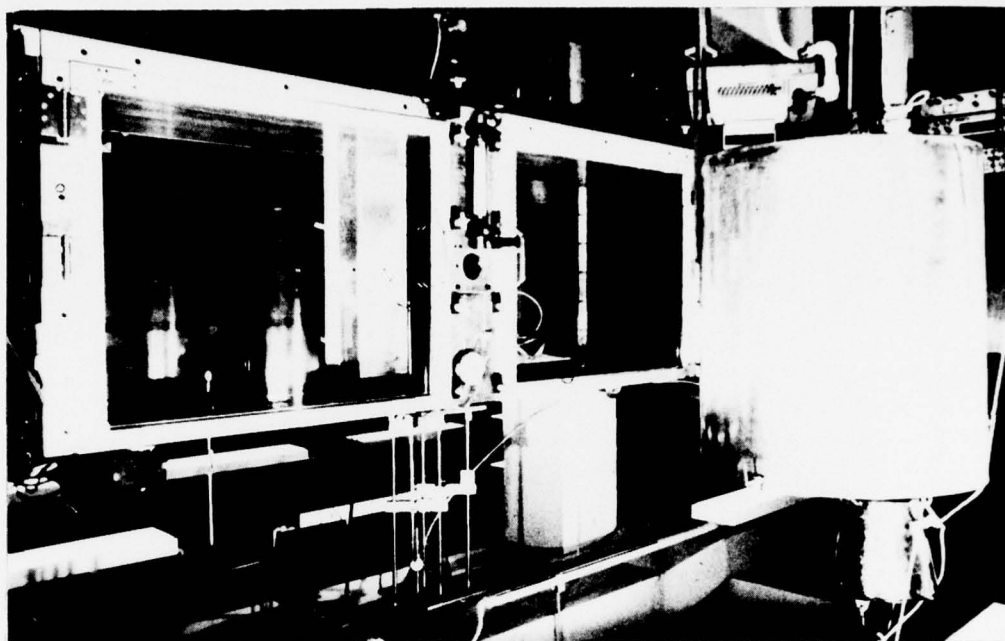


Figure 9. Photograph and Schematic of High Speed Test Section of Environmental Wind Tunnel

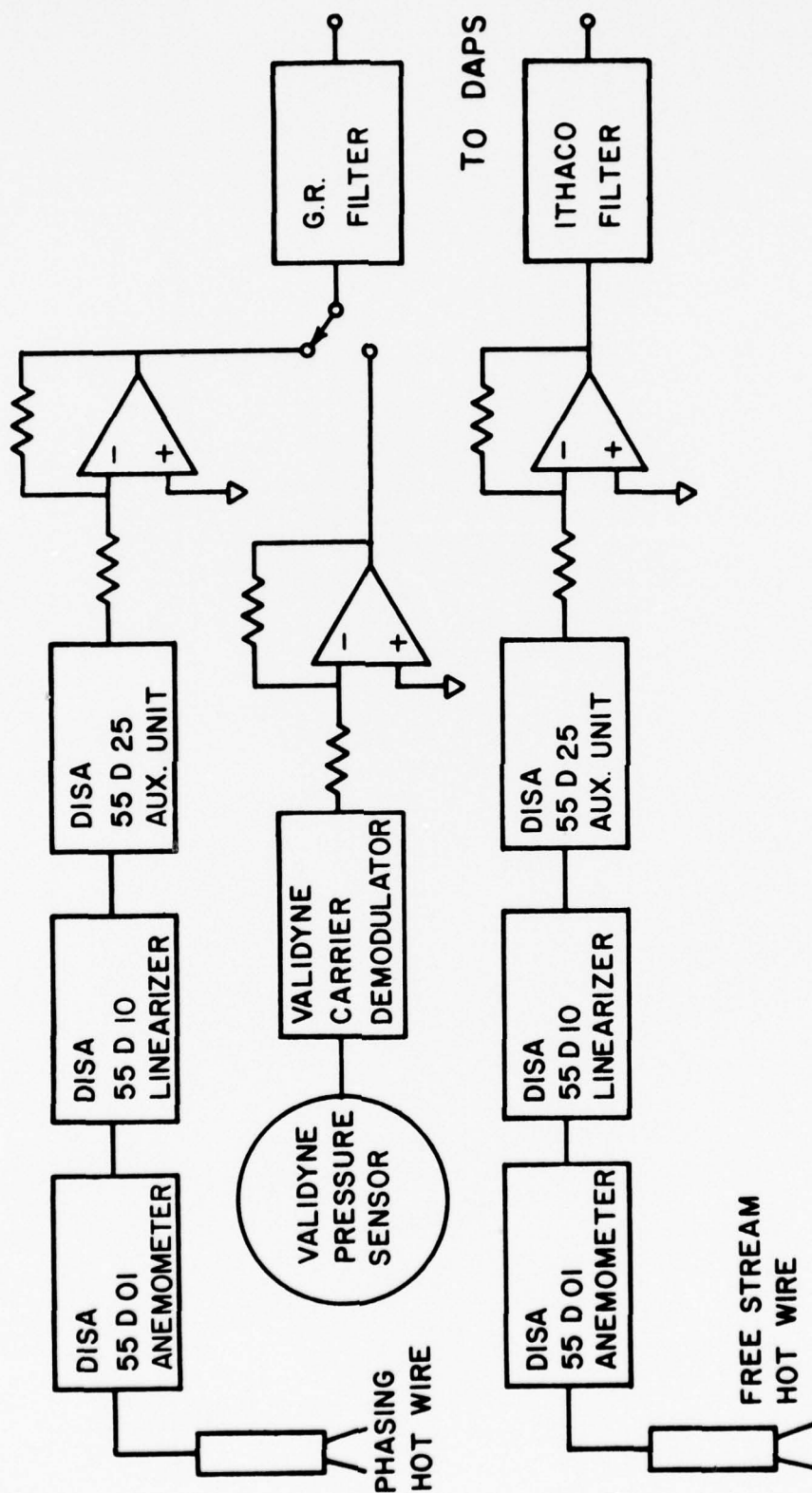


Figure 10. Instrumentation for Wind Tunnel Diagnostic Measurements

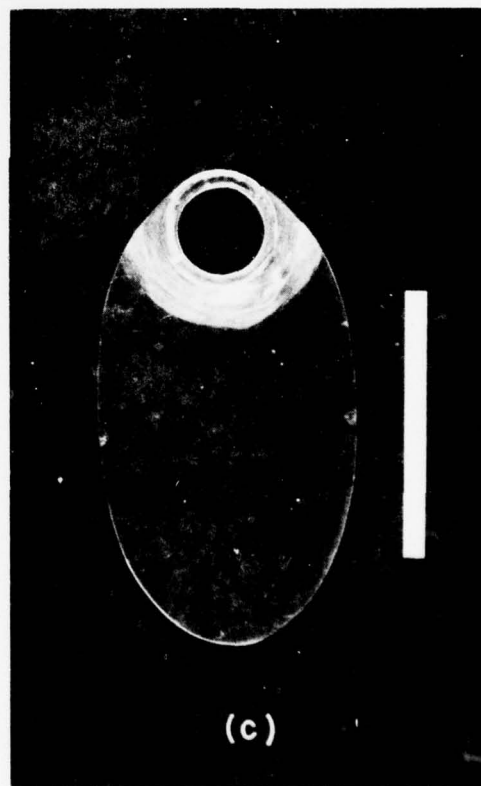
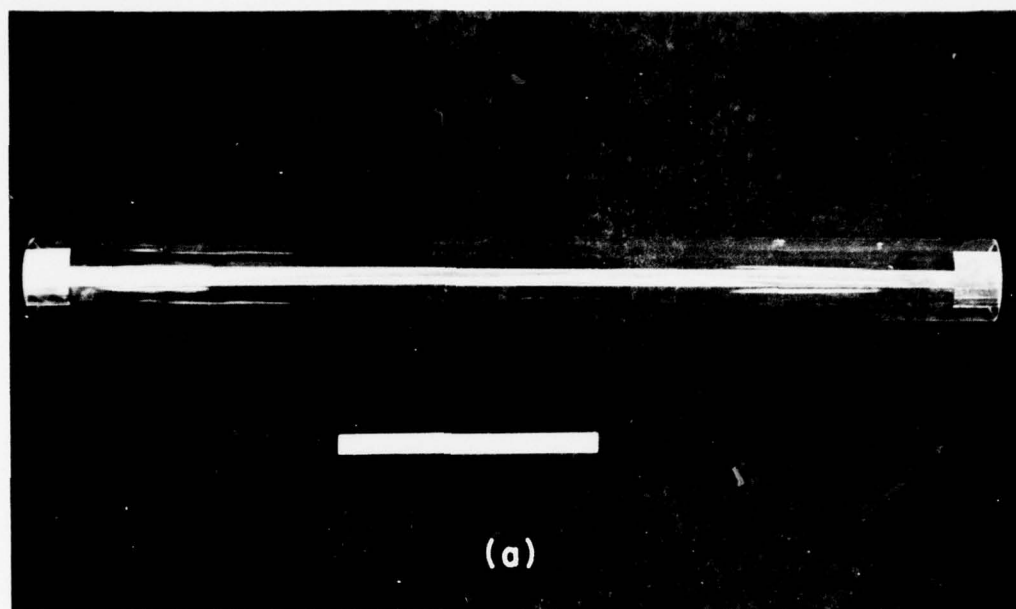


Figure 11. Photographs of Cylinder Model, Heating Strip and End Plate

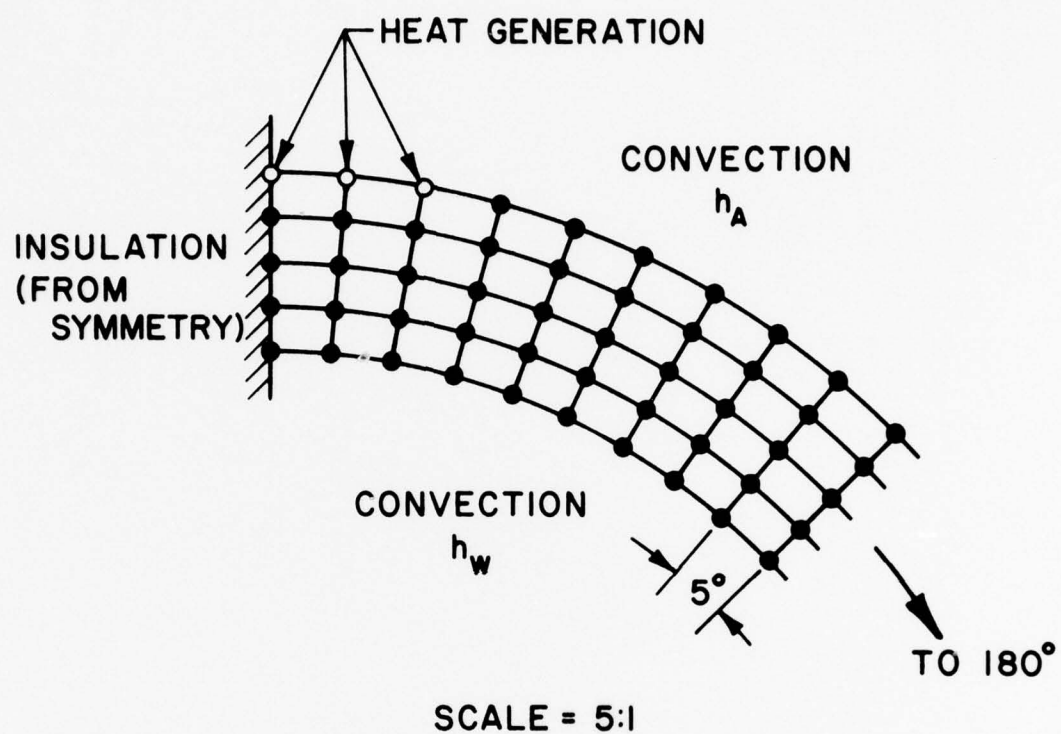


Figure 12. Cylinder Finite Difference Heat Transfer Model

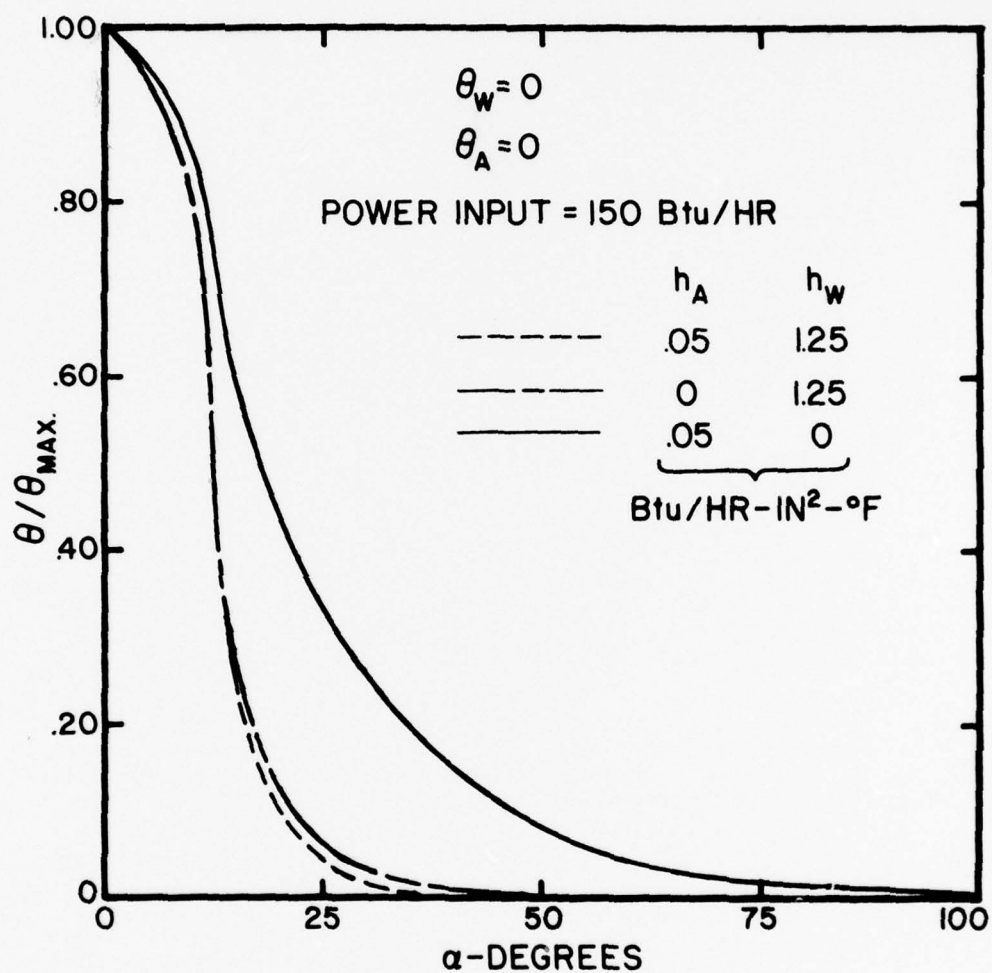


Figure 13. Results of Solution of Difference Equations for Cylinder Heat Transfer Model

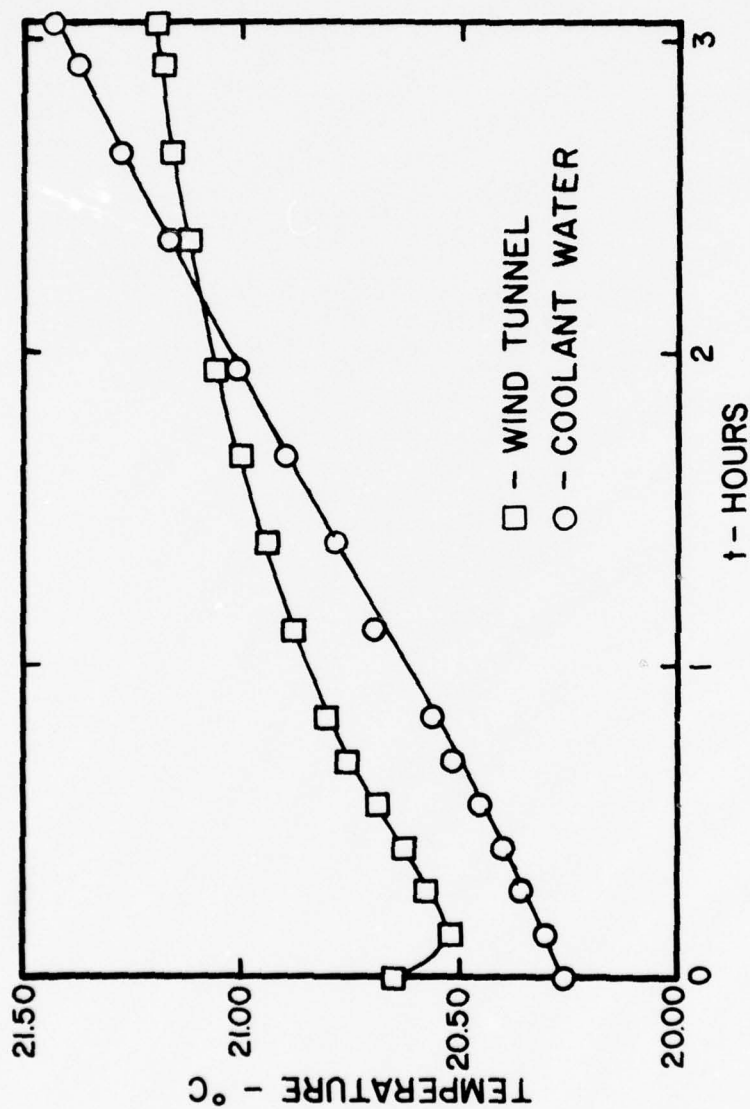


Figure 14. Temperature Drifts in Environmental Wind Tunnel and Cylinder Coolant

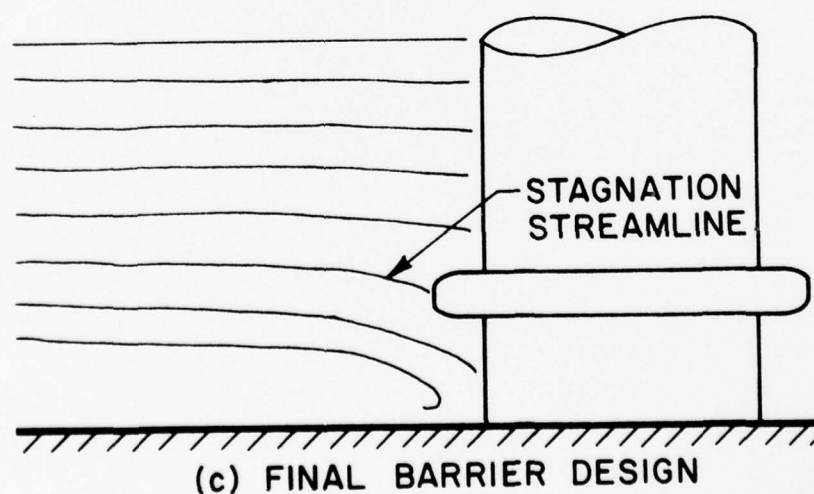
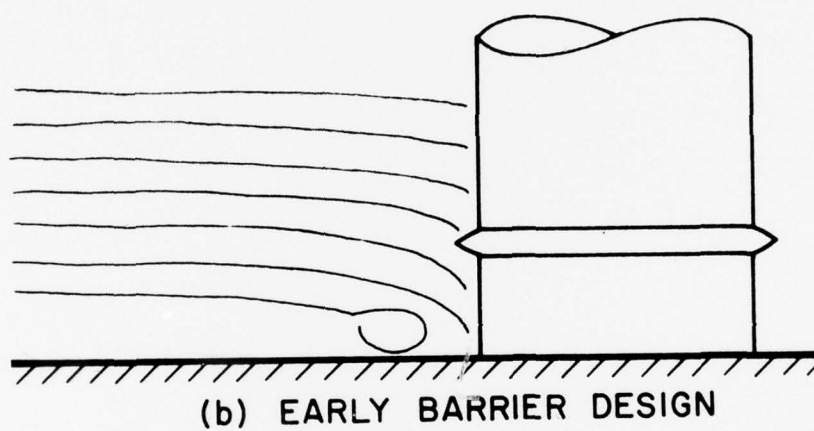
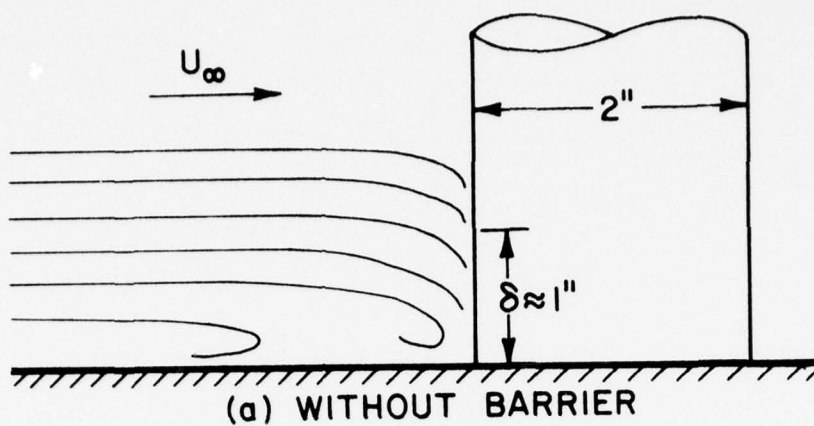


Figure 15. Flow Visualization Diagnostics of Sidewall Boundary Layer Interaction with Flowfield at Front of Cylinder

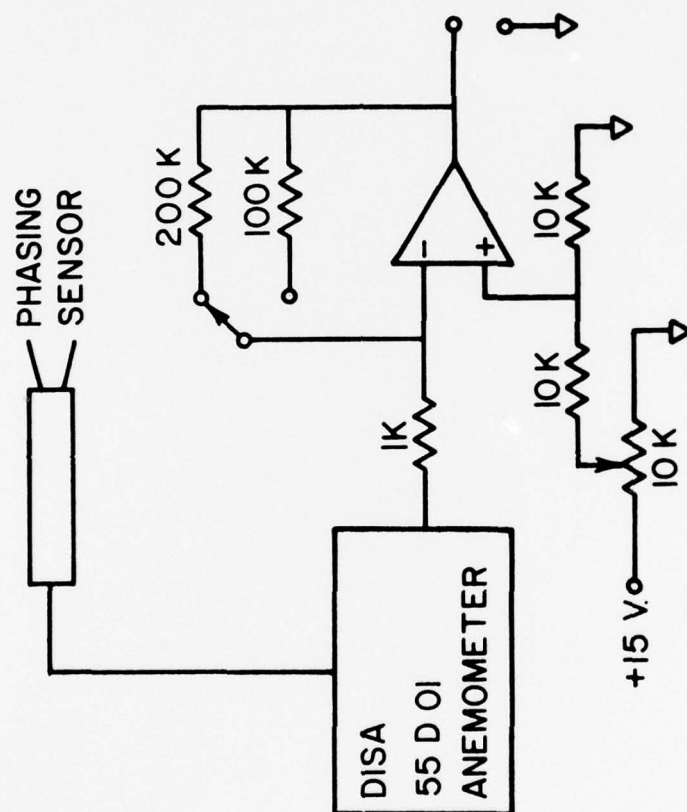


Figure 16. Phasing Velocity Sensor and Electronics

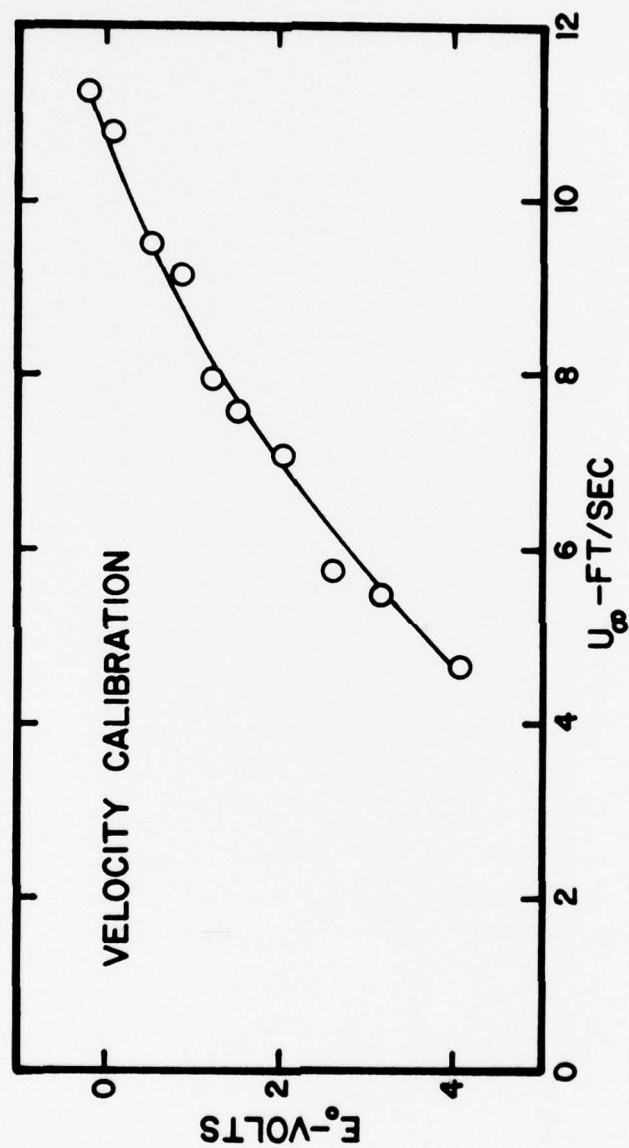


Figure 17. Calibration of Phasing Velocity Measurement Circuit

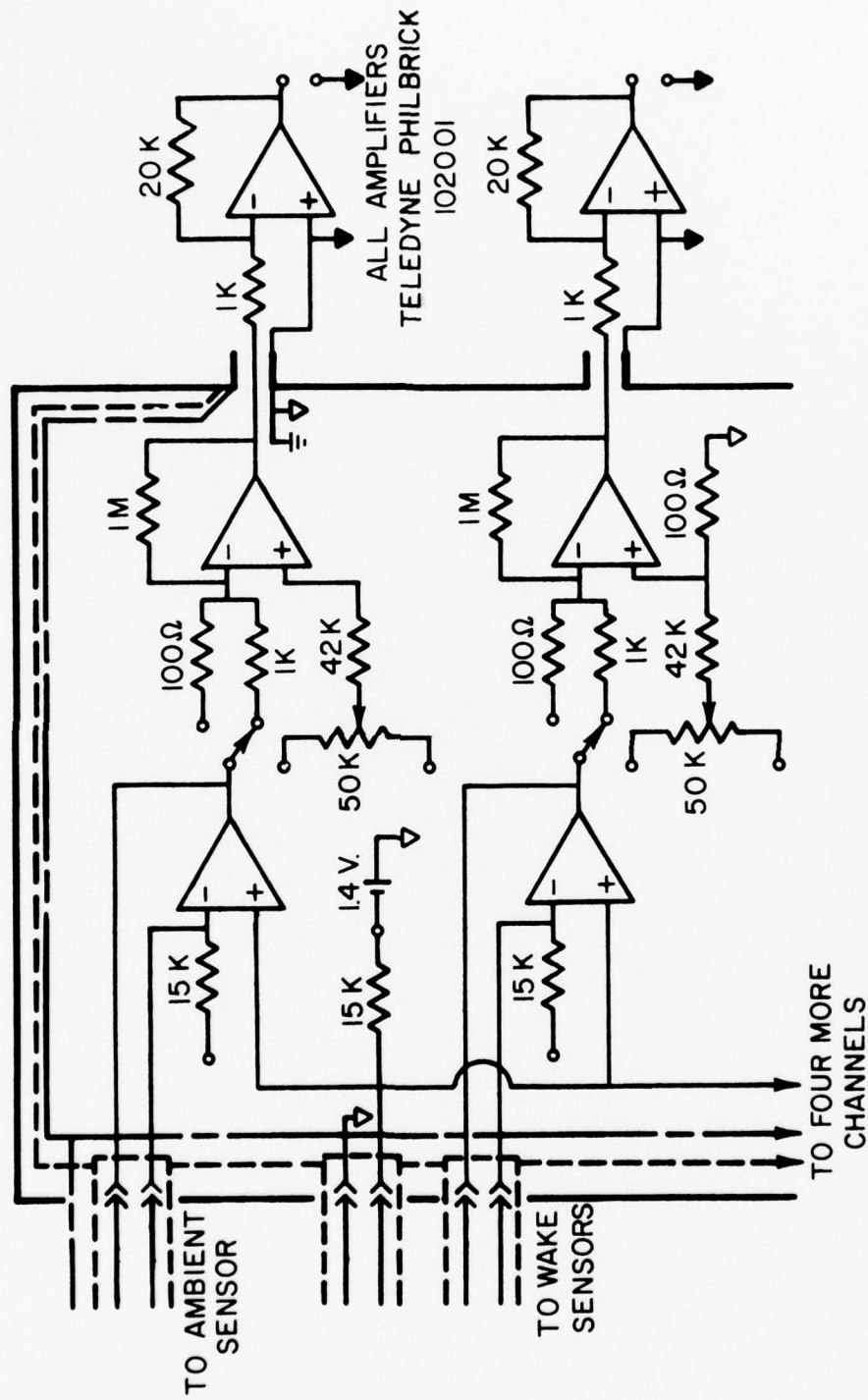


Figure 18. Circuit Diagram of Six Channel Differential Resistance Thermometer

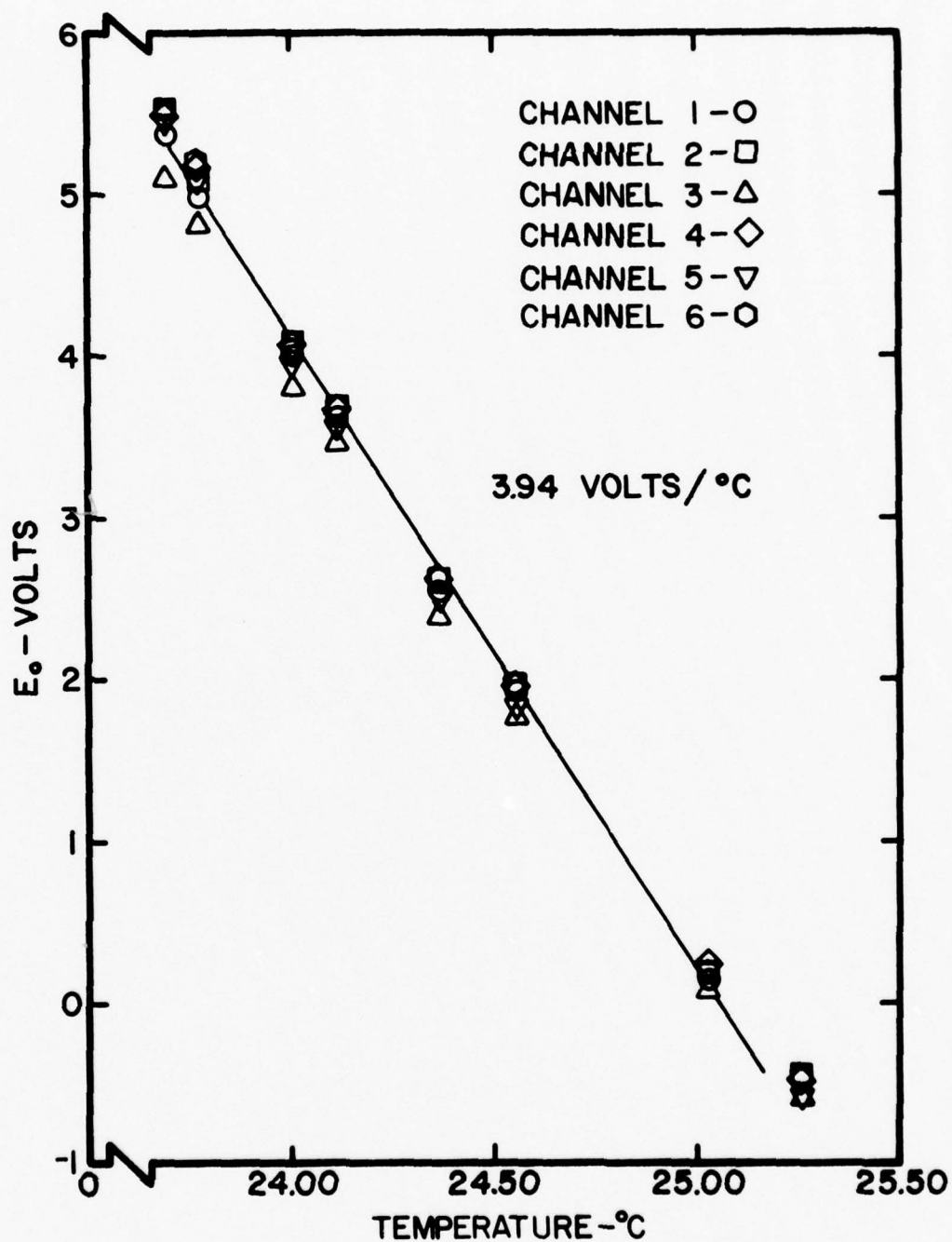
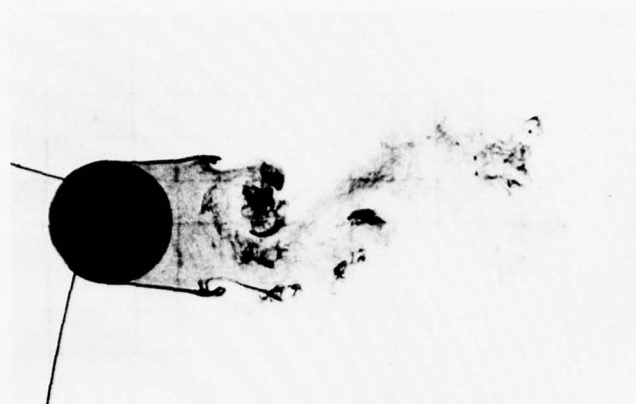
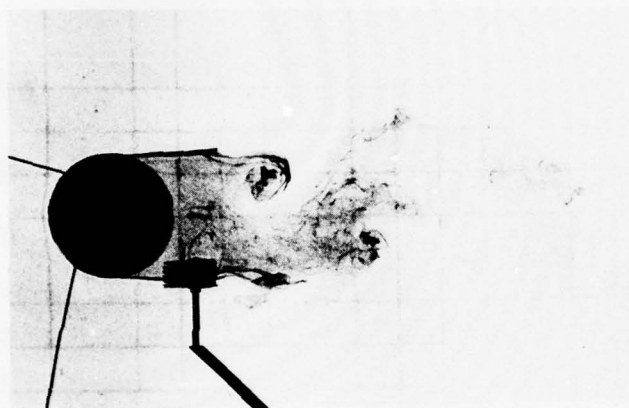


Figure 19. Calibration of Six Channel Differential Resistance Thermometer



(a) WITHOUT
PROBE

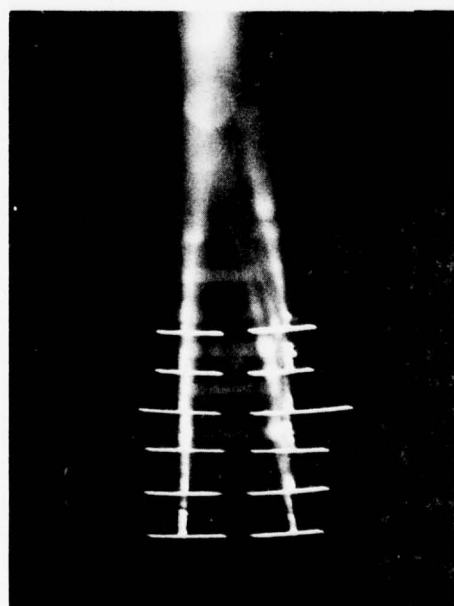
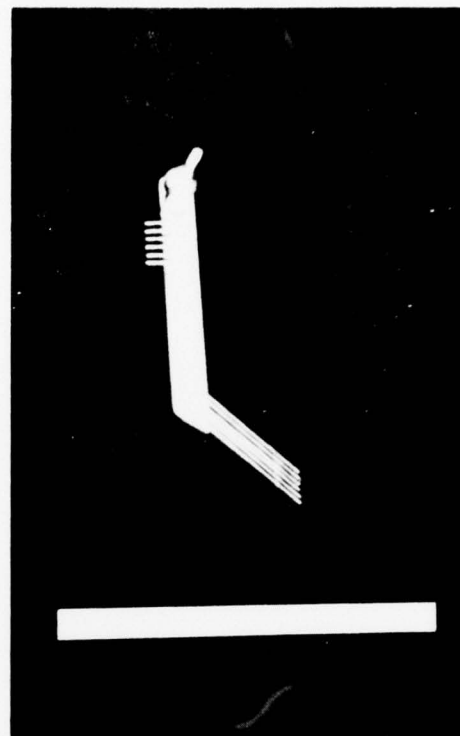
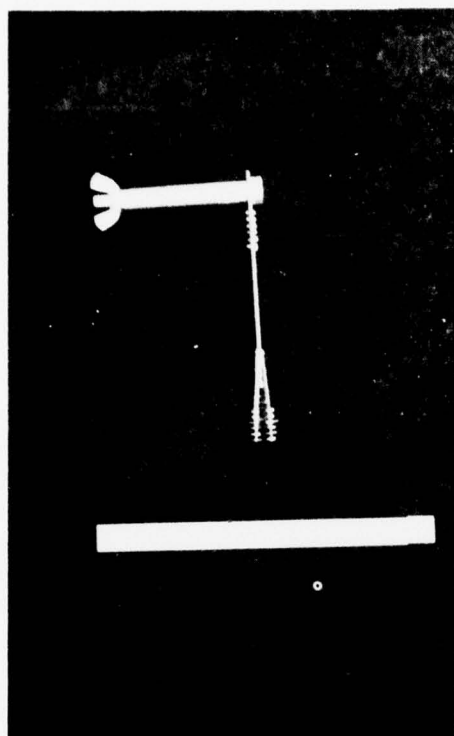


(b) HIGH
STAGNATION
PROBE



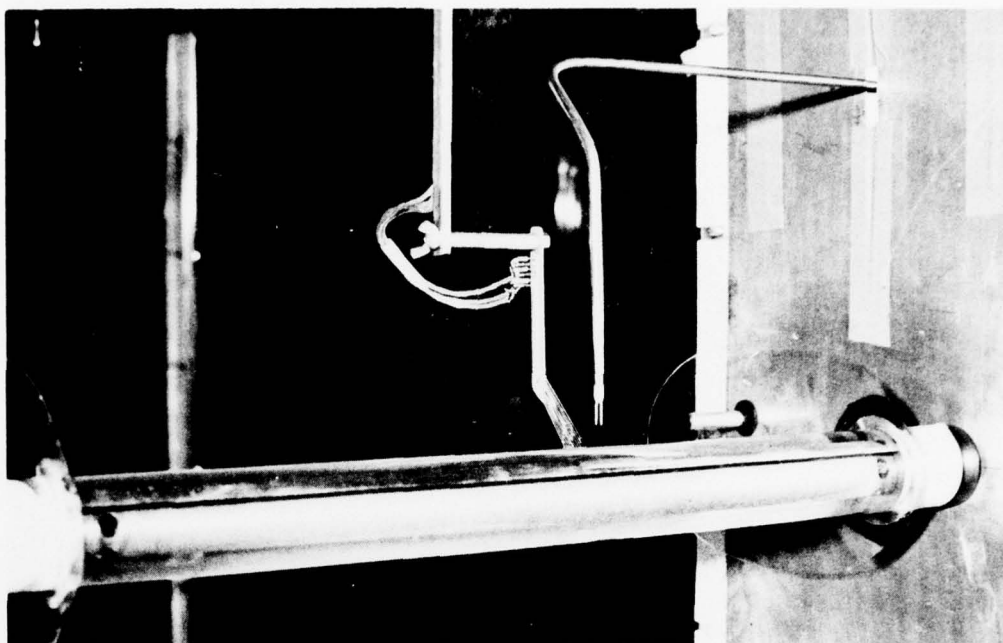
(c) LOW
INTERFERENCE
PROBE

Figure 20. Dye Flow Visualization of Interaction of Six-Sensor Probe with Cylinder Wake

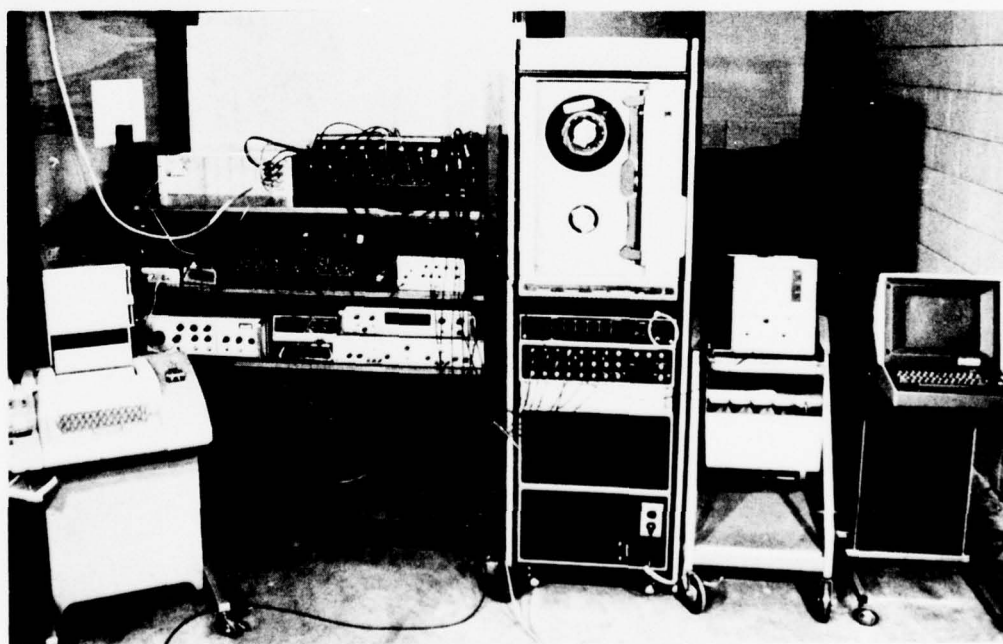


TEMPERATURE
PROBE

Figure 21. Different Views and Close-up of Six-Sensor
Temperature Probe



(a) CYLINDER MODEL WITH PROBES



(b) INSTRUMENTATION

Figure 22. Photographs of Cylinder Model with Probes and Instrumentation

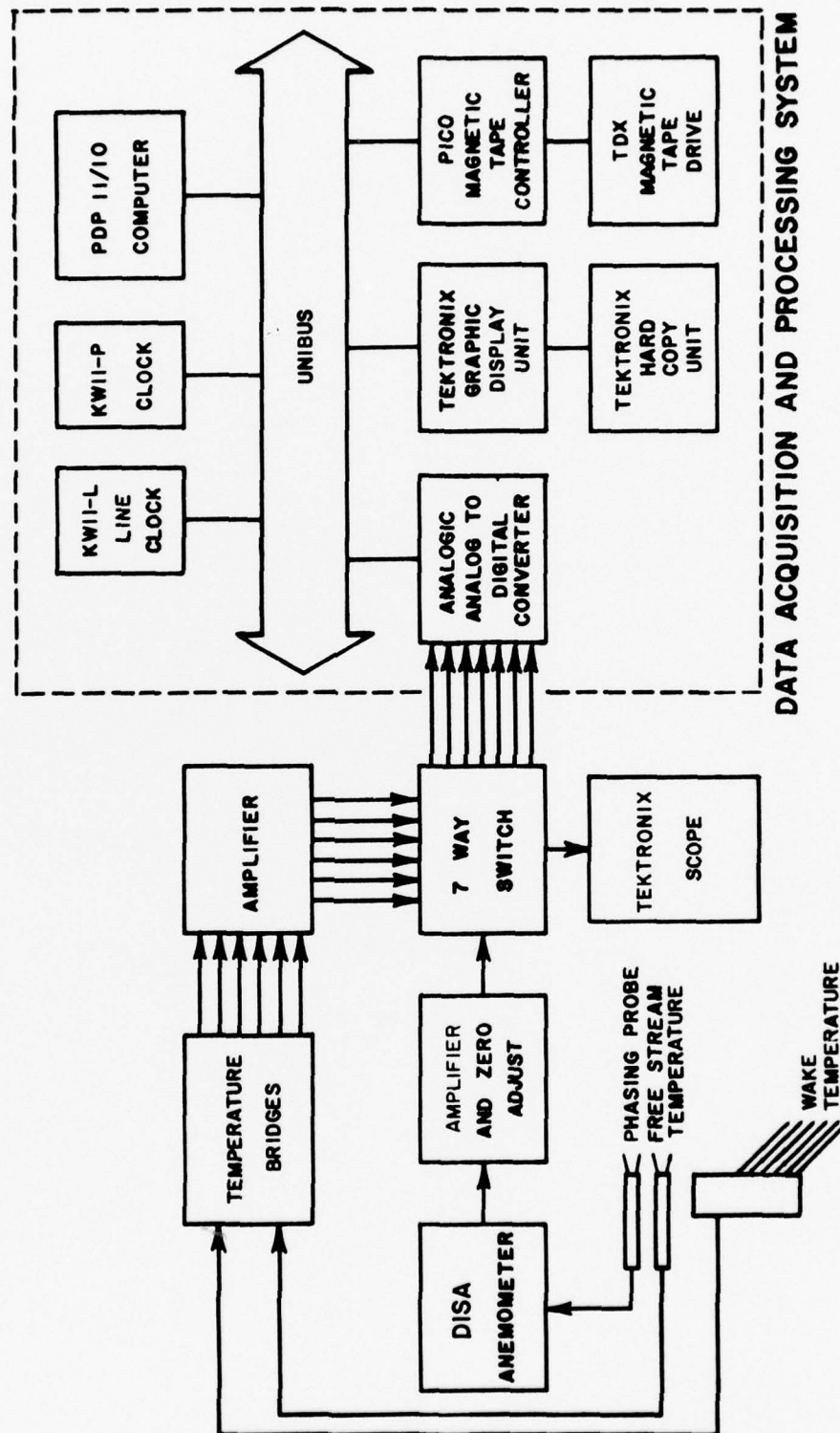


Figure 23. Analog Instrumentation and Data Processing System

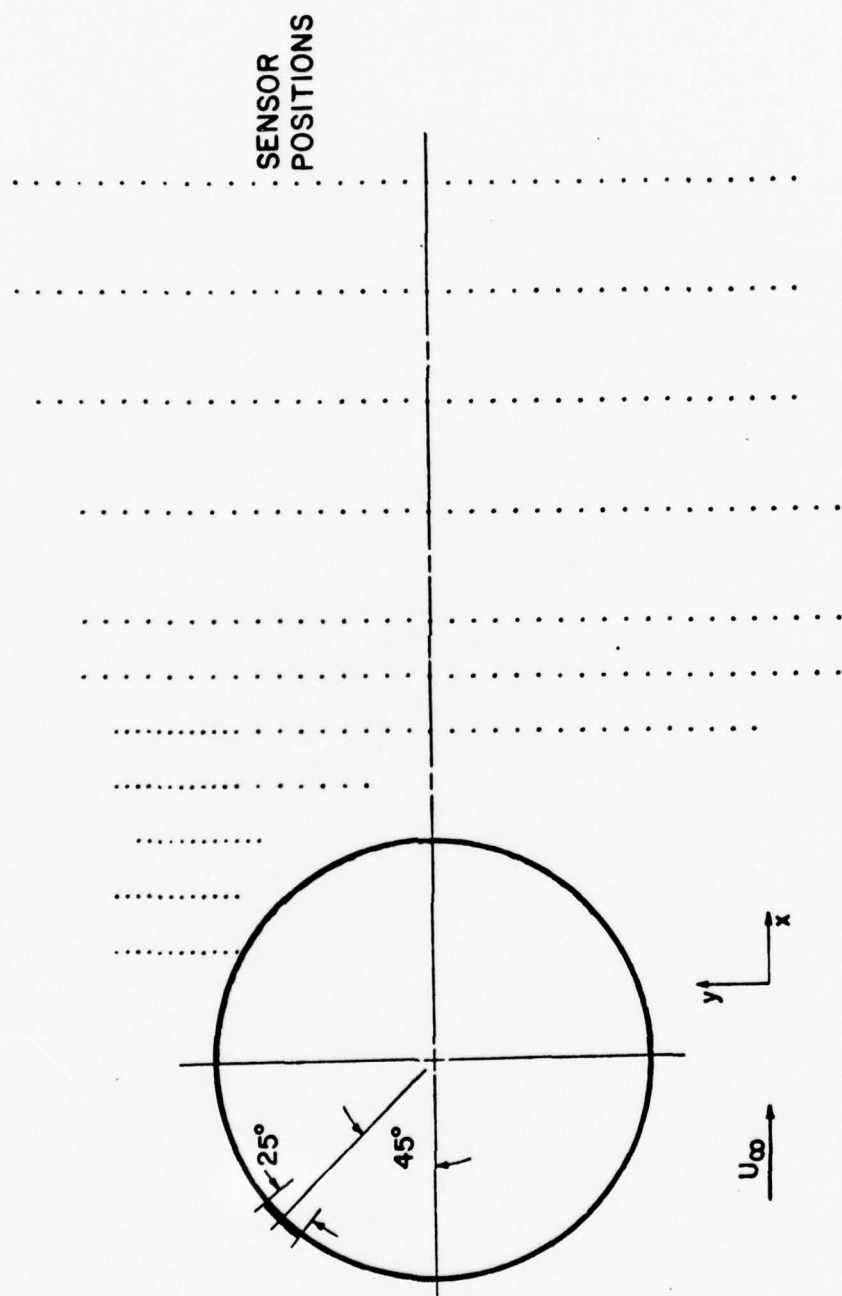


Figure 24. Wake Sensor Locations with Respect to Cylinder Model

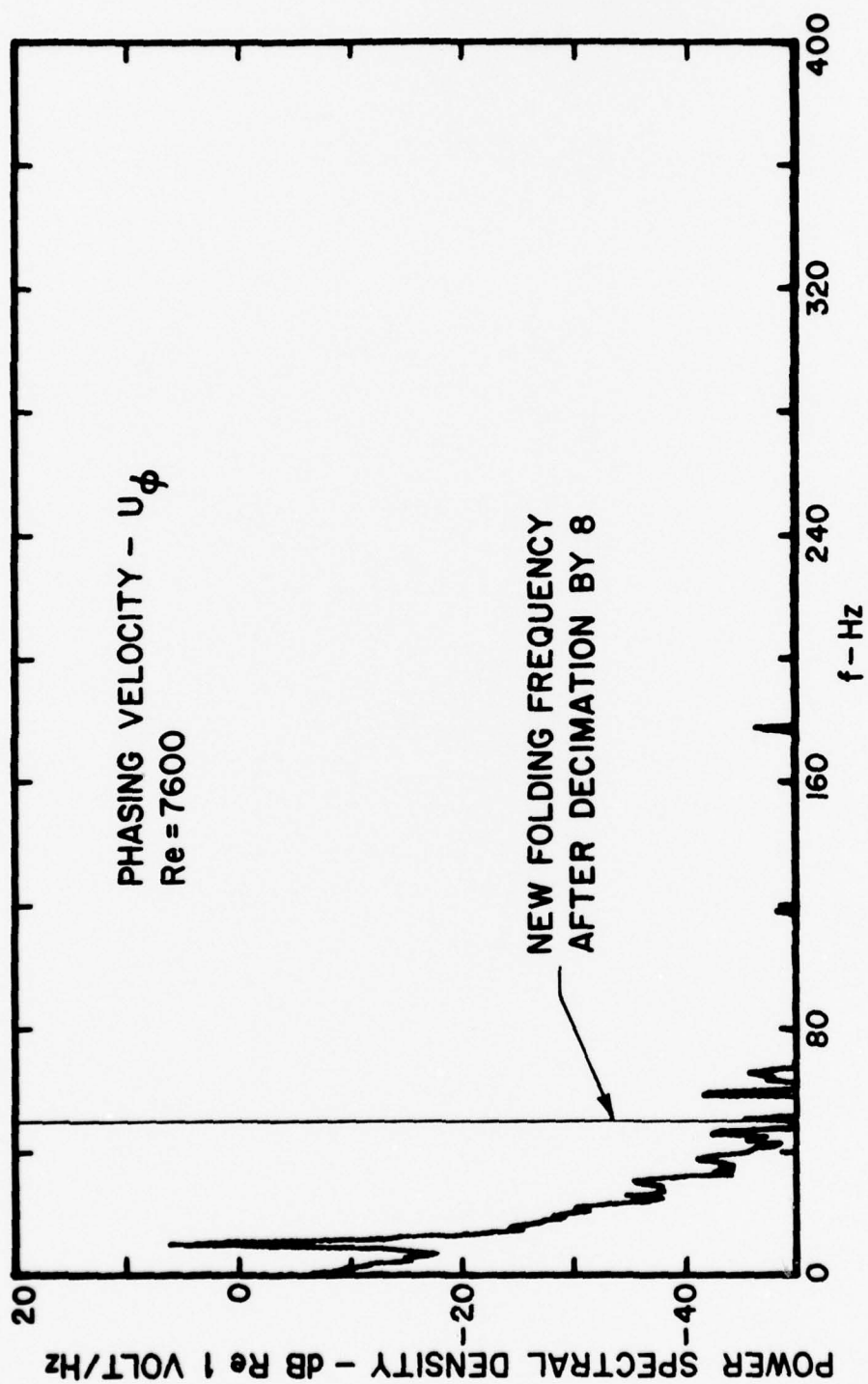


Figure 25. Log Power Spectral Density of Oversampled Phasing Velocity, U_ϕ

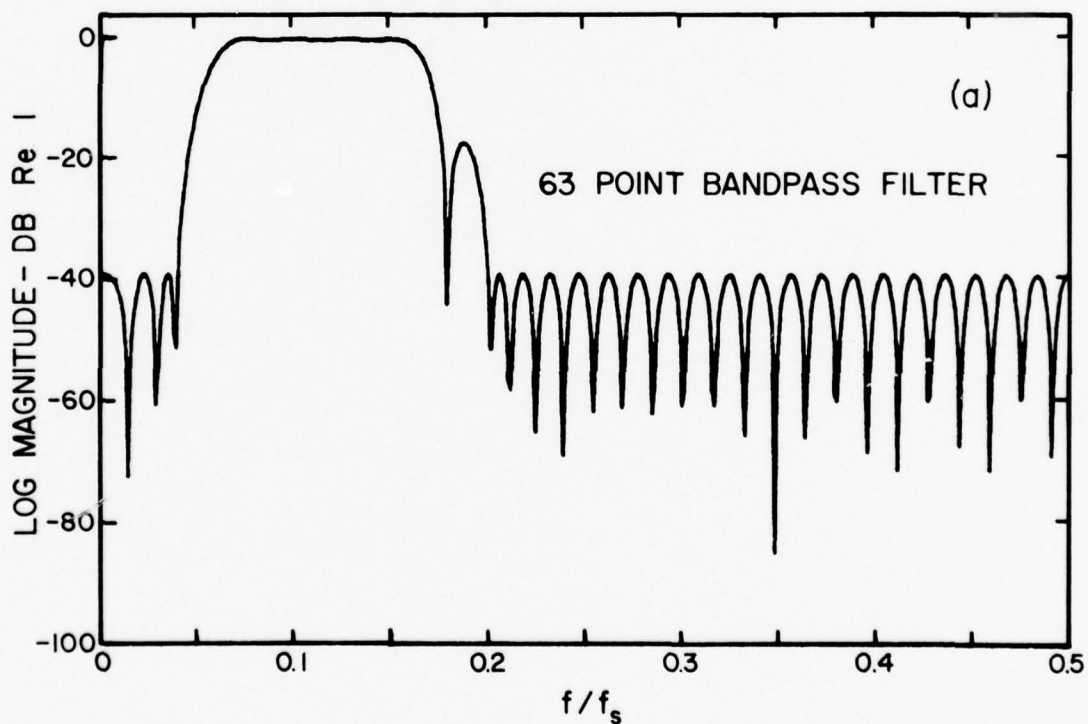
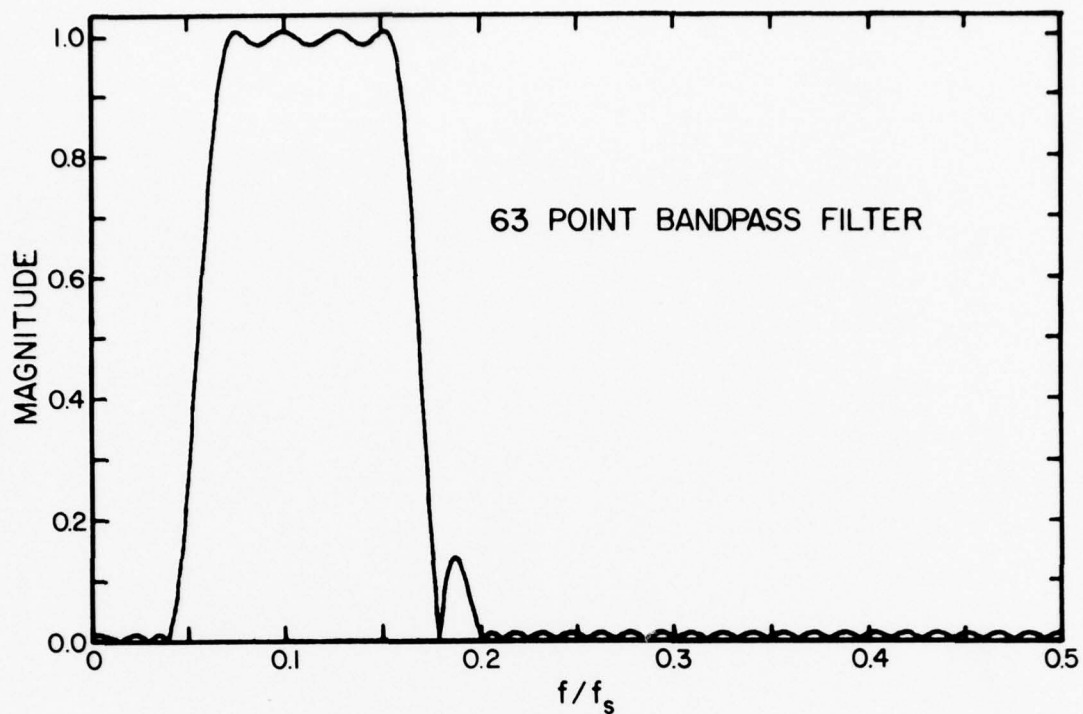


Figure 26. Linear and Log Magnitude Frequency Response of 63 Point Bandpass Filter

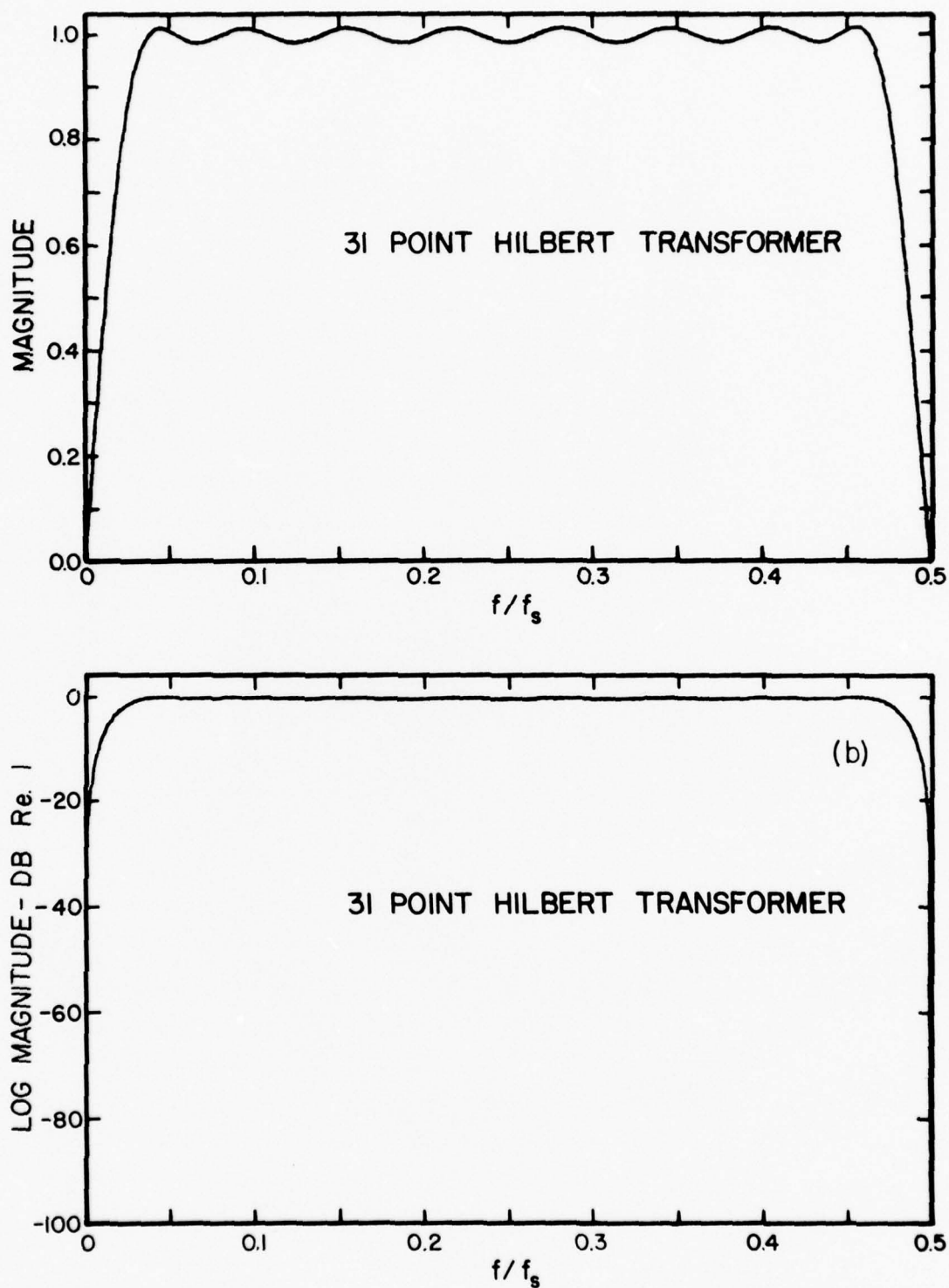


Figure 27. Linear and Log Magnitude Frequency Response of 31 Point Hilbert Transformer

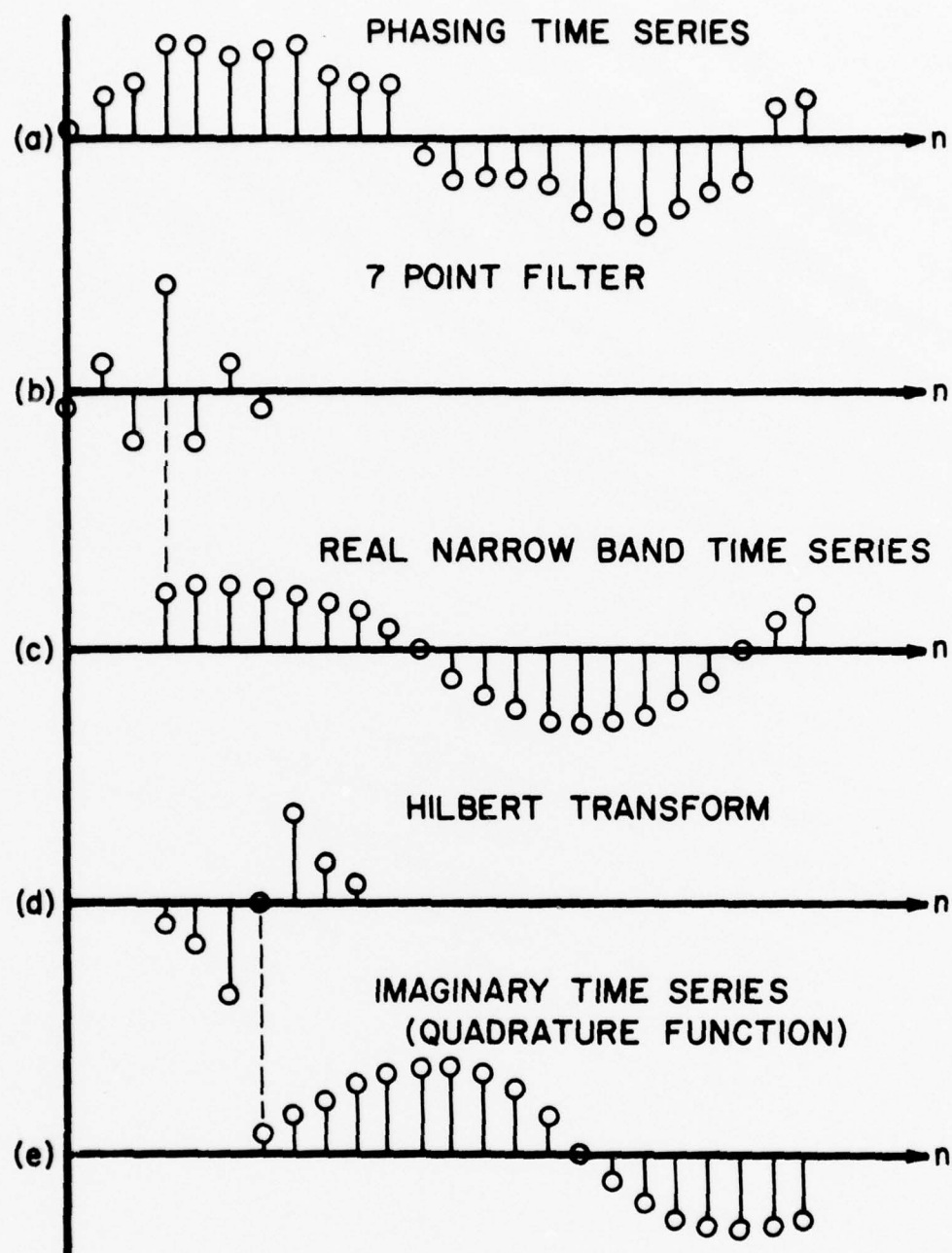


Figure 28. Illustration of Starting Losses for Digital Filter and Hilbert Transformer

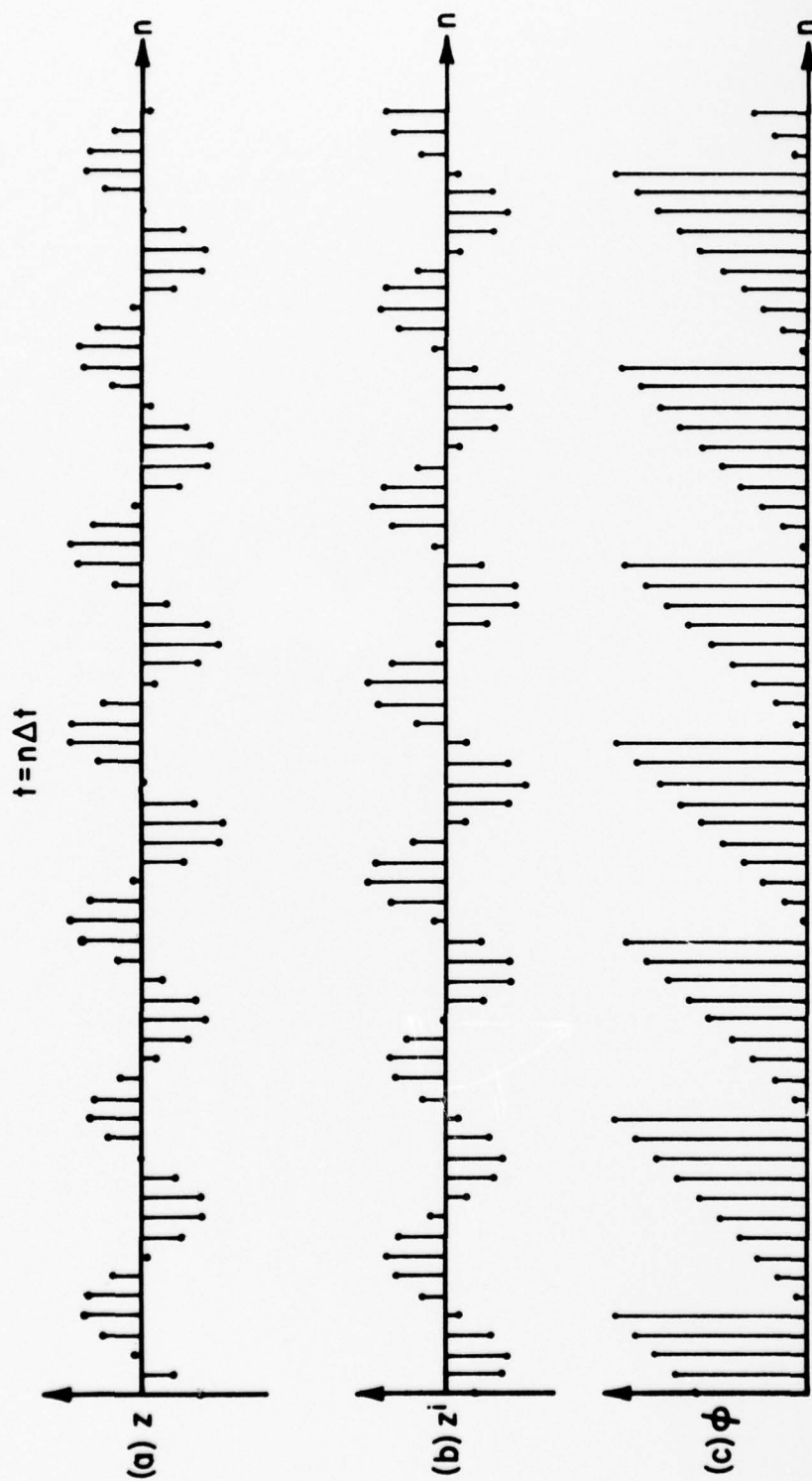


Figure 29. Bandlimited Function $z(t)$, Quadrature Function $z^i(t)$, and Phase Angle $\phi(t)$ Computed From U_ϕ

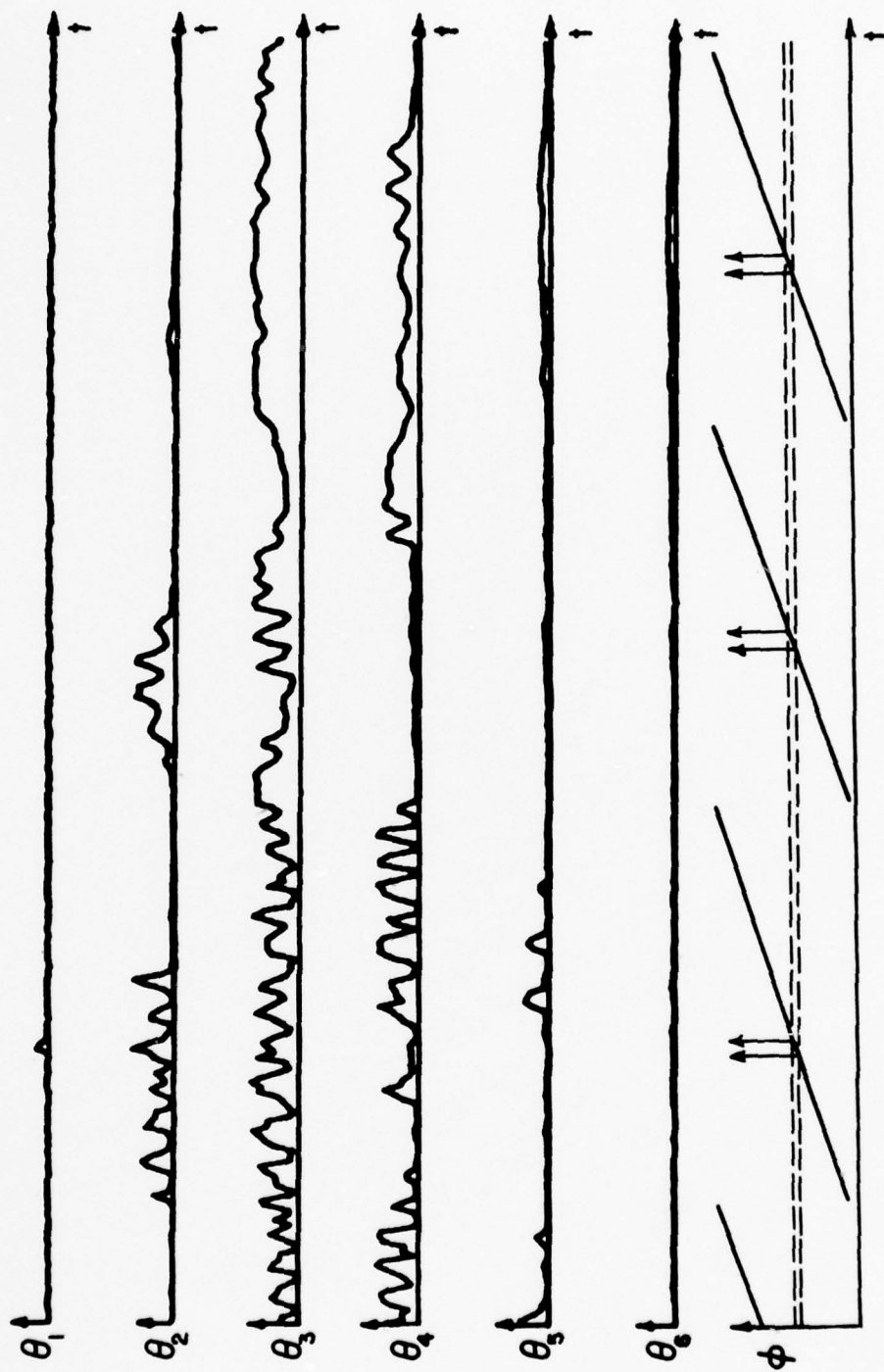


Figure 30. Example of Six-Sensor Temperature Information Conditionally Sampled Based on Phase

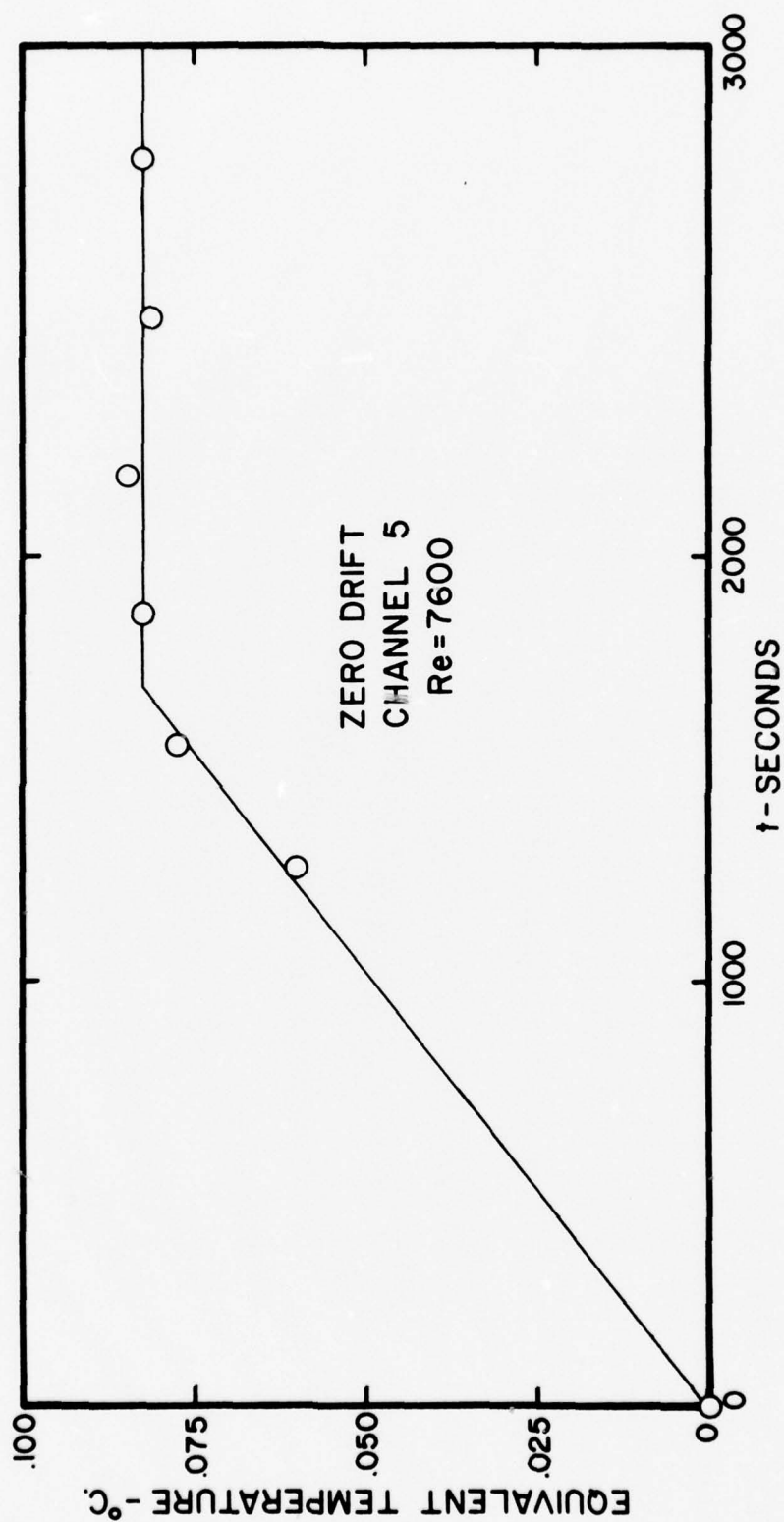


Figure 31. Linear Compensation for Drift in Channel Five Temperature Circuit

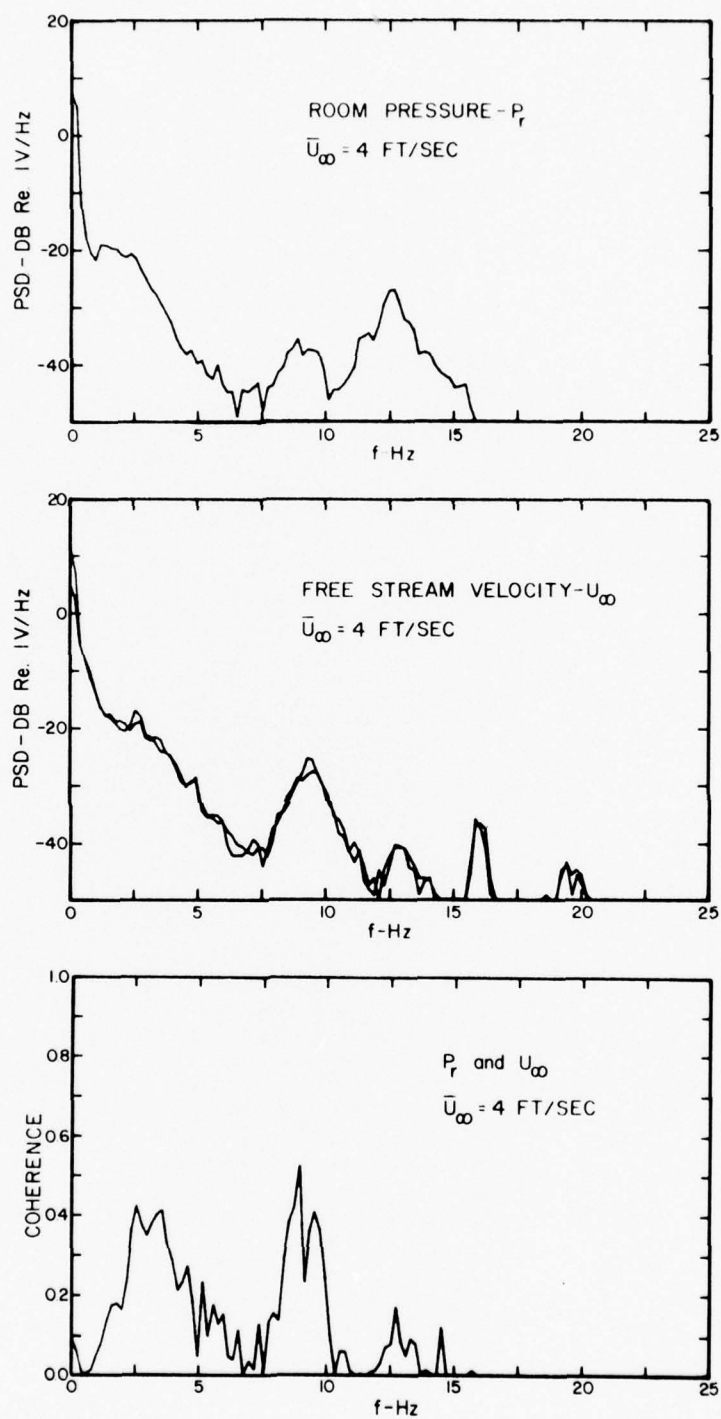


Figure 32. Comparison of Room Pressure and Free Stream Velocity for $U_\infty = 4$ ft/sec

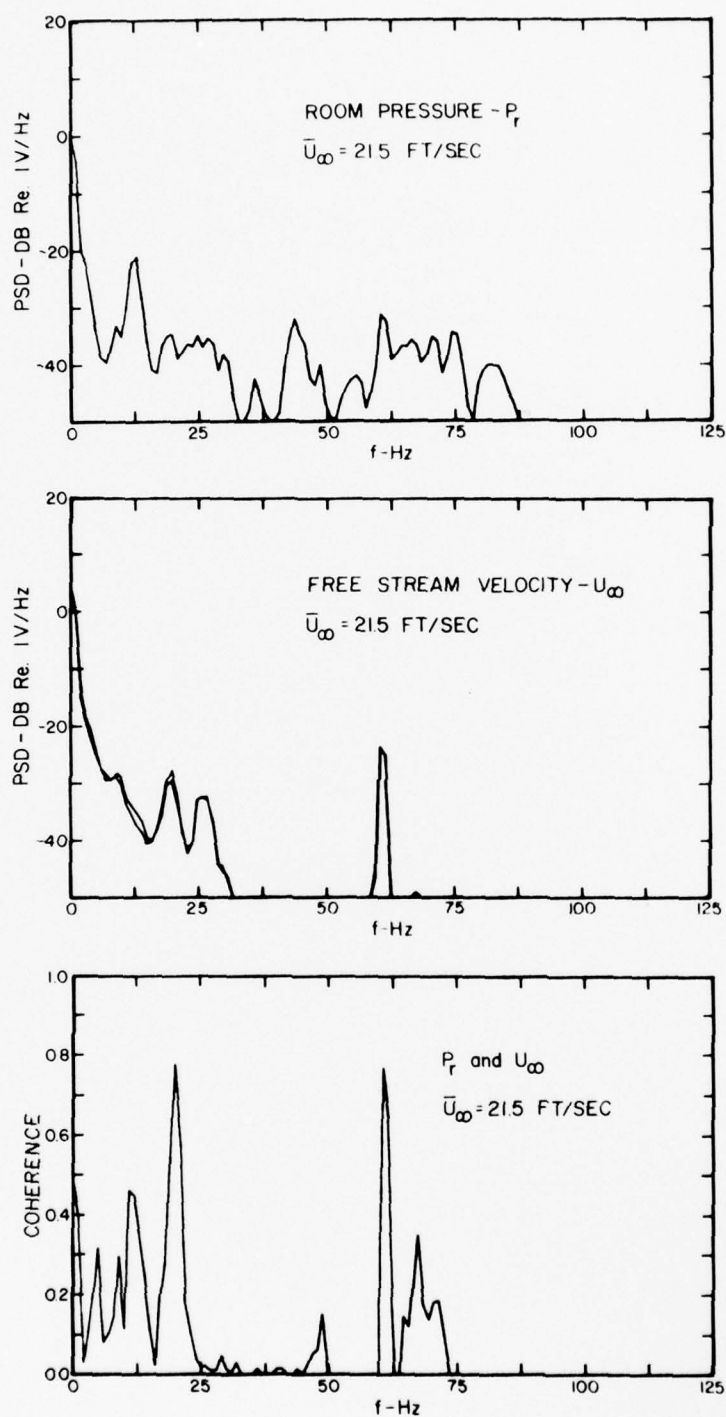


Figure 33. Comparison of Room Pressure and Free Stream Velocity for $U_\infty = 21.5$ ft/sec

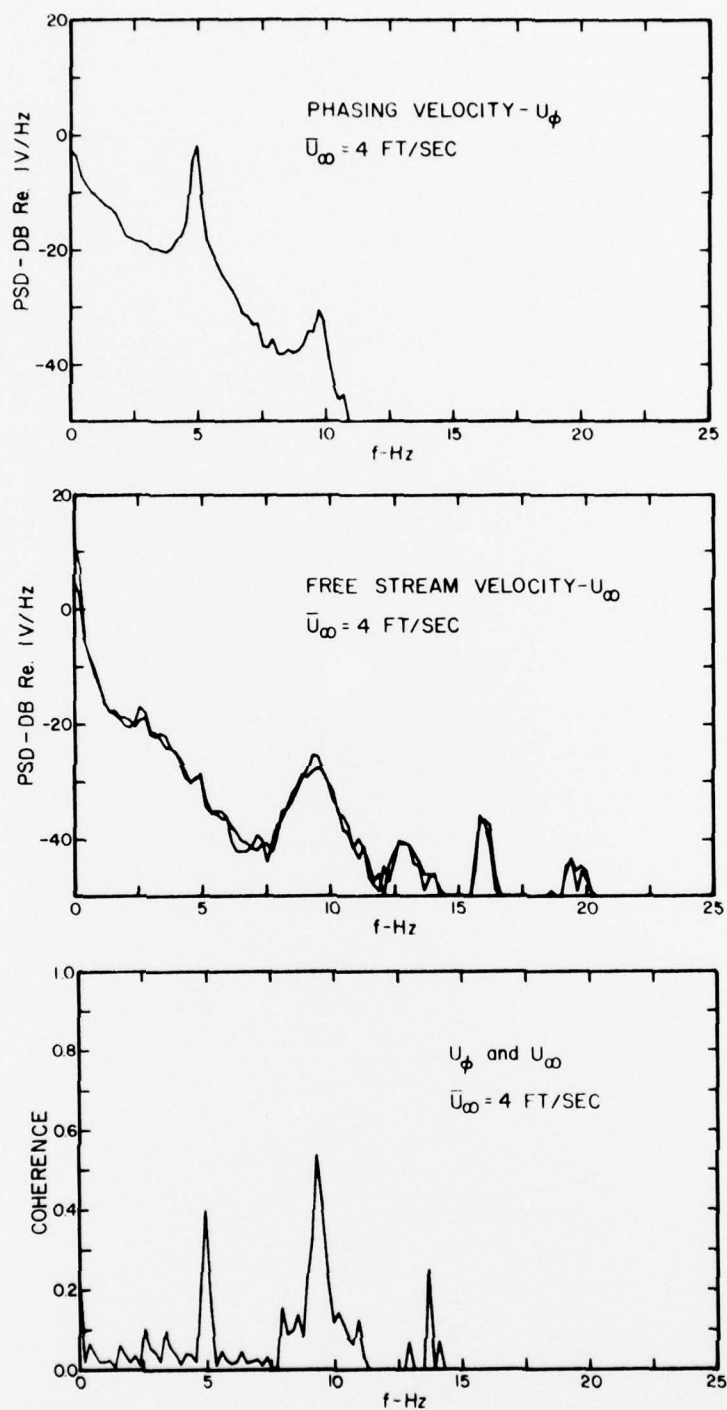


Figure 34. Comparison of Phasing Velocity and Free Stream Velocity for $U_\infty = 4$ ft/sec

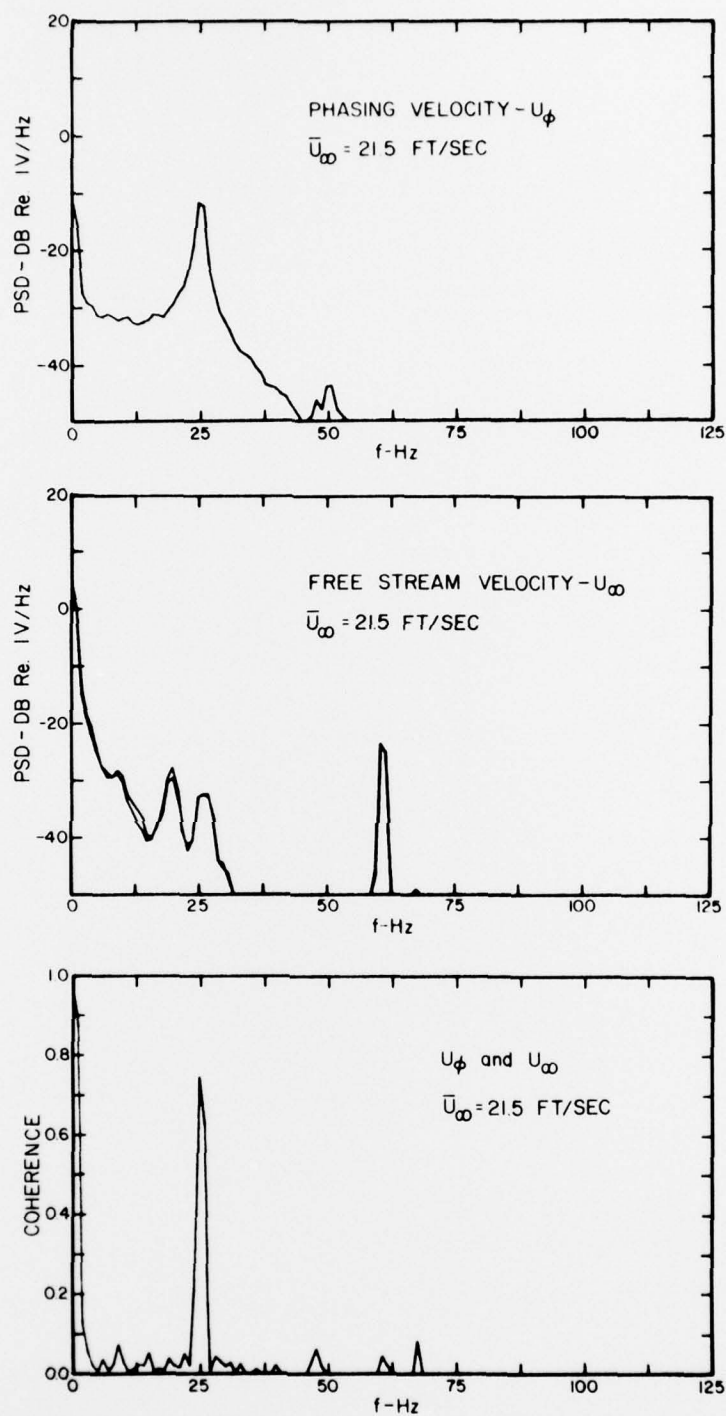


Figure 35. Comparison of Phasing Velocity and Free Stream Velocity for $U_\infty = 21.5$ ft/sec

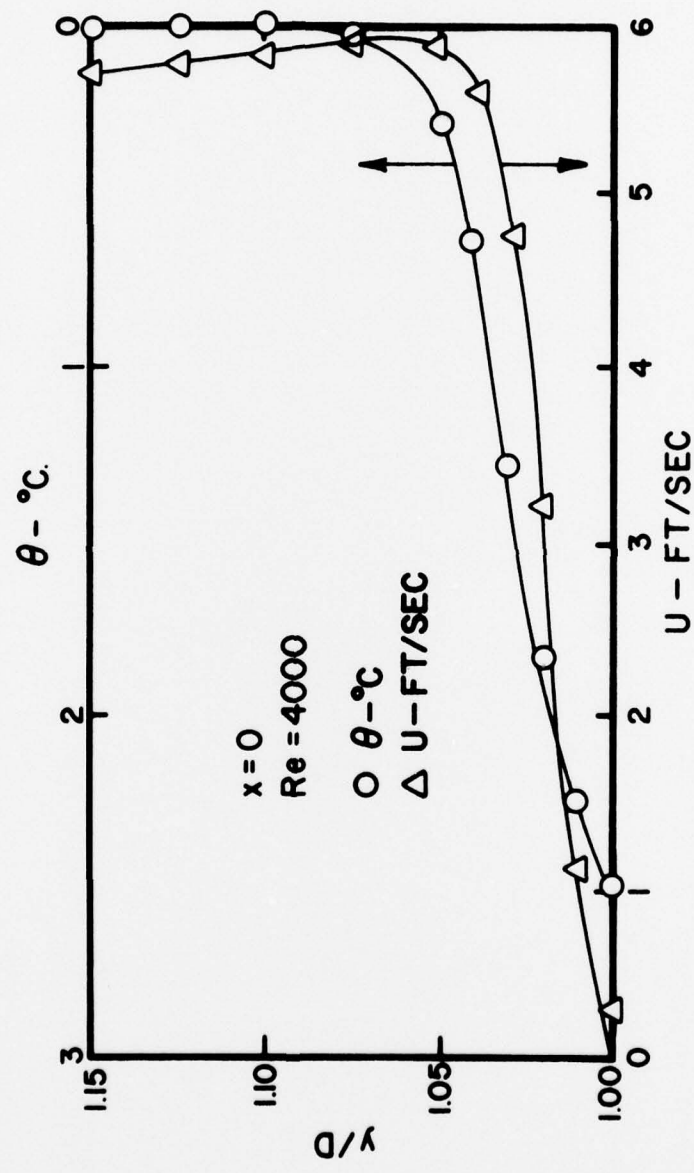


Figure 36. Mean Temperature and Velocity Profiles of Cylinder Boundary Layer near Separation Line

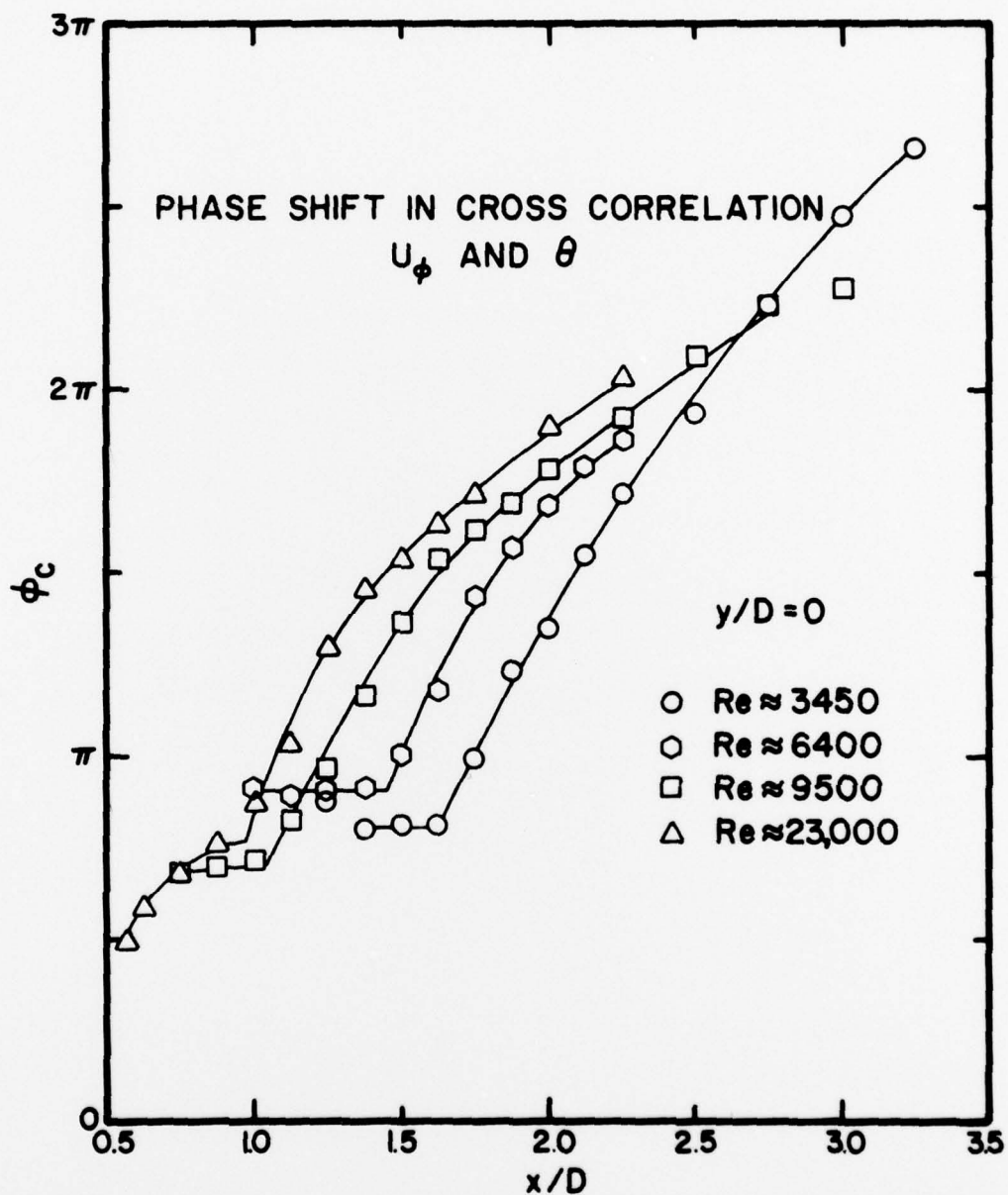


Figure 37. Phase Shift in Cross Correlation of U_ϕ and θ as a Function of Temperature Sensor Downstream Position

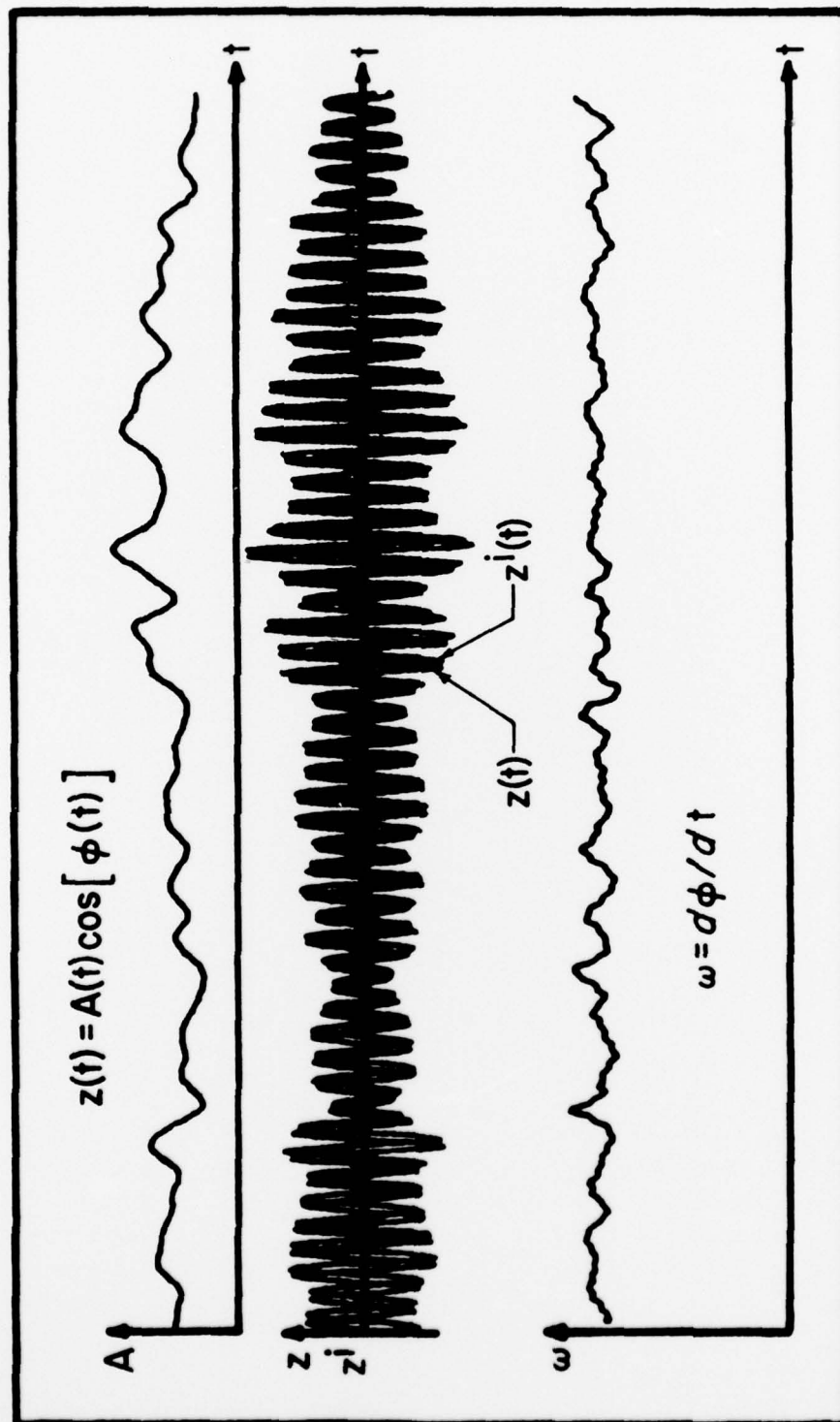


Figure 38. Instantaneous Amplitude and Frequency as Computed from Sample U_ϕ Data

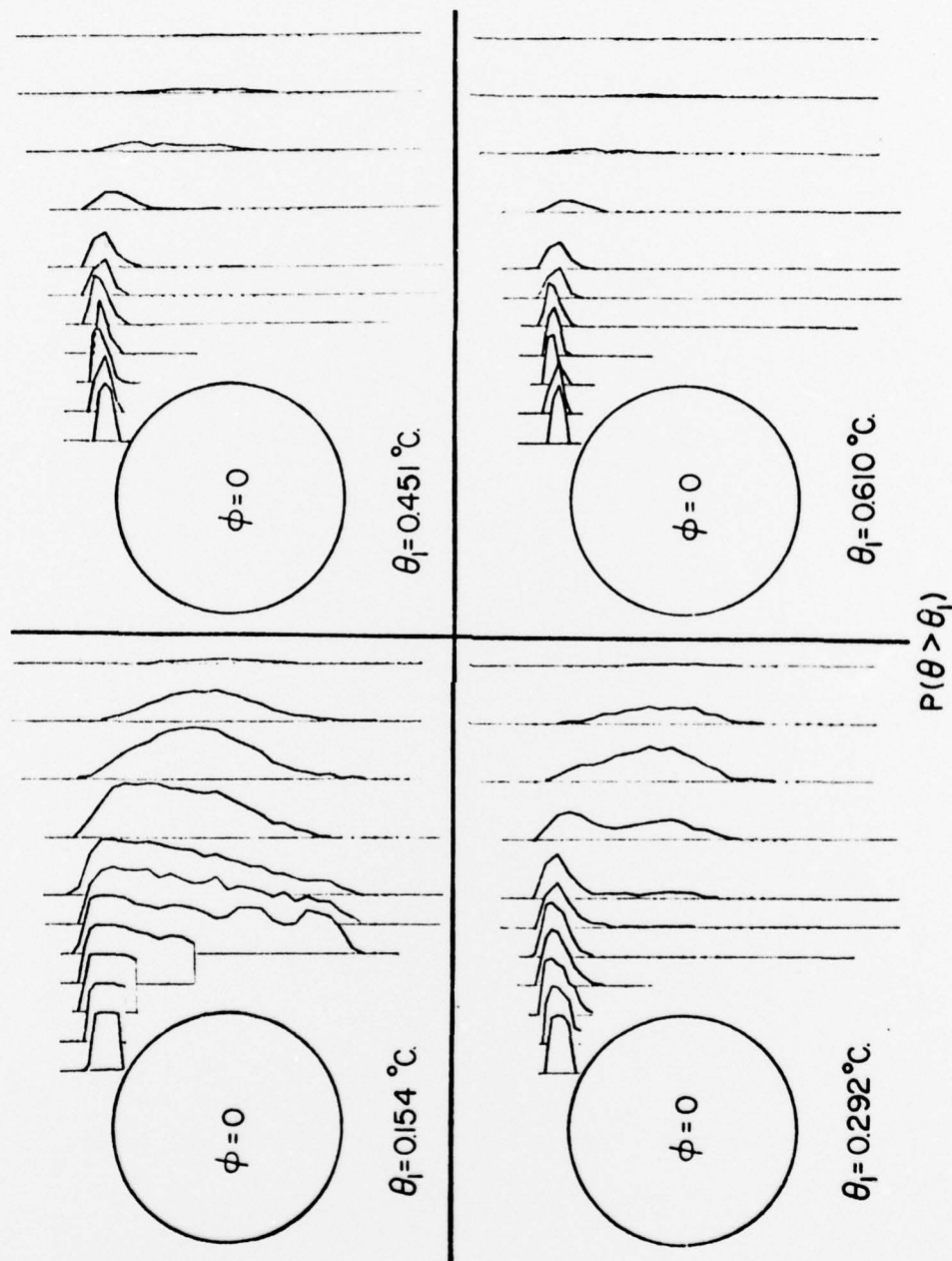


Figure 39. Dependence of Probability Distributions on Temperature Threshold Level for $\phi=0$

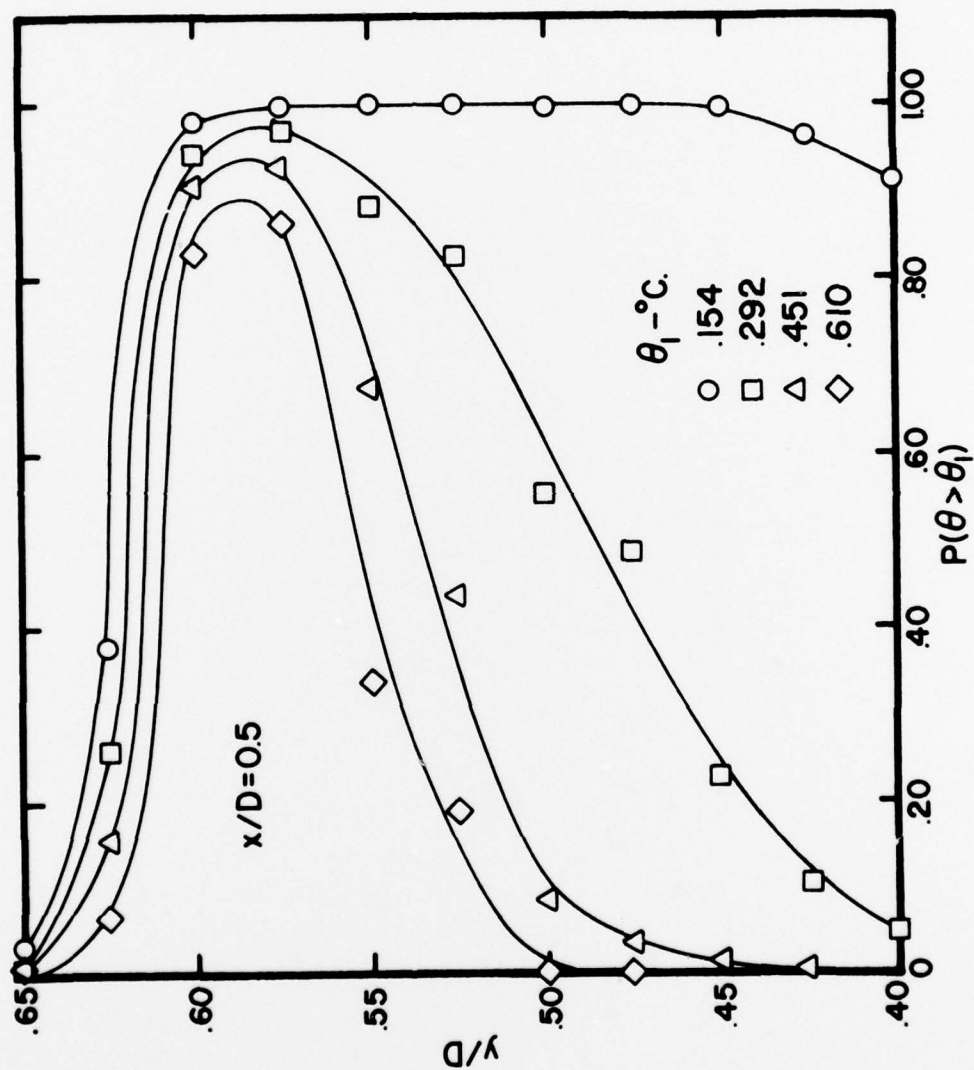


Figure 40. Dependence of Probability Distributions on Temperature Threshold Level for $\zeta=0$ at $x/D=0.5$

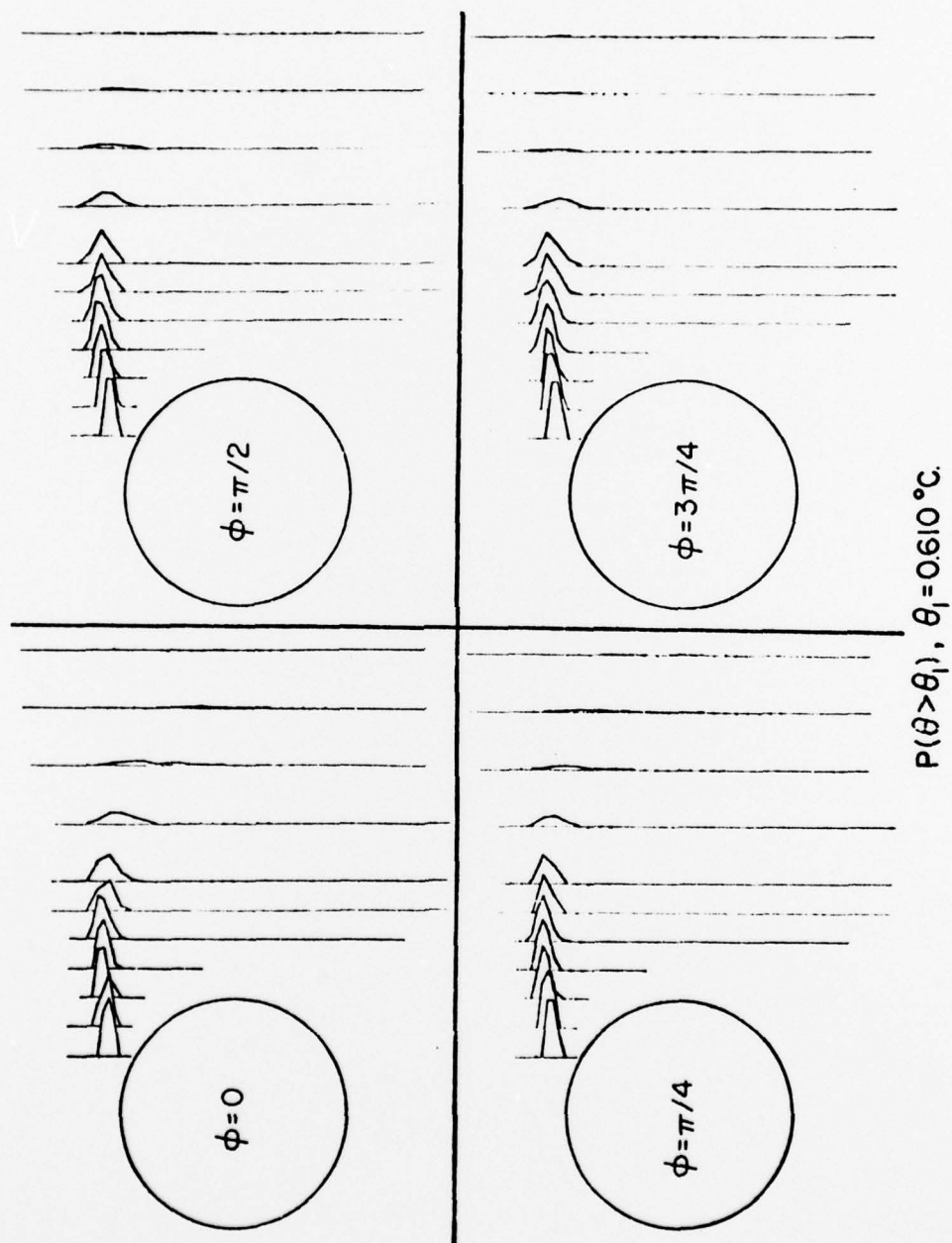
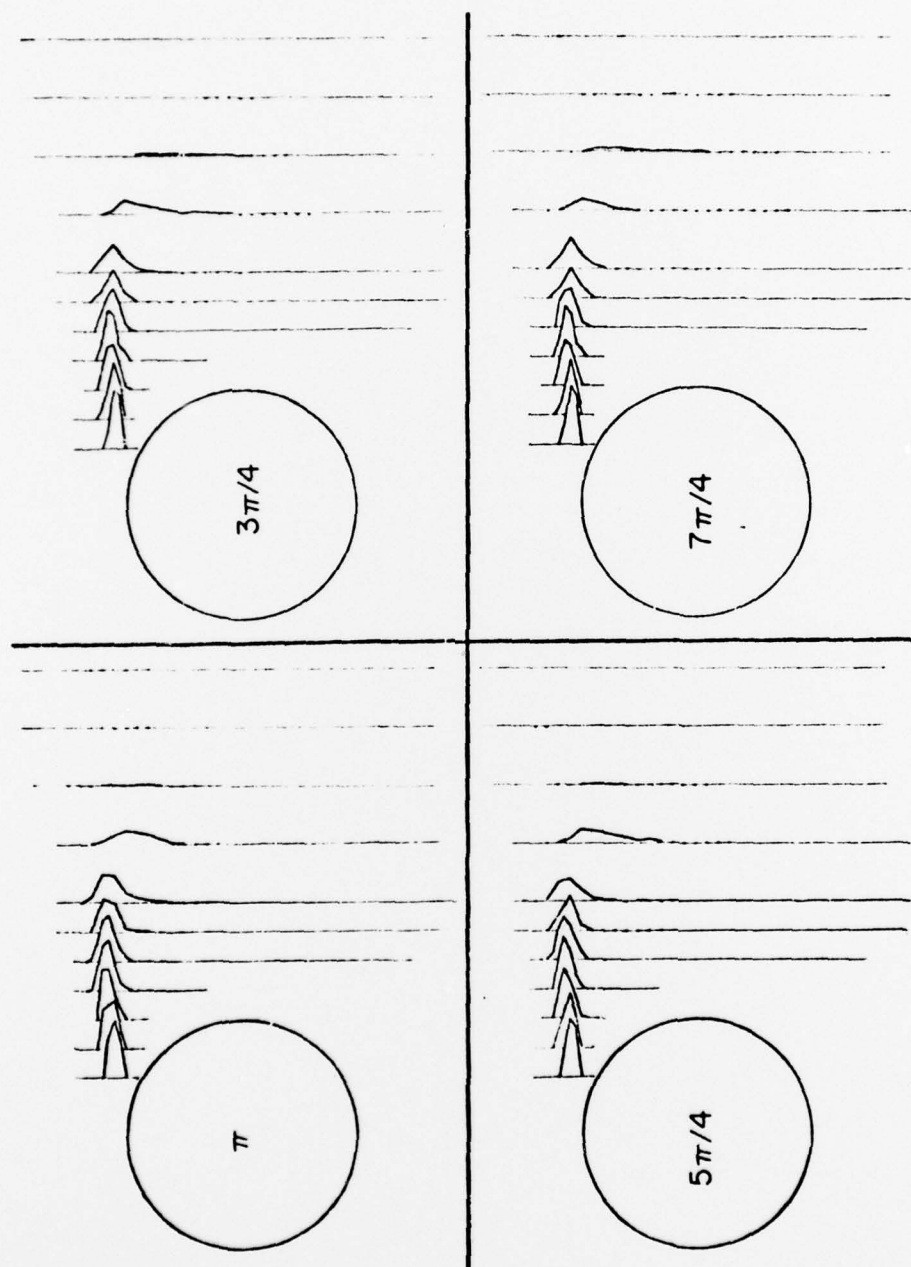
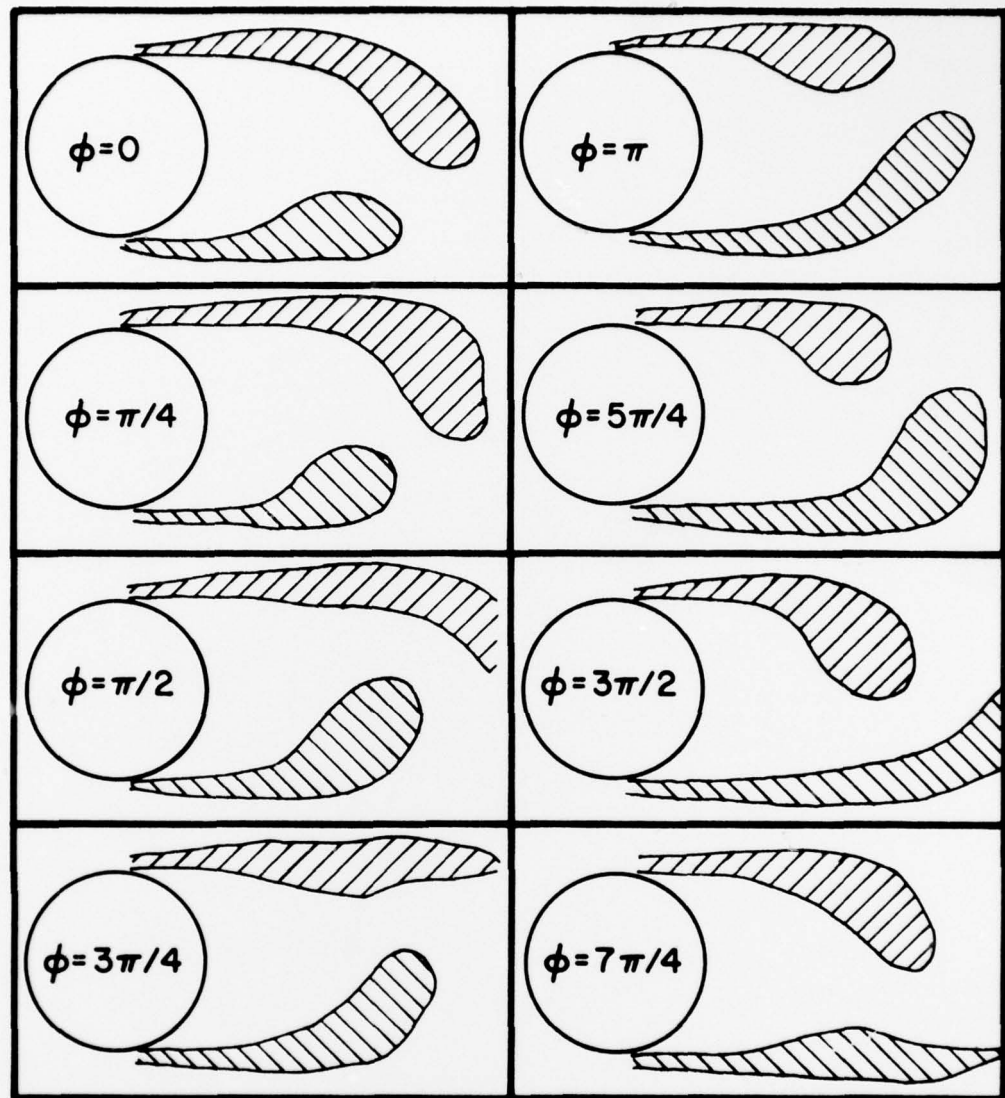


Figure 41. Probability Distributions through First Half of Shedding Cycle for High Temperature Threshold



$$P(\theta > \theta_1), \theta_1 = 0.610^\circ \text{C.}$$

Figure 42. Probability Distributions through Second Half of Shedding Cycle for High Temperature Threshold





 REGIONS WHERE $P(\theta > 0.61^\circ\text{C}) > 0$
 EXPECTED RESULTS FROM $\phi + \pi$
 AND SYMMETRY

Figure 43. Regions of Nonzero Probability through Shedding Cycle for High Temperature Threshold

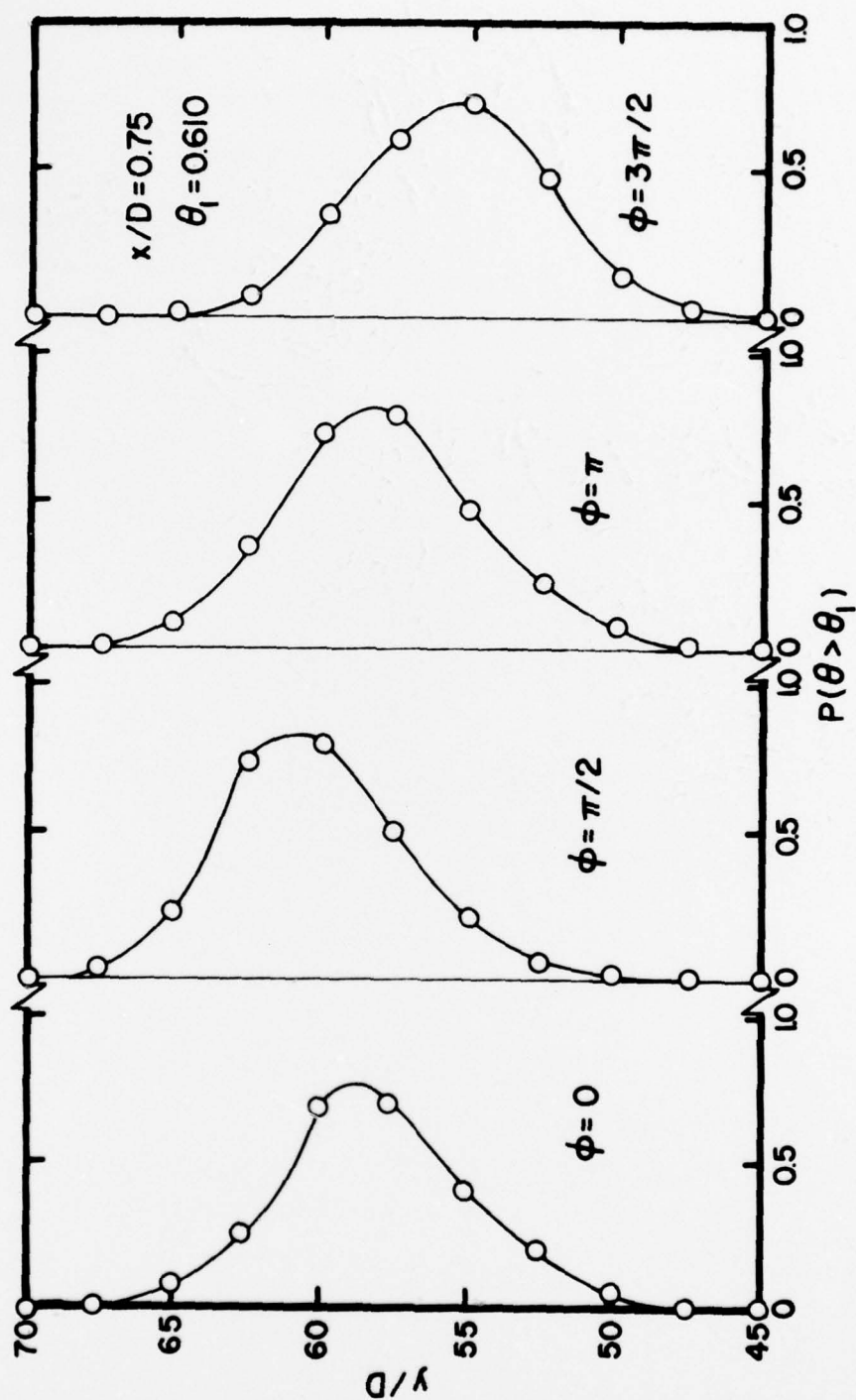


Figure 44. Phase Dependence of Probability Distributions at $x/D = 0.75$ for High Temperature Threshold

BIBLIOGRAPHY

- [1] Bearman, P. W. 1965. Investigation of the Flow Behind a Two-Dimensional Model with a Blunt Trailing Edge and Fitted with Splitter Plates. J. of Fluid Mech. 21,241.
- [2] Bendat, J. S. and Piersol, A. G. 1971. Random Data: Analysis and Measurement Procedures. Wiley-Interscience, New York.
- [3] Bloor, M. S. 1964. The Transition to Turbulence in the Wake of a Circular Cylinder. J. of Fluid Mech. 19,2,290.
- [4] Bloor, M. S. and Gerrard, J. H. 1966. Measurements on Turbulent Vortices in a Cylinder Wake. Proc. of the Royal Soc. A, Vol 294,319.
- [5] Born, M. and Wolf, E. 1965. Principles of Optics. Pergamon Press, Oxford.
- [6] Bracewell, R. 1965. The Fourier Transform and its Applications. McGraw - Hill, Inc., New York.
- [7] Cantwell, B. J. 1976. A Flying Hot Wire Study of the Turbulent Near Wake of a Circular Cylinder at a Reynolds Number of 140,000. Ph.D. Thesis California Institute of Technology.
- [8] Clements, R. R. 1973. An Inviscid Model of Two-Dimensional Vortex Shedding. J. of Fluid Mech. 57, 2, 321.
- [9] DeCoster, M. A. and Kibens, V. 1974. Periodic Vortex Shedding in the Wake of a Disk. Technical Report, University of Michigan.
- [10] Fabris, G. 1974. Conditionally Sampled Turbulent Thermal Velocity Fields in the Wake of a Warm Cylinder and its Interaction with an Equal Wake. Ph.D. Thesis, Illinois Institute of Technology.
- [11] Gabor, D. 1946. Theory of Communication. J. IEE Pt. III,93,429.
- [12] Gerrard, J. H. 1966. The Three-Dimensional Structure of the Wake of a Circular Cylinder. J. of Fluid Mech. 25,1,143.
- [13] Gerrard, J. H. 1966. The Mechanics of the Formation Region of Vortices Behind Bluff Bodies. J. of

Fluid Mech. 25,2,401.

- [14] Gerrard, J. H. 1967. Experimental Investigation of Separated Boundary Layer Undergoing Transition to Turbulence. The Phys. of Fluids Supplement. 598.
- [15] Hanson, F. B. and Richardson, P. D. 1968. The Near-Wake of a Circular Cylinder in Crossflow. Trans. of the ASME, Journal of Basic Engineering. Dec., 1968, 476.
- [16] Keefe, R. T. 1961. An Investigation of the Fluctuating Forces Acting on a Stationary Circular Cylinder in a Subsonic Stream and of the Associated Sound Field. University of Toronto, Rept. UTIA No. 76.
- [17] LaRue, J. C. and Libby, P. A. 1974. Temperature and Intermittency in the Turbulent Wake of a Heated Cylinder. The Phys. of Fluids. Vol. 17,5,873.
- [18] Maekawa, T. and Mizuno, S. 1967. Flow Around the Separation Point and in the Near-Wake of a Circular Cylinder. The Phys. of Fluids Supplement. 5184.
- [19] Mattingly, G. 1962. An Experimental Study of the Three Dimensionality of the Flow Around a Circular Cylinder. Tech. Note BN-295, University of Maryland.
- [20] Morkovin, M. V. 1964. Flow Around a Circular Cylinder-A Kaleidoscope of Challenging Fluid Phenomena. Symposium on Fully Separated Flows, ASME, New York.
- [21] Morrison, R. 1967. Grounding and Shielding Techniques in Instrumentation. John Wiley and Sons, Inc. New York.
- [22] Rabiner, L. and Gold, B. 1975. Theory and Application of Digital Signal Processing. Prentice Hall, Inc., Englewood Cliffs, New Jersey.
- [23] Roshko, A. 1958. On the Development of Turbulent Wakes from Vortex Streets. National Advisory Committee for Aeronautics, TR 1191.
- [24] Schaefer, J. W. and Eskinazi, S. 1959. An Analysis of the Vortex Street Generated in a Viscous Fluid. J. of Fluid Mech. 6,241.

- [25] Schiller, L. and Linke, W. 1933. Pressure and Frictional Resistance of a Cylinder at Reynolds Numbers 5,000 to 40,000. National Advisory Committee for Aeronautics. TM 715.
- [26] Shimizu, K. 1973. Spanwise Correlation in the Wake of a Circular Cylinder. Journal of Science of the Hiroshima University. Series a, Vol.37, No. 1.
- [27] Titchmarsh, E. C. 1959. Introduction to the Theory of Fourier Integrals. University Press, Oxford.
- [28] Toebe 1968. The Unsteady Flow and Wake Near an Oscillating Cylinder. J. of Basic Eng. 68-WA/FE-23.
- [29] Von Kármán, T. and Rubach, H. 1912. Über den Mechanismus des Flüssigkeits und Luftwiderstandes. Phys. Zs., Bd. 13, Heft 2.
- [30] Wille, R. 1972. Generation of Oscillatory Flows. Symposium on Flow-Induced Structural Vibrations. Karlsruhe, Germany.
- [31] Wlezien, R. W. and Way, J. L. 1976. Bridge Circuits for Differential Resistance Measurement and their Application to Resistance Thermometry. IEEE Transactions, to be published.